Thermodynamic stability of the novel tricontinuous $3ths(5)$ structure in self-assembled melts of triblock star-copolymers

Masterarbeit aus der Physik

Vorgelegt von

Michael Fischer

27. Februar 2014

Lehrstuhl für Theoretische Physik I
Friedrich-Alexander-Universität Erlangen-Nürnberg

Betreuer: PD Dr. Gerd Schröder-Turk

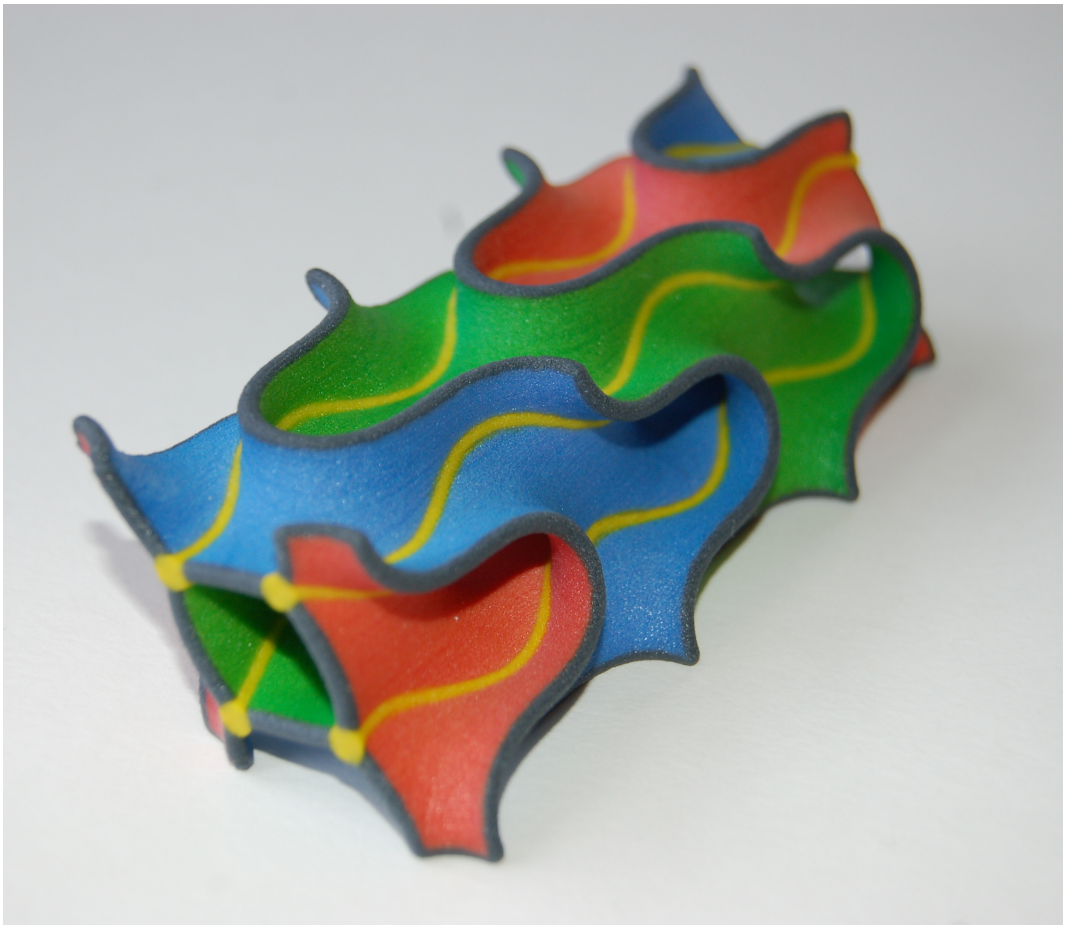

Photo of a 3D printed model of a tricontinuous structure. This thesis presents the thermodynamic stability of the pictured morphology in certain self-assembled copolymer melts.

Abstract

Copolymeric self-assembly provides an efficient route to the formation of ordered three-dimensional nanostructures. A well known example are diblock copolymers which are macromolecules that consist of two chemically different but covalently linked polymer chains. Due to the immiscibility of chemically distinct polymer species one observes a variety of morphologies that self-assembly in melts of these molecules. The most complex equilibrium mesophase being observed in diblock copolymer melts is the core-shell Gyroid, based on the bicontinuous intergrowth of two continuous network domains. Adaption of the molecular architecture, such as the introduction of a third chemically distinct species, is a proven strategy to achieve different phases, stabilising e.g. the alternating Gyroid and the Fddd network phase in linear triblock copolymers, or kaleidoscopic columnar phases in star-shaped triblock terpolymers.

However, the formation of phases based on the intergrowth of more than two network domains has not yet been reported in copolymer melts. In this thesis we show that a triply-periodic tricontinuous structure based on the intergrowth of three distorted chemically distinct *ths* nets, thus denoted $3ths(5)$, is a thermodynamically stable equilibrium phase of star-shaped triblock copolymers when a fourth phase, an extended molecular core, is introduced into the molecular architecture. This tricontinuous morphology has long-range crystalline order but low symmetry, in contrast to most other self-assembled mesophases.

We use the spectral method of the self-consistent field theory for polymers to confirm the geometric intuitions, gained from analytical expressions in the strong segregation limit, why the introduction of an extended core leads to the formation of this new phase. Its effect is a change in the relative importance of interface tension between the three initial polymeric species and entropic chain stretching contributions to the free energy. As a consequence, the arrangement of the molecular cores on a close-packed lattice of lines is favored.

Beyond the prediction of the first tricontinuous network phase in copolymer melts, this study discusses the existence of two new columnar phases and suggests the utilization of molecular cores as a new general concept for extending the range of self-assembled soft matter morphologies.

Contents

Chapter 1

Introduction

One of the most fascinating aspects of nature is its ability to form shapes and structures. In many of these phenomena molecules or small constituents, governed by very basic laws of physics, will self-assemble into structures with astonishing complexity and functionality. This observation motivates both fundamental and applied research. The idea that increasing complexity can emerge from simpler components continues to pose new questions for science up to the understanding of the development of life itself. In terms of applications and fabrication it is remarkable that a complex structure with specific functionality can be achieved and tuned by simply mixing a number of similar components which will then readily form the desired product.

Soft matter self-assembly therefore continues to attract much attention due to its ability to form complex and fascinating structures emerging from rather simple underlying molecular designs. An example are block copolymers and related molecules. These are known for the variety of structure they form as well as their technological importance [4]. Each copolymer consists of two or more chemically different polymer chains which are covalently linked together in order to form these macromolecules. Figure 1.1 shows a schematic of some copolymer architectures.

The simplest systems are melts of diblock copolymers, shown in figure 1.1(a). The chemically different polymer chains (shown in different colors in the pictures) tend to spatially segregate but are inhibited from separating on a macroscopic length scale because they are covalently linked to each other (shown by a yellow dot in the pictures). Therefore, these systems will microphase separate with each species occupying different domains thereby self-assembling into various micro- and nano-structures. One of the most interesting mesophases observed in diblock copolymer melts is the cubic core-shell Gyorid (or double-Gyroid) structure [70] of symmetry $Ia\bar{3}d$, that consists of two intergrown periodic and highly symmetric network domains, each of which is occupied by the polymeric minority species. These labyrinthine domains are separated by a sponge-like matrix of the majority species, as illustrated in figure 1.2.

This fascinating self-assembled morphology has become the epitome of a complex soft matter network phase with a plethora of applications as a functional nano-material [6]. Its spontaneous formation in various biological and synthetic systems [35], including block-copolymers [24, 57], and the demonstration that it can be used as a template for metallic and inorganic replicas [84] increase its value as a real-world material. The double-Gyroid, or its

chiral single-network counterpart have demonstrated photonic [45, 67], plasmonic [62, 68], mechanical and transport [80], electrochromic [69] or photovoltaic [8] functions, all of which are essentially determined by the network-like percolating nature of its geometry. Figure 1.3 shows a SEM image of a calcite single crystal that has been replicated using a Gyroid-forming block copolymer template [17].

The existence of single-network structures and double-network structures points immediately to the question, if nanostructures composed of three or more network domains can be devised and suitable self-assembly processes found [2]. This thesis considers balanced tricontinuous structures, which result from the intergrowth of three identical periodic networks. The networks naturally divide space into exactly three regions, the backbone of each being one of the periodic nets. By pure geometric consideration, the dividing surface between three intergrown networks (considered identical for the sake of simplicity) necessarily contains curves, here called *triple lines*, along which all three network domains meet. The interface between two of the three graphs is otherwise composed of curved surface patches (that may be modelled as minimal surfaces). An illustration of such an intricate tricontinuous structure is given by the photo at the beginning of this thesis.
While no complete systematic taxonomy of such tricontinuous structures can be offered yet, numerous structures have been devised [14, 32, 33, 34], partially by hyperbolic geometry [32, 33, 34, 36, 37].

The three-way partition of space into a triplet of locally adjacent networklike domains suggests the possible self-assembly of these structures by star-shaped molecules with three immiscible components, such that the molecular centers decorate some (or all) of the triple lines. To be precise, we will refer to triple lines that are decorated by molecular cores as *branch lines*. The subdivision of space into the three network domains is then the result of the immiscibility of the three components. The template for these sort of molecules is the triblock star-copolymer architecture, sometimes referred to as ABC star-shaped terpolymers, shown in figure 1.1(c). This architecture is characterized by covalently linking three

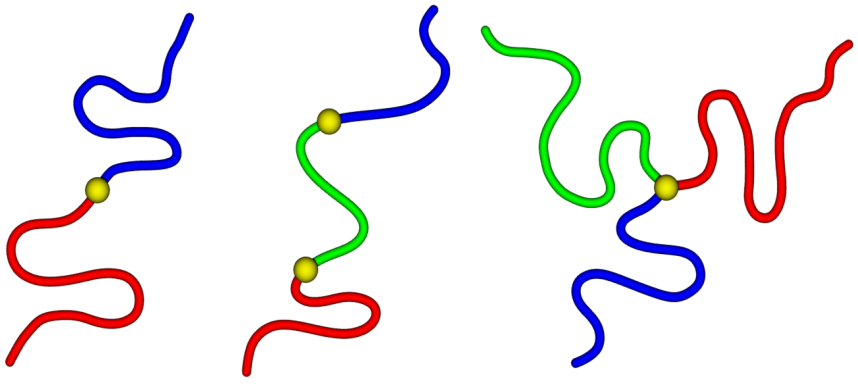

(a) (b) (c)

Figure 1.1: Overview of possible copolymer architectures. Different colors represent chemically different polymer species. Each species forms polymer chains which can be linked together, depicted by yellow dots, to form the respective copolymer molecules. (a) Diblock copolymer. (b) Linear triblock copolymer. (c) Triblock star-copolymer, the template for the molecules examined in this thesis.

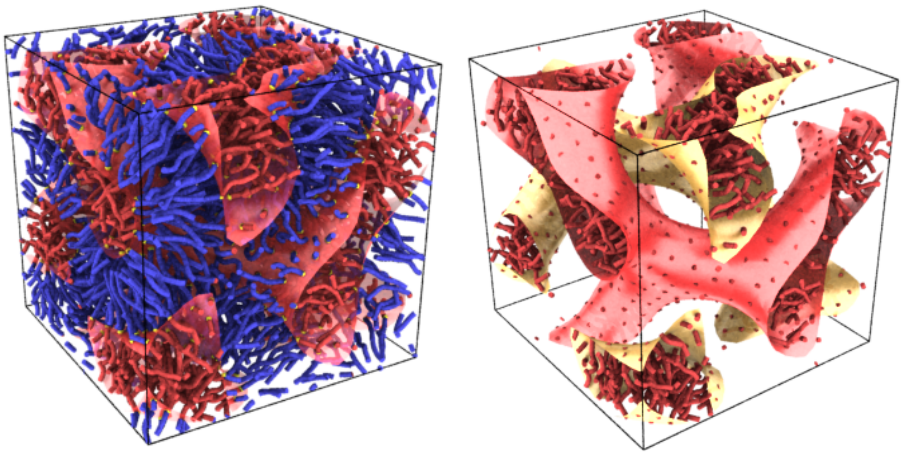

(a) (b)

Figure 1.2: Artistic representation of diblock copolymers self-assembling into the double-Gyroid phase. This morphology consists of two interwoven network-like domains occupied by the minority species, shown in red, that are separated by a sponge-like dividing region formed by the majority species, shown in blue. (a) Depiction of the overall structure formed by self-assembled diblock copolymers. The interfaces between the chemically different species are shown by red surfaces. (b) Only the minority species is shown. The two network-like domains that are occupied by this species are shown in different colors for clarification.

chemically different chains in the molecular center.
In general, simple triblock star-copolymers usually form a variety of tiling patterns in dependence of the volume fractions of their polymer species and the interaction parameters between them, as shown in figure 1.4. This is the result of existing theoretical investigations [78, 41, 39], and is confirmed by experiments [55]. Figure 1.5 shows the experimentally observed mesophases which correspond to the simulation results shown in figure 1.4. In this thesis, we focus on balanced structures with equal volume fractions for all species and equal interaction parameters between all of them. For this case one observes the 6.6.6 tiling pattern reminiscent of a three-colored honeycomb structure. We present that clever adaptations of the molecular design of triblock star-copolymers, based on the introduction of an extended molecular core, destabilize the formation of the 6.6.6 tiling and thereby lead to novel tricontinuous structures. This search for tricontinuous morphologies in triblock star-copolymer melts is further motivated by an experimental study which suggested the formation of complex mesophases in these systems [63].
Realisations of tricontinuous geometries are also conceivable in amphiphilic lipid or surfactant systems [72], which represent the likely precursor phase to the (to date) sole experimental realization of a tricontinuous structure in the solid IBAN-9 mesoporous silicate phase based on the $3etc(187)$ structure [25].

The theoretical understanding of self-assembly in these polymeric systems is feasible by means of a self-consistent field theory which treats the polymers as flexible chains. In the limit of strong segregations between chemically different moieties these chains are highly stretched outwards from their common covalent bond in the molecular center. Semenov derived an analytical approximation for this limit, which allows to relate the geometry of a

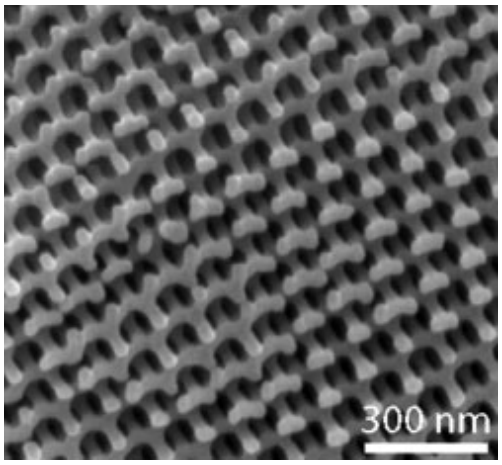

Figure 1.3: Scanning electron microscopy (SEM) image of a nanostructured calcite single crystal that follows a Gyroid network. This crystallization process is based on a block copolymer that self-assembles into a Gyroid morphology such that the minority species occupies the two network-like domains. After removing the minority species the calcite can be grown into the resulting porous channels. In the image, only one of the two networks has been replicated by calcite which becomes visible after removing the remaining majority polymer species. The picture has been taken from [17].

structure to its free energy [74]. The two emerging contributions to this free energy are an interfacial term due to unfavorable contacts between distinct species on the one hand, and a term quantifying the entropic penalty of stretching polymer chains within the individual domains on the other. The incompressible melt state enforces the latter contribution since the polymer chains have to fill space uniformly in these systems. This allows us to evaluate candidate structures with respect to certain geometric attributes and gives invaluable insight into the driving forces of block copoylmer self-assembly. Furthermore, we apply a numerical approach developed by Matsen and Schick [53] to solve the full self-consistent field theory. This enables us to verify the developed concepts and to determine accurate values for the free energies of various structures for different system parameters. These methods are presented in detail in chapter 2.

One of the standard examples, for which this theory has been developed, and where it has been successfully applied, are melts of diblock copolymers. Chapter 3 therefore reviews the mesophases found in these systems and shows the agreement of the theoretical and experimental studies devoted to this subject. We show how the analytical expressions of the strong segregation limit emphasize the role of curvature and packing frustration for these self-assemblies. One of the observed mesophases - the bicontinuous Gyroid - exhibits a rather complex geometry and allows for curvatures between those of the flat lamellar and the cylindrical phase. This structure is characterized by two interpenetrating network domains and hence one of the main motivations to look for tricontinuous structures, i.e. structures made of three interwoven networks, in soft matter systems in the next step. We discuss the relevance of tricontinuous structures for diblock copolymers and related soft matter systems with special emphasis on the $3etc(193)$ structure, which has been observed in experiments [25].

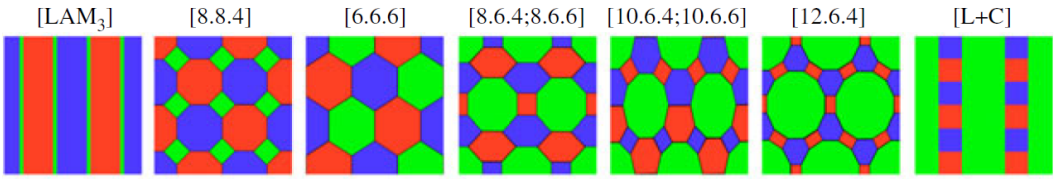

Figure 1.4: Tiling patterns usually formed by triblock star-copolymers. The chemically different moieties are shown in different colors. The 6.6.6 tiling (third from the left), reminiscent of a three-colored honeycomb structure, is formed in systems of *balanced* copolymers with equal volume fractions for each species and uniform interactions between them. The presented sequence was obtained by dissipative particle dynamics simulations and the picture has been taken from [39].

In order to stabilize balanced structures other than the honeycomb pattern, which clearly provides the best shape to minimize interfacial area, we have to further pronounce the chain stretching term to the free energy. We discuss a number of ways to increase this contribution to the self-assembly process, based on the introduction of an extended or functionalized core to the molecular centers of triblock (three-arm) star-copolymers, which essentially leads to an increased emphasis on packing frustration within the morphologies. The detailed realization of the molecular cores and its influence can be treated in different ways, each corresponding to different experimental situations. We examine some of the more relevant constructions and show their influence on the geometrical understanding of the self-assembly process. Specifically, we focus on the realization of the core by a fourth polymeric species. This species forms the center of the molecule and has the other arms attached to it. In this way, we are able to examine these concepts with the usual methods placed at our disposal by the self-consistent field theory. However, different types of realizations, for example rigid cores, should result in qualitatively comparable results. Chapter 4 examines the analytical

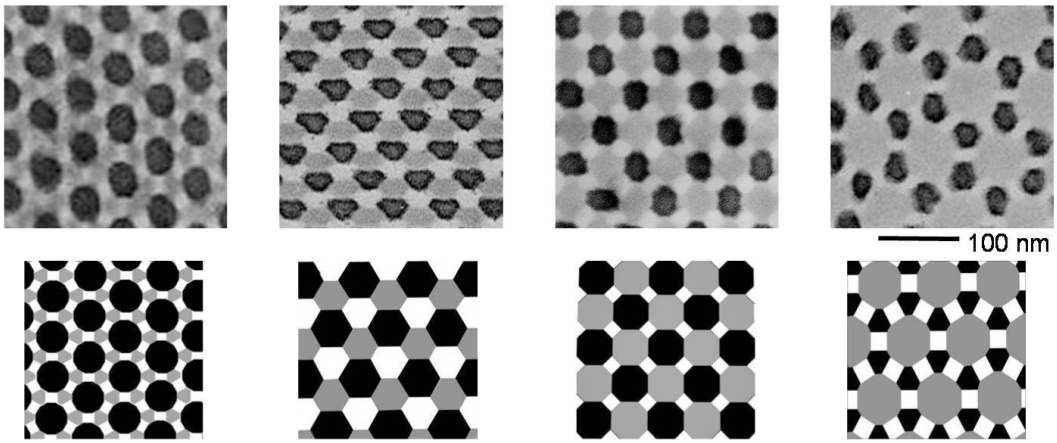

Figure 1.5: Experimentally identified mesophases in triblock star-copolymer melts, observed via transmission electron microscopy (TEM). The top row shows the TEM images while the bottom row shows a schematic of the respective structure. These mesophases correspond well to those found in simulations, cf. figure 1.4. The picture has been taken from [55].

results which link the geometry of our candidate structures to their free energies, when seen as mesophases of star-copolymer melts. Therefore, this chapter is of particular importance as it presents new ideas to achieve novel complex structures in soft matter systems.

We present a selection of columnar and tricontinuous morphologies that provide suitable candidates for self-assembled mesophases in triblock star-copolymer melts in chapter 5. Special attention is devoted to the branch lines within the structures because these are the regions that are decorated by the molecular cores. Therefore, their arrangement is directly linked to the degree of packing frustration. We apply geometric measures developed in chapter 4 to assess the structures with respect to their packing frustration and their interface configuration thereby elucidating their role for star-copolymer self-assembly.

In chapter 6 we finally employ the numerical method to solve the self-consistent field theory for star-shaped copolymers with an extended core. By accurately calculating the free energies of different candidate structures, we are able to test the validity of the geometric considerations that have been developed in chapter 4 and applied in chapter 5. We construct phase diagrams for melts of star-copolymers with an extended polymeric core that has two arms of each other species attached to it, which further emphasizes the importance of suitable branch line arrangements. The parameters of these diagrams are the volume fraction of the core and its relative segregation strength, compared to the strength of segregation between the attached polymer species among each other. These phase diagram present profound evidence for the thermodynamic stability of the novel tricontinous $3ths(5)$ phase for molecules with large enough and well segregated cores.

Chapter 7 summarizes our results and discusses possible extensions of the theoretical investigation. More importantly, however, we discuss possibilities how the predicted tricontinuous structure could be realized experimentally. This thesis therefore aims to lead the way for further theoretical and experimental studies which investigate novel intriguing mesophases.

Chapter 2

Self-consistent field theory for block copolymers

The theoretical treatment of block copolymers is feasible by means of a self-consistent field theory (SCFT) approach which treats the individual blocks of the copolymer as flexible Gaussian chains [26]. The chains are attached to each other according to the copolymer architecture. Since the treatment uses the mean field approximation, each copolymer is treated as being subject to an external field describing the interactions with the other molecules instead of keeping track of the interactions between each copolymer and every other one. Upon assuming a particular morphology this allows us to calculate the free energy of the system. Section 2.1 shows the basic derivation of this theory.

For arbitrary interaction strengths, these calculations can only be done numerically. However, assuming strong segregation between chemically different polymer species, which in turn results in high stretching of the chains, one can utilize further approximations allowing for an analytical treatment. This has first been shown in 1985 by A. N. Semenov [74] and has been established as the strong segregation theory (SST). The resulting analytical expressions for the free energy of the system are invaluable for understanding the driving forces behind the self-assembly process since they link geometric features of a structure to its free energy. We apply exactly these formulas to elucidate the geometric understanding of the structures discussed in this thesis and show how the introduction of an extended core in the center of triblock star-copolymers can lead to new complex morphologies. Section 2.2 shows the general ideas leading to the SST limit. Although the SST is believed to be in agreement with the strong segregation limit of the SCFT, some corrections to this approach have been pointed out [43, 54].

Thus we relax the assumptions for this approximation and use numerical methods to solve the full SCFT for finite segregation strength in order to verify the ideas we developed and to determine the free energies of different morphologies more accurately. For this purpose we apply the spectral method first developed by Matsen and Schick [53] to numerically evaluate the self-consistent field equations. In order to solve the equations within this framework we use the Anderson mixing scheme as demonstrated in [49]. In the case of triblock star-copolymers the equations involved take a slightly different form compared to those presented in [53, 49]. A real-space SCFT approach examining the phases of triblock star-copolymers has been employed in [78, 41] focusing, however, not on the complex

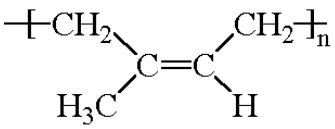

Figure 2.1: Chemicals structure of Polyisoprene, a common polymer. By linking together a number of alike chemical monomer units, as is depicted here, a polymer chain is formed. The graphic was taken from http://pslc.ws/macrog/isoprene.htm.

phases discussed here, but primarily on the simpler columnar tilings observed in a wide region of the phase space, see figure 1.4. In section 2.3 we demonstrate the equations involved in the spectral method when applied to the molecular architectures of interest for this thesis.

The derivation of the self-consistent field equations and of the strong segregation limit can be found in various literature sources. For this chapter we used review articles which summarize these concepts and provide a good introduction to the theory, e.g. [58, 47, 13, 22, 48].

2.1 Gaussian chain model in mean-field approximation

This section adopts ideas from all of the above mentioned literature, whereby the notation mainly follows [48]. The derivation is tailored to be applicable to (core-)star-copolymers discussed in this thesis. Polymer dynamics are known to be slow and it can take a lot of time for them to reach their equilibrium state, or they can be completely stuck in a metastable configuration. Since we are interested in the morphological properties of copolymer systems in equilibrium, we restrict ourselves to the melt state where the dynamics are faster compared to the solid state and the system can adopt its equilibrium behavior. This allows us to use statistical mechanics to examine these systems [48].
We start by looking at a single polymer chain. A typical example is Polyisoprene, whose chemical formula is given in figure 2.1. Polymers consist of a large number of identical chemical units called monomers. By linking these monomers together a polymer chain is formed.

In the limit of high molecular weights, i.e. large numbers of monomers per molecule, polymer configurations in the melt state can be described by non-avoiding random walks. Independent of the precise model for the probability distribution of the distance and orientation between adjacent monomer units we can introduce coarse-grained *segments* of the polymer chain, each consisting of multiple monomers. By virtue of the central limit theorem, the probability distribution for the difference vector between two neighboring segments, denoted $\vec{r}$, approaches a Gaussian,

$$p(\vec{r}) \to \left(\frac{3}{2\pi a^2}\right)^{\frac{3}{2}} \exp\left(-\frac{3r^2}{2a^2}\right), \tag{2.1}$$

upon increasing the number of monomer units per segment. Here, a denotes the *statistical segment length* of the polymer chain consisting of N segments. Let $\vec{R}$ be the difference vector between the two end points of the polymer chain. As a consequence of the chosen model,

the root-mean-square average, R_0, measuring the size of the polymer is given by

$$R_0 \equiv \sqrt{\left\langle \vec{R}^2 \right\rangle} = N^{\frac{1}{2}} a. \tag{2.2}$$

A more realistic model for isolated polymer chains are self-avoiding random walks. These do not obey (2.2) but yield $R_0 \propto N^\nu$ with $\nu \approx 0.6$ [10]. However, in a polymer melt the individual polymer chains have to avoid themselves as well as all the other chains. In this case the polymer reverts back to the random-walk statistics and expression (2.1) as well as expression (2.2) are in fact describing the polymers correctly, although the value for the statistical segment lengths has to be modified [85].
Hence we proceed by describing a polymer chain as N coarse-grained segments which can additionally be exposed to external fields. Each segment has volume ρ_0^{-1} and statistical segment length a. The segments are large enough so that they obey Gaussian statistics but also small enough such that possible external interactions acting on them can be assumed to be homogeneous on the scale of the segment length. With this so-called coarse-grained Gaussian model for high molecular weight polymers we can imagine these macromolecules as flexible chains, cf. figure 1.1.

In the next step, we go from simple polymer chains to block copolymers. These macromolecules are made of multiple polymer chains, referred to as blocks, which are covalently linked together. Each individual chain can be chemically different to the others. Figure 1.1 shows possible architectures of block copolymers. Throughout this thesis, different colored chains are indicating chemically different polymer species. The yellow nodes in figure 1.1 symbolize the covalent bonds between these chains.
Chemically different polymer species tend to segregate spatially. Let us first consider a mixture of two types of polymer chains which are not linked together. For high enough segregation strength, which is usually given for low enough temperatures or high molecular weights, these species can macrophase separate. The polymers of each species then tend to occupy different volumes, thereby decreasing the interfacial area, or equivalently the overlap, between unlike species which lowers the energy of the system. This is the same phenomenon as can be observed in mixtures of oil and water. However, by linking polymer chains of different species together, these molecules can not macrophase separate anymore. Rather, we observe microphase separation, which means that the species still separate spatially from one another, but on a much smaller length scale. To achieve this spatial segregation the molecules will form structures on a mesoscopic scale, which allows them to minimize the free energy of the system. This observation and its analysis form the main focus of this thesis.

In the following, we consider a melt of n identical copolymer molecules with fixed volume,

$$V = n\frac{N}{\rho_0}. \tag{2.3}$$

We label each copolymer by an index α and allow for multiple and possibly chemically different polymer chains linked together according to the architecture of the macromolecule. Each polymer chain is divided into segments such that the volume per segment, ρ_0^{-1}, is independent of the monomer species contained in it. This leads to the possibility of different statistical segment lengths a_I for chemically different polymer chains, where $I \in \mathbb{I} \equiv \{A, B, C, ...\}$ labels the monomer species. From here on N denotes the total number of segments contained in each copolymer and hence the sum of the segments of all polymer chains making up the molecule. The coarse-grained trajectory of each copolymer can be described by a set

of connected curves in space. Each curve corresponds to a polymer chain. Due to covalent bonds in the copolymer these curves have to be connected. The curve belonging to the ith chain of species I in the αth copolymer is given by a function $\vec{r}_{\alpha,I,\iota}(s)$, where $0 \leq s \leq f_{I,\iota}$. Equal intervals of s have the same molecular weight. We note that in this instance we use a different notation compared to the literature. This is due to the fact that we intend to describe comparatively complex molecular architectures and hence need an efficient way of parameterizing them. $f_{I,\iota}$ denotes the relative length of the respective polymer chain and indicates that the chain comprises monomers of species $I \in \mathbb{I}$. The second index, ι, enumerates the individual chains of species I in the copolymer. Therefore, $1 \leq \iota \leq I^{max}$, where I^{max} is the number of chains of species I in each copolymer. Typically, the parametrization is chosen such that by summing up the intervals of all chains we end up with one, $\sum_{I\in\mathbb{I}} \sum_{\iota=1}^{I^{max}} f_{I,\iota} = 1$. With this we can introduce (dimensionless) segment concentrations. The concentration of segments of species I stemming from a single copolymer with index α is given by

$$\hat{\phi}_{\alpha,\iota}(\vec{r}) = \frac{N}{\rho_0} \sum_{i=\iota}^{I^{max}} \int_0^{f_{I,\iota}} ds\ \delta\left(\vec{r} - \vec{r}_{\alpha,I,\iota}(s)\right). \tag{2.4}$$

The I-segment concentration for the whole melt is then simply

$$\hat{\phi}_I = \sum_{\alpha=1}^{n} \hat{\phi}_{\alpha,\iota}. \tag{2.5}$$

Using this definitions we can treat the segregation between unlike monomers based on the concept of simple contact energies. Let us consider the interactions between segments of species A and B. Assuming the number of contacts between those species in a small volume d^3r at position $\vec{r}$ is proportional to $\hat{\phi}_A(\vec{r})\hat{\phi}_B(\vec{r})d^3r$ allows us to express the total internal energy of the melt, U, as

$$\frac{U\left[\hat{\phi}_A(\vec{r}), \hat{\phi}_B(\vec{r})\right]}{k_B T} = \chi\rho_0 \int d^3r\ \hat{\phi}_A(\vec{r})\hat{\phi}_B(\vec{r}), \tag{2.6}$$

where χ is a dimensionless parameter measuring the interaction strength [18]. Note that due to the incompressibility of the system the interactions between alike monomers can be incorporated into this derivation, essentially leaving us with expressions of the form (2.6) [10, 48]. χ is usually temperature dependent and a common empirical expression describing this dependency is given by

$$\chi\rho_0 = \frac{\alpha}{T} + \beta, \tag{2.7}$$

where α and β are constants that depend on the chosen (co)polymers [56]. The extension of this concept to systems containing more than two chemically different monomer species is straightforward. One simply accounts for all possible interactions between pairs of unlike species. To do this we introduce parameters χ_{JK} measuring the segregation strengths between species J and species K and end up with

$$\frac{U\left[\{\hat{\phi}_I\}_{I\in\mathbb{I}}\right]}{k_B T} = \frac{1}{2} \sum_{J\neq K\in\mathbb{I}} \chi_{JK}\rho_0 \int d^3r\ \hat{\phi}_J(\vec{r})\hat{\phi}_K(\vec{r}), \tag{2.8}$$

whereby $\chi_{JK} = \chi_{KJ}$ and the factor $\frac{1}{2}$ accounts for the fact that interactions between species J and K have been counted twice in the summation.

Having listed all the ingredients for our model, we start by formulating the partition function of the system,

$$Z \propto \frac{1}{n!} \int \prod_{\alpha=1}^{n} \tilde{D}\vec{r}_\alpha \exp\left(-\frac{U\left[\{\hat{\phi}_I\}_{I\in\mathbb{I}}\right]}{k_B T}\right) \delta\left(1 - \sum_{I\in\mathbb{I}} \hat{\phi}_I\right). \tag{2.9}$$

The delta function ensures the incompressibility of our system and the prefactor $\frac{1}{n!}$ accounts for the indistinguishability of the molecules. The Boltzmann factor incorporates the internal energy of the system and is of the form (2.8).
Note that the functional integration is performed over all possible coarse-grained configurations $\{\vec{r}_\alpha\}_{\alpha=1,\dots,N}$ of the copolymers which summarizes the trajectories of all connected curves of each molecule. It is already weighted accounting for the statistical probability of the respective configuration of a copolymer molecule, $\tilde{D}\vec{r}_\alpha = D\vec{r}_\alpha P[\vec{r}_\alpha]$. Due to the internal (stretching-)entropy of each coarse-grained segment this probability is given by

$$P[\vec{r}_\alpha] = \exp\left(-\sum_{I\in\mathbb{I}} \sum_{\iota=1}^{I^{max}} \frac{3}{2a_I^2 N} \int_0^{f_{I,\iota}} ds \left|\frac{d}{ds}\vec{r}_{\alpha,I,\iota}(s)\right|^2\right). \tag{2.10}$$

This expression is chosen to reproduce the Gaussian probability distribution for the difference vectors between adjacent segments, shown in (2.1).
It has to be noted that the kinetic energy should also contribute to the Boltzmann factor in (2.10) and the integrations should also be performed over the momenta of all monomers. However, due to the form of the kinetic energy the momentum coordinates can be integrated out and included in the proportionality factor in (2.9) [30]. Since we do not need the precise form of this factor we can stick with expression (2.9) and (2.10).

To proceed, we insert functional integrals over expressions of the form $\delta\left[\Phi_I - \hat{\phi}_I\right]$ into (2.9). This is similar to (A.4) shown in the appendix and allows us to identify the operators $\hat{\phi}_I(\vec{r})$ with the ordinary functions $\Phi_I(\vec{r})$,

$$Z \propto \frac{1}{n!} \int \prod_{I\in\mathbb{I}} D\Phi_I \int \prod_{\alpha=1}^{n} \tilde{D}\vec{r}_\alpha \exp\left(-\frac{U\left[\{\Phi_I\}_{I\in\mathbb{I}}\right]}{k_B T}\right) \delta\left[\Phi_I - \hat{\phi}_I\right] \delta\left[1 - \sum_{I\in\mathbb{I}} \Phi_I\right]. \tag{2.11}$$

As is shown in (A.7) we can replace the delta functionals with integral representations leading to

$$\begin{aligned} Z \propto \frac{1}{n!} \int \prod_{I\in\mathbb{I}} \Phi_I \int \prod_{I\in\mathbb{I}} DW_I \int D\kappa \int \prod_{\alpha=1}^{n} \tilde{D}\vec{r}_\alpha \ \exp\left(-\frac{U\left[\{\Phi_I\}_{I\in\mathbb{I}}\right]}{k_B T}\right) \\ \times \exp\left(\frac{\rho_0}{N} \int d^3r \ \sum_{I\in\mathbb{I}} W_I(\vec{r}) \left[\Phi_I(\vec{r}) - \hat{\phi}_I(\vec{r})\right] + \kappa(\vec{r}) \left[1 - \sum_{I\in\mathbb{I}} \Phi_I(\vec{r})\right]\right). \end{aligned} \tag{2.12}$$

By inserting (2.4) into (2.12) we get

$$\begin{aligned} Z \propto \frac{1}{n!} \int \prod_{I\in\mathbb{I}} \Phi_I \int \prod_{I\in\mathbb{I}} DW_I \int D\kappa \ \exp\left(-\frac{U\left[\{\Phi_I\}_{I\in\mathbb{I}}\right]}{k_B T}\right) \\ \times \exp\left(\frac{\rho_0}{N} \int d^3r \ \sum_{I\in\mathbb{I}} W_I(\vec{r})\Phi_I(\vec{r}) + \kappa(\vec{r}) \left[1 - \sum_{I\in\mathbb{I}} \Phi_I\right]\right) \\ \times \int \prod_{\alpha=1}^{n} \tilde{D}\vec{r}_\alpha \exp\left(-\sum_{\alpha=1}^{n} \sum_{I\in\mathbb{I}} \sum_{\iota=1}^{I^{max}} \int_0^{f_{I,\iota}} ds \ W_I\left(\vec{r}_{\alpha,I,\iota}(s)\right)\right). \end{aligned} \tag{2.13}$$

We identify

$$\begin{aligned} Q\left[\{W_I\}_{I\in\mathbb{I}}\right] &\propto \int \tilde{D}\vec{r}_\alpha \exp\left(-\sum_{I\in\mathbb{I}}\sum_{\iota=1}^{I^{max}}\int_0^{f_{I,\iota}} ds\; W_I\left(\vec{r}_{\alpha,I,\iota}(s)\right)\right) \\ &= \int \tilde{D}\vec{r}_\alpha \exp\left(-\frac{\rho_0}{N}\sum_{I\in\mathbb{I}}\sum_{i=\iota}^{I^{max}}\int d^3r\; W_I\left(\vec{r}\right)\hat{\phi}_{\alpha,\iota}(\vec{r})\right). \end{aligned} \tag{2.14}$$

as the partition function for a *single* copolymer whose chains of species I are subject to the corresponding fields W_I. The equality between both lines in this expression can immediately be seen by inserting $\hat{\phi}_{\alpha,\iota}$ from (2.4). κ can be interpreted as the Lagrange multiplier enforcing the incompressibility constraint. Substituting Q for the corresponding integrals in (2.13) and inserting (2.8) for the internal energy yields

$$\begin{aligned} Z \propto \frac{1}{n!}\int\prod_{I\in\mathbb{I}}\Phi_I\int\prod_{I\in\mathbb{I}}DW_I\int D\kappa\;\left(\frac{\rho_0}{N}Q\right)^n\;\exp\Bigg(-\frac{\rho_0}{N}\int d^3r \\ \left\{\frac{1}{2}\sum_{J\neq K\in\mathbb{I}}\chi_{JK}N\;\hat{\phi}_J(\vec{r})\hat{\phi}_K(\vec{r})-\sum_{I\in\mathbb{I}}W_I(\vec{r})\Phi_I(\vec{r})-\kappa(\vec{r})\left[1-\sum_{I\in\mathbb{I}}\Phi_I\right]\right\}\Bigg). \end{aligned} \tag{2.15}$$

Note that for the purpose of simplification a factor of $\left(\frac{\rho_0}{N}\right)^n$ has been extracted from the proportionality factor and moved to the single chain partition function.
Using the Stirling approximation $\ln(n!) = n\ln(n) - n$ and (2.3) we rewrite

$$\left(\frac{\rho_0}{N}Q\right)^n = \exp\left(n\ln\left(Q\frac{n}{V}\right)\right) = n!\exp\left(n\left[\ln\left(\frac{Q}{V}\right)+1\right]\right). \tag{2.16}$$

It can then be seen that (2.15) is of the form

$$Z \propto \int\prod_{I\in\mathbb{I}}\Phi_I\int\prod_{I\in\mathbb{I}}DW_I\int D\kappa\;\exp\left(-\frac{F\left[\{\Phi_I\}_{I\in\mathbb{I}},\{W_I\}_{I\in\mathbb{I}},\kappa\right]}{k_BT}\right). \tag{2.17}$$

In our case

$$\begin{aligned} \frac{F\left[\{\Phi_I\}_{I\in\mathbb{I}},\{W_I\}_{I\in\mathbb{I}},\kappa\right]}{nk_BT} &= -\ln\left(\frac{Q}{V}\right) \\ +\frac{1}{V}\int d^3r\;\frac{1}{2}\sum_{J\neq K\in\mathbb{I}}\chi_{JK}N\;\Phi_J(\vec{r})\Phi_K(\vec{r})-\sum_{I\in\mathbb{I}}W_I(\vec{r})\Phi_I(\vec{r})-\kappa(\vec{r})\left[1-\sum_{I\in\mathbb{I}}\Phi_I\right], \end{aligned} \tag{2.18}$$

where an irrelevant constant of one has been dropped compared to (2.16).

Now we introduce the mean-field approach to proceed in our treatment. This is done by employing the saddle-point approximation to (2.17). This means we leave out the integrals and insert the values $\{\phi_I\}_{I\in\mathbb{I}},\{w_I\}_{I\in\mathbb{I}},\kappa$ for which $F\left[\{\phi_I\}_{I\in\mathbb{I}},\{w_I\}_{I\in\mathbb{I}},\kappa\right]$ adopts a minimum. Note that lower-case letters label the fields yielding this minimum whereas their upper-case analogs represent the the general fields. This approximation is justified if the values for $F\left[\{\Phi_I\}_{I\in\mathbb{I}},\{W_I\}_{I\in\mathbb{I}},\kappa\right]$ are much greater than the thermal energy k_BT. Therefore we are left with

$$Z \propto \exp\left(-\frac{F\left[\{\phi_I\}_{I\in\mathbb{I}},\{w_I\}_{I\in\mathbb{I}},\kappa\right]}{k_BT}\right), \tag{2.19}$$

which shows that $F\left[\{\phi_I\}_{I\in\mathbb{I}}, \{w_I\}_{I\in\mathbb{I}}, \kappa\right]$ becomes the mean-field (or SCFT) approximation to the free energy of the melt. The minimum for $F\left[\{\Phi_I\}_{I\in\mathbb{I}}, \{W_I\}_{I\in\mathbb{I}}, \kappa\right]$ can be obtained by requesting that the functional derivatives, cf. definition (A.1), with respect to all arguments vanish when evaluated for the fields $\{\phi_I\}_{I\in\mathbb{I}}, \{w_I\}_{I\in\mathbb{I}}, \kappa$. From (2.18) we can see that setting the functional derivative of F with respect to W_I to zero yields

$$\phi_I(\vec{r}) = -V\frac{D\ln\left(Q\left[\{w_I\}_{I\in\mathbb{I}}\right]\right)}{Dw_I(\vec{r})}. \tag{2.20}$$

As we will show below, $\phi_I(\vec{r})$ is identified as the average I-segment concentration from n copolymers subject to external fields $\{w_I\}_{I\in\mathbb{I}}$. The derivative with respect to κ result in the incompressibility constraint

$$\sum_{I\in\mathbb{I}}\phi_I(\vec{r}) = 1. \tag{2.21}$$

Setting the remaining functional derivatives with respect to Φ_I to zero provides the self-consistent field conditions

$$w_I(\vec{r}) = \sum_{J\neq I}\chi_{IJ}N\ \phi_J(\vec{r}) + \kappa(\vec{r}). \tag{2.22}$$

By using equation (2.21) in (2.18) the minimum free energy reads

$$\frac{F\left[\{\phi_I\}_{I\in\mathbb{I}}, \{w_I\}_{I\in\mathbb{I}}, \kappa\right]}{nk_BT} = \frac{F_{Conf}}{nk_BT} + \frac{F_{int}}{nk_BT}, \tag{2.23}$$

with

$$\frac{F_{Conf}}{nk_BT} = -\ln\left(\frac{Q}{V}\right) - \frac{1}{V}\int d^3r\ \sum_{I\in\mathbb{I}} w_I(\vec{r})\phi_I(\vec{r}) \tag{2.24}$$

and

$$\frac{F_{int}}{nk_BT} = \frac{1}{V}\int d^3r\ \frac{1}{2}\sum_{J\neq K\in\mathbb{I}}\chi_{JK}N\ \phi_J(\vec{r})\phi_K(\vec{r}). \tag{2.25}$$

F_{Conf} is the configurational free energy which is given via the single molecule partition function minus the average contribution from the external fields. Since the single molecule partition function Q describes the statistics of a copolymer molecule in an external field w_I we end up with the pure configurational free energy by subtracting the average energetic contributions from this field. In effect, the external fields just serve to produce certain density fields for the polymer species ϕ_I whose configurational free energy is given by F_{Conf}.
The energetic contribution accounting for unfavorable contacts between different polymer species is given by F_{int} and stems from the expression introduced in (2.8).
Equation (2.22) leads to the simplest form of the minimum free energy (2.23),

$$\frac{F\left[\{\phi_I\}_{I\in\mathbb{I}}, \{w_I\}_{I\in\mathbb{I}}, \kappa\right]}{nk_BT} = -\ln\left(\frac{Q}{V}\right) - \frac{1}{V}\int d^3r\ \frac{1}{2}\sum_{J\neq K\in\mathbb{I}}\chi_{JK}N\ \phi_J(\vec{r})\phi_K(\vec{r}), \tag{2.26}$$

where we have w.l.o.g. set $\int d^3r\ \kappa(\vec{r}) = 0$.

In order to use equations (2.20, 2.21, 2.22) self-consistently to calculate the fields $\{\phi_I\}_{I\in\mathbb{I}}$, $\{w_I\}_{I\in\mathbb{I}}$, κ and with that the free energy $F\left[\{\phi_I\}_{I\in\mathbb{I}}, \{w_I\}_{I\in\mathbb{I}}, \kappa\right]$ of the melt, we need a way to calculate the single copolymer partition function $Q\left[\{w_I\}_{I\in\mathbb{I}}\right]$, which in turn depends on

the fields $\{w_I\}_{I\in\mathbb{I}}$. To this end we start with (2.14) and note that it contains expressions for the partition function of simple polymer chain of species I which are subject to the external field $w_I(\vec{r})$. More precisely we begin by looking at the partition function of the ιth polymer chain of species I, described by the curve $\vec{r}_{\alpha,I,\iota}(s)$, and assume its $s=0$ end is fixed at position $\vec{r}_0$ and its sNth segment is fixed at position $\vec{r}$. Therefore we have $\vec{r}_{\alpha,I,\iota}(0)=\vec{r}_0$ and $\vec{r}_{\alpha,I,\iota}(s)=\vec{r}$ with $0\leq s\leq f_{I,\iota}$. The partial partition function for this polymer chain fragment with two fixed points is

$$q_{I,\iota}(\vec{r},\vec{r}_0,s)\propto\int\tilde{D}\vec{r}_{\alpha,I,\iota}\exp\left(-\int_0^s dt\ w_I\left(\vec{r}_{\alpha,I,\iota}(t)\right)\right)\delta\left(\vec{r}_{\alpha,I,\iota}(0)-\vec{r}_0\right)\delta\left(\vec{r}_{\alpha,I,\iota}(s)-\vec{r}\right). \tag{2.27}$$

The integration is performed over all curves $\vec{r}_{\alpha,I,\iota}(t)$ with $0\leq t\leq s$. To account for the stretching entropy the configurations are again weighted similar to (2.10) with $\tilde{D}\vec{r}_{\alpha,I,\iota}=D\vec{r}_{\alpha,I,\iota}P[\vec{r}_{\alpha,I,\iota}]$ and

$$P[\vec{r}_{\alpha,I,\iota}]=\exp\left(-\frac{3}{2a_I^2N}\int_0^s dt\left|\frac{d}{dt}\vec{r}_{\alpha,I,\iota}(t)\right|^2\right). \tag{2.28}$$

(2.28) implies that in order for $q_{I,\iota}(\vec{r},\vec{r}_0,0)$ to be unequal to zero, forces $\vec{r}$ and $\vec{r}_0$ to coincide,

$$q_{I,\iota}(\vec{r},\vec{r}_0,0)\propto\delta\left(\vec{r}-\vec{r}_0\right). \tag{2.29}$$

It can be shown [48] that $q_{I,\iota}(\vec{r},\vec{r}_0,s)$ obeys a modified diffusion equation,

$$\frac{\partial}{\partial s}q_{I,\iota}(\vec{r},\vec{r}_0,s)=\left[\frac{a_I^2N}{6}\nabla^2-w_I(\vec{r})\right]q_{I,\iota}(\vec{r},\vec{r}_0,s). \tag{2.30}$$

Similarly we can define a partition function for the polymer chain where the other end at $s=f_{I,\iota}$ is fixed as well as the sNth segment as before. The partial partition function for the other fragment of the chain $\vec{r}_{\alpha,I,\iota}(t)$ running from $\vec{r}_{\alpha,I,\iota}(s)=\vec{r}$ to $\vec{r}_{\alpha,I,\iota}(f_{I,\iota})=\vec{r}_0$ in the interval $s\leq t\leq f_{I,\iota}$ is then, analogously to (2.27), given by

$$q^\dagger_{I,\iota}(\vec{r},\vec{r}_0,s)\propto\int\tilde{D}\vec{r}_{\alpha,I,\iota}\exp\left(-\int_s^{f_{I,\iota}} dt\ w_I\left(\vec{r}_{\alpha,I,\iota}(t)\right)\right)\delta\left(\vec{r}_{\alpha,I,\iota}(f_{I,\iota})-\vec{r}_0\right)\delta\left(\vec{r}_{\alpha,I,\iota}(s)-\vec{r}\right). \tag{2.31}$$

The probability distribution weighting the functional integral corresponds to (2.28) whereby the integration is performed over the interval $s\leq t\leq f_{I,\iota}$. This partition function also satisfies a modified diffusion equation similar to (2.30) but with a different sign,

$$\frac{\partial}{\partial s}q^\dagger_{I,\iota}(\vec{r},\vec{r}_0,s)=-\left[\frac{a_I^2N}{6}\nabla^2-w_I(\vec{r})\right]q^\dagger_{I,\iota}(\vec{r},\vec{r}_0,s). \tag{2.32}$$

The partial partition functions for a chain with a free end is simply obtained by integrating over the possible positions for the respective end,

$$q^{(\dagger)}_{I,\iota}(\vec{r},s)\equiv\int d^3r_0\ q^{(\dagger)}_{I,\iota}(\vec{r},\vec{r}_0,s). \tag{2.33}$$

Our choice for the proportionality factors so far deviates slightly from [48]. However, following the same conventions and thereby effectively setting a proportionality constant in the expressions for the partial partition functions leads to the boundary conditions $q_{I,\iota}(\vec{r},0)=1$

and $q^{\dagger}_{I,\iota}(\vec{r}, f_{I,\iota}) = 1$.

Turning back to the complete partition function for a single copolymer molecule we are now able to rewrite (2.14) using the partial partition functions (2.27, 2.31),

$$Q\left[\{w_I\}_{I\in\mathbb{I}}\right] = \int ... \int \left[\prod_{I,\iota} d^3r_{I,\iota;0}\; d^3r_{I,\iota}\; q_{I,\iota}(\vec{r}_{I,\iota}, \vec{r}_{I,\iota;0}, f_{I,\iota})\right] \times \delta\left(\{\vec{r}_{I,\iota;0}\}_{I,\iota}, \{\vec{r}_{I,\iota}\}_{I,\iota}\right). \tag{2.34}$$

Alternatively, each of the $q_{I,\iota}(\vec{r}, \vec{r}_0, f_{I,\iota})$ can be replaced by its corresponding $q^{\dagger}_{I,\iota}(\vec{r}, \vec{r}_0, 0)$ which describes the same chain the other way around. $\delta\left(\{\vec{r}_{I,\iota;0}\}_{I,\iota}, \{\vec{r}_{I,\iota}\}_{I,\iota}\right)$ encodes the architecture of the copolymer and is a product of delta functions of the form $\delta\left(\vec{r}_{I_1,\iota_1(;0)} - \vec{r}_{I_2,\iota_2(;0)}\right)$, which account for links between different polymer chains. For a free end no such delta function exits to restrict it, and hence the integration with respect to the position of this end can be performed as shown in (2.33).

Since the initial conditions for the partial partition function with free ends are known, the strategy is as follows. Starting with those chains the partial partition function can be calculated for these by using the initial conditions and the modified diffusion equations (2.30, 2.32). Next, we have to identify the links in the architecture which have already calculated partial partition functions "coming towards them". By using these partition functions, initial conditions for the next polymer chains can be calculated which can then again be used by the modified diffusion equation to calculate the partial partition functions for the whole chain. By recursively using this scheme all quantities can be calculated eventually. To keep track of this, we extend the use of the partial partition functions $q^{(\dagger)}_{I,\iota}(\vec{r}, s)$ from polymer chains with free ends to arbitrary chains where these functions describe the partition function of the respective fragment of the ith chain of species I *plus* the cumulated partition functions of chains "leading" to the respective segment at position $\vec{r}$.
Hence, in the case of diblock, triblock and even more complex molecules we have to account for two additional cases which tell us how to handle an end of a polymer chain which is not free but attached to other polymer chains.

In the simpler case, a polymer chain is attached end-to-end to a single other chain of a different species which is for example the case in diblock copolymers, see figure 2.2(a). Let us assume that the partition function for the "incoming" chain, $q_{I_2,\iota_2}(\vec{r}, s)$, is known. Let $q_{I_1,\iota_1}(\vec{r}, s)$ be the polymer chain "leaving" the node for which we want to obtain the initial condition. The partial partition function $q_{I_1,\iota_1}(\vec{r}, s)$ describing the *part* of the copolymer which stretches from some of its free ends to the sth segment of the ι_1th chain of species I_1 at position $\vec{r}$ is, similarly to (2.34), given by

$$q_{I_1,\iota_1}(\vec{r}, s) \equiv \int d^3r_{I_1,\iota_1;0} \int d^3r_{I_2,\iota_2}\; q_{I_1,\iota_1}(\vec{r}, \vec{r}_{I_1,\iota_1;0}, s) q_{I_2,\iota_2}(\vec{r}_{I_2,\iota_2}, f_{I_2,\iota_2})\; \delta\left[\vec{r}_{I_1,\iota_1;0} - \vec{r}_{I_2,\iota_2}\right], \tag{2.35}$$

where the delta function describes the connection between the two chains. Due to (2.29) we obtain in the limit $s \to 0$, $q_{I_1,\iota_1}(\vec{r}, 0) = q_{I_2,\iota_2}(\vec{r}, f_{I_2,\iota_2})$. Analogously, one obtains similar conditions for the partial partition functions describing the other part of the molecule. In the example of figure 2.2(a) for example, $q^{\dagger}_{I_2,\iota_2}(\vec{r}, f_{I_1,\iota_1}) = q^{\dagger}_{I_1,\iota_1}(\vec{r}, 0)$. Also, connecting a $s = 0$ end to a $s = 0$ end of another chain or a $s = f_{I_1,\iota_1}$ to a $s = f_{I_2,\iota_2}$ end would simply result in

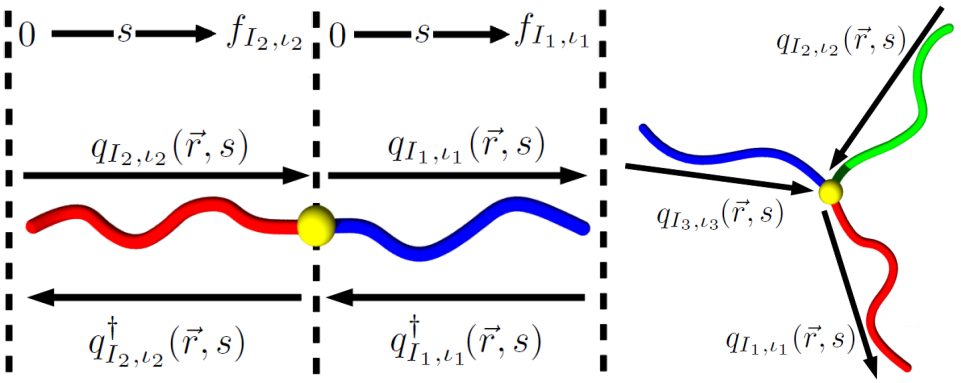

Figure 2.2: Representation of the method to obtain the partial partition functions $q_{I,\iota}(\vec{r},s)$ and $q^\dagger_{I,\iota}(\vec{r},s)$ for different types of links present in complex copolymer architectures. (a) A diblock copolymer yields a link between two distinct chains. The evolution of s, which parametrizes the individual polymer chains, is shown at the top of the picture. The direction of the forward-integration of the respective partial partitions is also indicated. (b) Links between three distinct chains, inherent to e.g. triblock star-copolymers, require two partial partition functions to be known at the common node (indicated by incoming arrows) in order to obtain the initial condition for the remaining partial partition function (outgoing arrow).

expressions such as $q_{I_1,\iota_1}(\vec{r},0) = q^\dagger_{I_2,\iota_2}(\vec{r},0)$ and $q_{I_2,\iota_2}(\vec{r},0) = q^\dagger_{I_1,\iota_1}(\vec{r},0)$ for the $s = 0$ connection or $q^\dagger_{I_1,\iota_1}(\vec{r},f_{I_1,\iota_1}) = q_{I_2,\iota_2}(\vec{r},f_{I_2,\iota_2})$ and $q^\dagger_{I_2,\iota_2}(\vec{r},f_{I_2,\iota_2}) = q_{I_1,\iota_1}(\vec{r},f_{I_1,\iota_1})$ in the other case.

In the next complex case, we allow three polymer chains to meet at a common node, see figure 2.2(b). Let $q_{I_2,\iota_2}(\vec{r},s)$ and $q_{I_3,\iota_3}(\vec{r},s)$ by known "incoming" partial partition functions whose two chains merge with a third chain at a common node. The partial partition function "leaving" the node along the third chain is denoted $q_{I_1,\iota_1}(\vec{r},s)$. Its function obeys

$$q_{I_1,\iota_1}(\vec{r},s) \equiv \int d^3r_{I_1,\iota_1;0} \int d^3r_{I_2,\iota_2} \int d^3r_{I_3,\iota_3}\; q_{I_1,\iota_1}(\vec{r},\vec{r}_{I_1,\iota_1;0},s) q_{I_2,\iota_2}(\vec{r}_{I_2,\iota_2},f_{I_2,\iota_2}) \times q_{I_3,\iota_3}(\vec{r}_{I_3,\iota_3},f_{I_3,\iota_3})\; \delta\left[\vec{r}_{I_1,\iota_1;0} - \vec{r}_{I_2,\iota_2}\right] \delta\left[\vec{r}_{I_2,\iota_2} - \vec{r}_{I_3,\iota_3}\right]. \tag{2.36}$$

The limit $s \to 0$ shows $q_{I_1,\iota_1}(\vec{r},0) = q_{I_2,\iota_2}(\vec{r},f_{I_2,\iota_2}) q_{I_3,\iota_3}(\vec{r},f_{I_3,\iota_3})$. Linking the ends of the chains in a different fashion results in similar expression, analogously to the previous case. Note that nodes linking more than three polymer chains can simply be seen as multiple links of three chains.

With that the partial partition functions describe the whole copolymer molecule up to a certain segment of one of its polymer chains. There is always a partial partition function describing exactly the other part of the molecule and ending in the same point as the first one. Figure 2.3 shows this for a complex architecture where $q_{I,\iota}(\vec{r},s)$ accumulates information from the lower part of the molecule and $q^\dagger_{I,\iota}(\vec{r},s)$ describes the upper part. Both partial partition functions meet at the sNth segment of the ith chain of species I at position $\vec{r}$. Accounting for all possible positions for $\vec{r}$, the total partition function of the copolymer is then simply given by multiplying both partial partition functions and integrating with

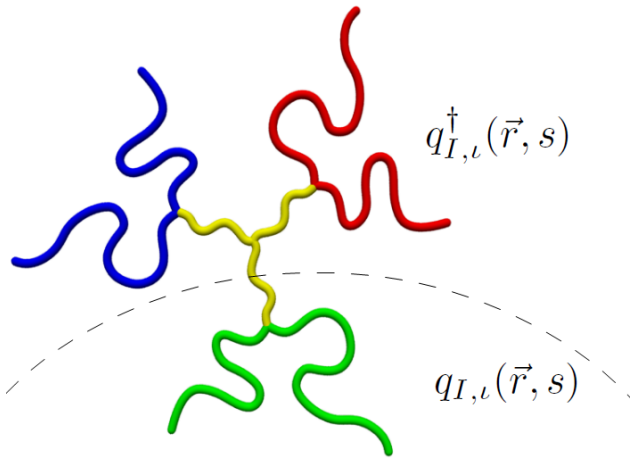

Figure 2.3: Complex copolymer architecture, consisting of different types of polymer chains and multiple links. Starting with the known initial conditions for the partial partition functions, $q_{I,\iota}(\vec{r},s)$ and $q^{\dagger}_{I,\iota}(\vec{r},s)$, at the free ends of the copolymer, these functions can be integrated forward along the chains and, accounting for the connections within the architecture, will eventually be evaluated for the whole molecule. At each point of the copolymer, defined by I, ι and s, a partial partition function, $q_{I,\iota}(\vec{r},s)$, describing part of the molecule (in the illustrated case the lower part) meets another partial partition function, $q^{\dagger}_{I,\iota}(\vec{r},s)$, describing the other (upper) part. In the picture, this division into two parts is indicated by the dashed circular arc.

respect to $\vec{r}$,

$$Q\left[\{w_I\}_{I\in\mathbb{I}}\right] = \int d^3r\; q_{I,\iota}(\vec{r},s)q^{\dagger}_{I,\iota}(\vec{r},s). \tag{2.37}$$

The partition function depends on the fields $\{w_I\}_{I\in\mathbb{I}}$ since these enter into the modified diffusion equations for the partial partition functions. Note that the polymer chain and the precise segment where the partial partition functions meet is arbitrary and hence Q is independent of the choice for I, ι and s. Next, we calculate the *average* segment distribution of each copolymer, $\phi_\alpha(\vec{r})$. In our mean-field approximation this can be done by looking at a single copolymer subject to the fields $\{w_I\}_{I\in\mathbb{I}}$. According to statistical mechanics, we weight the segment concentration of each configuration by the respective Boltzmann factor,

$$\phi_{\alpha,I}(\vec{r}) = \frac{1}{Q}\int \tilde{D}\vec{r}_\alpha\; \hat{\phi}_{\alpha,I}(\vec{r}) \exp\left(-\sum_{J\in\mathbb{I}}\sum_{j=1}^{J^{max}}\int_0^{f_{J,j}} ds\; w_J\left(\vec{r}_{\alpha,J,j}(s)\right)\right). \tag{2.38}$$

Inserting the segment concentration (2.4) yields

$$\begin{aligned}\phi_{\alpha,I}(\vec{r}) =& \frac{N}{\rho_0 Q}\sum_{\iota=1}^{I^{max}}\int_0^{f_{I,\iota}} ds \int \tilde{D}\vec{r}_\alpha\ \delta\left(\vec{r}-\vec{r}_{\alpha,I,\iota}(s)\right) \\ &\times \exp\left(-\sum_{J\in\mathbb{I}}\sum_{j=1}^{J^{max}}\int_0^{f_{J,j}} ds\ w_J\left(\vec{r}_{\alpha,J,j}(s)\right)\right) \\ =& \frac{N}{\rho_0 Q}\sum_{\iota=1}^{I^{max}}\int_0^{f_{I,\iota}} ds\ q_{I,\iota}(\vec{r},s)q^\dagger_{I,\iota}(\vec{r},s).\end{aligned} \tag{2.39}$$

Alternatively, by employing (2.38) and looking at the second line in (2.14), we see that the functional derivative of $\ln(Q)$ with respect to $w_I(\vec{r})$ yields $\phi_{\alpha,I}(\vec{r}) = -\frac{N}{\rho_0}\frac{D\ln(Q)}{Dw_I(\vec{r})}$. In the mean-field approximation, we can conclude from definition (2.5) that $\phi_I = n\phi_{\alpha,I}$. With (2.3) we end up with $\phi_I(\vec{r}) = -V\frac{D\ln(Q)}{Dw_I(\vec{r})}$, which in fact identifies the self-consistent fields $\phi_I(\vec{r})$ in (2.20) with the average I-segment concentration.

We have demonstrated the derivation of the self-consistent equations (2.20, 2.21, 2.22) which define the fields used in the calculation of the mean-field free energy (2.26). A way to numerically calculate the self-consistent fields and with that the free energy of a microstructure with predetermined symmetry is presented in chapter 2.3. Having calculated the free energy of different candidate morphologies and of the homogeneous, disordered state, we are able to identify the structure with the lowest free energy as the equilibrium state of the melt. For high enough segregation strength this will not be the disordered state but rather an ordered microphase. Note that the mean-field treatment ignores fluctuation effects which become increasingly important in the weak segregation limit. The biggest deviations to the mean-field treatment are expected to occur near the transition between an ordered phases and the disordered phase. However, for well segregated structures fluctuations are negligible and the SCFT allows for a quantitative comparison between different morphologies in order to determine the equilibrium solution.

2.2 Strong segregation theory

In the limit of strong segregation, meaning χN is much larger than the values needed to form ordered phases, there are further useful approximations to the SCFT. We would like to show the expressions of this strong segregation theory (SST) in more detail since these will result in formulas which will allows us to link a structures geometry and the molecular architecture of its constituents to its free energy. The SST is hence invaluable for choosing molecular architectures and candidate structures which allow for self-assembly of the desired complex morphologies we are interested in.
In this limit, the free energy of block copolymer melts can be split into two contributions. The first contribution is due to the interfacial free energy which describes the energetic contributions arising from the interfaces between immiscible species. An evaluation of this part of the free energy can be achieved by looking at the case of an interface between immiscible homopolymers [28, 26]. Corrections, for example due to the connectivity of chains in block copolymers, can be discussed [75, 21] but vanish in the limit $\chi N \to \infty$ and are neglected in order to simplify the problem.
Secondly, we have to account for the stretching energy of polymer chains originating from

the need that the polymers fill space evenly in their incompressible melts state under the constraint that junction points between different polymer chains are confined to the thin interfacial regions. This corresponds to the problem of a brush of flexible polymer chains tethered to an interface. The strong segregation limit also implies a strong stretching of these chains which allows us to evaluate the corresponding free energies analytically, thereby completing the SST together with the free energies of the interfaces [74].

To evaluate the free energy of an interface let us start by looking at the operators involved in the modified diffusion equations for the partial partition functions, e.g. (2.30). For simplicity, we will only look at a single polymer chain of only one species, i.e. the case of a homopolymer, which allows us to drop the indexes I and ι in (2.30). Firstly, we are interested in the configurational free energy penalty of the homopolymer statistics due to the interface. Let us assume that we can solve the eigenvalue problem involving the operator of the modified diffusion equation for the scenario described,

$$\left[\frac{Na^2}{6}\nabla^2 - \omega(\vec{r})\right] g_i(\vec{r}) = -\gamma_i g_i(\vec{r}). \tag{2.40}$$

Hence, we know all eigenvalues γ_i and eigenfunctions $g_i(\vec{r})$, where $i = 0, 1, 2, ...$ Let the the eigenvalues and eigenfunctions be arranged in such a way that the eigenvalues are ordered from smallest to largest. The eigenfunctions can be chosen to be orthonormal,

$$\frac{1}{V}\int d^3r\ g_i(\vec{r})g_j(\vec{r}) = \delta_{ij}. \tag{2.41}$$

Since the eigenfunctions form a complete basis, we can expand any spatial function, and the spatial part of the partial partition function in particular, as

$$q(\vec{r}, s) = \sum_{i=0}^{\infty} q_i(s)g_i(\vec{r}). \tag{2.42}$$

Using (2.40), (2.41) and (2.42) we see that the modified diffusion equation (2.30) transforms to

$$q_i'(s) = -\gamma_i q_i(s), \tag{2.43}$$

for all $i = 0, 1, 2, ...$, yielding the solution

$$q(\vec{r}, s) = \sum_{i=0}^{\infty} q_i(0)\exp(-\gamma_i s)g_i(\vec{r}). \tag{2.44}$$

Similarly, (2.32) results in

$$q^\dagger(\vec{r}, s) = \sum_{i=0}^{\infty} q_i^\dagger(1)\exp(-\gamma_i(1-s))g_i(\vec{r}). \tag{2.45}$$

For high molecular weight polymers the expansions for $q(\vec{r}, s)$ in (2.44) and for $q^\dagger(\vec{r}, s)$ in (2.45) become increasingly dominated by the first term corresponding to the eigenvalue γ_0 [48]. Hence we can employ the approximations

$$q(\vec{r}, s) \approx q_0(0)\exp(-\gamma_0 s)g_0(\vec{r}) \tag{2.46}$$

and

$$q^\dagger(\vec{r}, s) \approx q_0^\dagger(1)\exp(-\gamma_0(1-s))g_0(\vec{r}). \tag{2.47}$$

Using these expressions the partition function for the entire copolymer, (2.37) simplifies to

$$Q\left[\{w_I\}_{I\in\mathbb{I}}\right] \approx V q_0(0) q_0^\dagger(1) \exp\left(-\gamma_0\right). \tag{2.48}$$

Analogously, using these approximations, the segment concentrations (2.39) can easily be calculated,

$$\phi_\alpha(\vec{r}) \approx \frac{N}{\rho_0 V} g_0^2(\vec{r}). \tag{2.49}$$

For n molecules we then have

$$\phi(\vec{r}) \approx g_0^2(\vec{r}). \tag{2.50}$$

From (2.50) we can express the concentration gradients as

$$\nabla\phi(\vec{r}) \approx 2 g_0(\vec{r}) \nabla g_0(\vec{r}). \tag{2.51}$$

By looking at (2.40) for $i = 0$, multiplying it by $g_0(\vec{r})$ and integrating over V, we obtain

$$\int d^3r\ w(\vec{r})\phi(\vec{r}) \approx \frac{Na^2}{6} \int d^3r\ g_0(\vec{r})\nabla^2 g_0(\vec{r}) + V\gamma_0. \tag{2.52}$$

Inserting (2.48) and (2.52) in (2.24) gives an expression for the configurational free energy of a homopolyer chain of high molecular weight near an interface,

$$\frac{F_{Conf}}{nk_BT} \approx -\frac{Na^2}{6V} \int d^3r\ g_0(\vec{r})\nabla^2 g_0(\vec{r}) - \ln\Big(q_0(0) q_0^\dagger(1)\Big). \tag{2.53}$$

Neglecting the logarithmic term in the high molecular weight limit and performing a partial integration allows us to write

$$\frac{F_{Conf}}{nk_BT} \approx \frac{Na^2}{6V} \int d^3r\ \left|\nabla g_0(\vec{r})\right|^2, \tag{2.54}$$

where we have assumed that the gradient of the concentration profiles vanishes at the boundaries, $\nabla\phi|_{\partial V} = 0$. With (2.50) and (2.51) we can express the configurational free energy solely via the concentration profiles,

$$\frac{F_{Conf}}{nk_BT} \approx \frac{Na^2}{24V} \int d^3r\ \frac{\left|\nabla\phi(\vec{r})\right|^2}{\phi(\vec{r})}. \tag{2.55}$$

Suppose we have an interface between two immiscible homopolymers of species A and B. We use (2.55) as the configurational free energy expression for each of the two polymer species involved. For the contact free energy at the interface we employ the usual form given in (2.25) and restrict ourselves to the case of only two species A and B and hence a single parameter χ_{AB}. The total free energy is then, similarly to (2.23), given by the sum of both configurational free energies and the interfacial contact free energy,

$$\frac{F}{nk_BT} = \frac{Na^2}{24V} \int d^3r\ \left(\frac{\left|\nabla\phi_A(\vec{r})\right|^2}{\phi_A(\vec{r})} + \frac{\left|\nabla\phi_B(\vec{r})\right|^2}{\phi_B(\vec{r})}\right) + \frac{1}{V}\int d^3r\ \chi_{AB}N\ \phi_A(\vec{r})\phi_B(\vec{r}). \tag{2.56}$$

For simplicity, we have assumed the same statistical segment length a for both polymer species. However, a more general treatment is also possible [27]. Since we are interested in the strong segregation limit, where the width of the interfaces is small compared to the size of the domains, we can neglect the curvature of the interface. This enables us to consider

the interface as being flat and renders the problem effectively one-dimensional allowing us to simplify the integrals in (2.56). Upon choosing the mid-plane of the interface to coincide with the $z = 0$ plane of the coordinate system we get

$$\frac{F}{nk_BT} = \frac{Na^2}{24L}\int dz\ \left(\frac{|\phi_A'(z)|^2}{\phi_A(z)} + \frac{|\phi_B'(z)|^2}{\phi_B(z)}\right) + \frac{1}{L}\int dz\ \chi_{AB}N\ \phi_A(z)\phi_B(z), \tag{2.57}$$

where the integration ranges from $z = -\frac{L}{2}$ to $z = \frac{L}{2}$. Let us assume that the positive half space is filled with polymer species A and the negative half space is occupied by species B. At large enough distances from the interface, we will hence have only monomers of species A on one side, $\phi_A(z = \frac{L}{2}) = 1$, and vanishing concentration on the other side, $\phi_A(z = -\frac{L}{2}) = 0$. Ultimately, L can be extended to infinity. By virtue of the systems incompressibility we can, in absence of any other polymer species, write $\phi_B(z) = 1 - \phi_A(z)$. Additionally, we use the substitution $\phi_A(z) = \sin^2(\Theta(z))$ which recasts the free energy expression of (2.57) as

$$\frac{F}{nk_BT} = \frac{1}{L}\int dz\ \left(\frac{Na^2}{6}\left[\Theta'(z)\right]^2 + \chi_{AB}N\sin^2(\Theta(z))\cos^2(\Theta(z))\right). \tag{2.58}$$

The boundary conditions are $\Theta(z = -\frac{L}{2}) = 0$ and $\Theta(z = \frac{L}{2}) = \frac{\pi}{2}$. We wish to minimize (2.58) with respect to the function $\Theta(z)$. The minimum is given by means of the Euler-Lagrange equation,

$$\frac{Na^2}{3}\Theta''(z) - \frac{\chi_{AB}N}{2}\sin(4\Theta(z)) = 0. \tag{2.59}$$

Multiplying (2.59) by $\Theta'(z)$ leads to

$$\frac{Na^2}{6}\left[\Theta'(z)\right]^2 - \chi_{AB}N\sin^2(\Theta(z))\cos^2(\Theta(z)) = \text{const.} \tag{2.60}$$

The boundary conditions for $\Theta(z)$ and the fact that the profile becomes flat at large enough distances from the interface imply that the constant of integration in (2.60) must be zero. Thus it follows from (2.60) that

$$w_{AB}\Theta'(z) = 2\sin(\Theta(z))\cos(\Theta(z)), \tag{2.61}$$

where we have defined

$$w_{AB} \equiv \frac{2a}{\sqrt{6\chi_{AB}}}. \tag{2.62}$$

It is possible to express (2.61) via the original concentration profile $\phi_A(z)$,

$$w_{AB}\phi_A'(z) = 4\phi_A(z)\left[1 - \phi_A(z)\right]. \tag{2.63}$$

We can solve (2.63) by separation of variables. Setting $\phi_A(z = 0) = \frac{1}{2}$ we get

$$\phi_A(z) = \frac{1}{2}\left[1 + \tanh\left(\frac{2z}{w_{AB}}\right)\right]. \tag{2.64}$$

This is the concentration profile in the vicinity of the interface from which we see that w_{AB} is an appropriate measure for the width of the interface. Figure 2.4 shows a schematic representation of a diblock copolymer lamellar microdomain and a plot of its concentration profiles. The profile in the interfacial region is characterized by the shape of the tanh function.

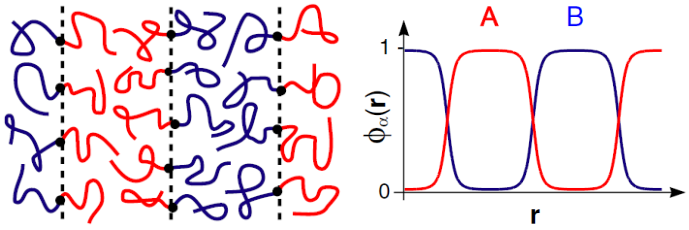

(a) (b)

Figure 2.4: (a) Schematic representation of a lamellar microdomain structure in a diblock copolymer melt. (b) Concentration profiles of both polymer species. The shape of the profiles in the interfacial regions is characterized by the tanh function. The pictures have been taken from [47].

Inserting (2.64) into (2.57) gives the total free energy of the interface,

$$\frac{F}{nk_BT} = \frac{Na}{L}\sqrt{\frac{\chi_{AB}}{6}}. \tag{2.65}$$

Since the free energy of the individual bulk phases, which are separated by the interfacial region, is zero in the strong segregation limit, we can derive an interfacial tension γ_{AB} from (2.65). The interfacial tension is simply defined to be the free energy per area arising from the interface. Hence, the interfacial tension per copolymer and in units of k_BT is given by

$$\frac{\gamma_{AB}}{nk_BT} = \frac{Na}{V}\sqrt{\frac{\chi_{AB}}{6}}. \tag{2.66}$$

Although we have performed the calculation for the case of two immiscible species of homopolymes, these concepts can be extended to interfaces between the immiscible chains of block copolymers, whereby the junction points of the copolymers are confined to the interfacial region. Corrections due to the connectivity of the blocks and other effects are discussed in, for example, [75, 21]. As it turns out, to a first order approximation the derivation is the same as has been shown here, although there are corrections to e.g. the interfacial width for finite segregation strength, especially due to the connectivity of chains. For simplicity, we will stick with the simpler formulas, which become valid in the limit $\chi N \to \infty$, and use (2.66) to calculate the free energy contributions arising from all interfaces in the investigated morphologies, regardless of whether there are connections between the immiscible polymer chains present or not.

In order to understand the formation of morphologies in block copolymers we have to take another contribution to the free energy, besides the interfaces we have just discussed, into account. This is due to the circumstance that polymer chains are highly stretched away from the interfaces where their junction points are confined. This high stretching allows us to derive analytical expressions for the free energy of a block copolymer melt [74]. A good introduction to this contribution is found in [22].
For simplicity let us imagine a brush of highly stretched polymer chains of a single species attached to an interface. Eventually, we will use this picture and the conclusions we can derive from it to calculate all stretching contributions within our copolymer morphologies. For the moment, we refrain from the mean-field description of the free energy in (2.23) and simply look at the configurational free energy of the Gaussian chain model in absence of

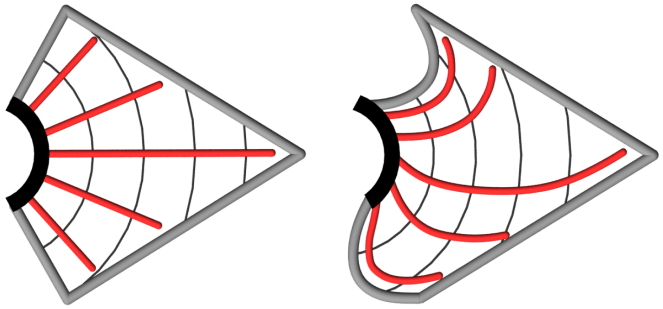

(a) (b)

Figure 2.5: Polymer brushes involved in microphases of block copolymer melts. The bold black curves indicate grafting surfaces of the brushes which corresponds to the interfacial regions between distinct but connected polymer species. Besides these grafting surfaces, there may be additional surfaces (shown in grey) confining the polymer brush. In block copolymer melts, these surfaces can form in order to separate distinct polymer species which are not directly connected by covalent bonds. This is for example the case in triblock star-copolymers. Red curves illustrate typical coarse-grained polymer paths. The polymeric path distance, $z(\vec{r})$, is defined as the distance between a point in the polymer brush at position $\vec{r}$ and an associated point on the grafting surface, measured along the polymer path which connects both points. The thin circular arcs in the polymer brush indicate surfaces whose points are located at a certain polymeric path distance z away from the grafting surface. Their surface areas are denoted as $A(z)$. (a) In absence of any constraints, the polymer paths can be chosen as the shortest connection between the points in the brush and the interface, thereby minimizing the stretching contribution to the free energy. (b) Due to their confinement, the polymers have to adopt curved paths which are dictated by the curved boundary surfaces. Note that this means that the surfaces at a given polymeric path distance z lie closer (w.r.t. the standard euclidean distance) to the grafting surface when compared to (a).

any interface contributions. In the strong stretching limit, we can associate each polymer chain with a fixed coarse-grained path, thereby neglecting fluctuations about it, provided the end points of this path are known. Usually, these paths were assumed to be straight and perpendicular to the surface where the fixed ends are attached, which is true for the simpler morphologies found in diblock copolymer melts. However, extensions to this crude assumption have been pointed out [42]. For our complex morphologies we have to allow for the possibility of non-perpendicular paths which can also be curved. This becomes already evident by noting that the domains, which polymer chains of the individual species are confined to, are not necessarily convex objects. Polymer chains in the melt state have to obey these boundary conditions, forcing them to take a curved path. To be consistent with literature, we define the distance between the interface to which the polymers are tethered and an arbitrary point in their domain by measuring the length along the polymeric path which runs from the respective point in the volume to the point at the interface where it is attached. Henceforth, we label this *polymer path distance* by z. Figure 2.5 provides two examples of domains, showing the possibility of both straight and curved polymer paths.

Consider a trajectory $z(z_0, s)$, starting at the interface at $z = 0$, which runs to a distance $z = z_0$ away from the interface. $z(z_0, s)$ describes the distance of the sNth segment of

the polymer chain from the interface, measured along the polymer chain. The free energy associated with this path is, in accordance with the probability of a coarse-grained trajectory, stated in (2.10), given by

$$\frac{f_{Conf,z_0}}{k_BT} \equiv \int_0^f ds\ \frac{3}{2a^2N} \left| \frac{dz}{ds}(z_0,s) \right|^2, \tag{2.67}$$

where we have assumed that each chain has fN segments and utilized that the stretching of the polymer chain occurs along z. The total configurational (or stretching) free energy is then given by adding the free energies of all chains. To calculate this, let $g(z_0)dz_0$ be the number of chains whose free ends are located a polymeric path distance between z_0 and $z_0 + dz_0$ away from the interface. With this, the configurational free energy reads [74]

$$\frac{F_{Conf}}{k_BT} \equiv \int_0^L dz_0\ g(z_0) \int_0^f ds\ \frac{3}{2a^2N} \left| \frac{dz}{ds}(z_0,s) \right|^2, \tag{2.68}$$

where L is the maximum distance of a point in the domain to the interface, measured along the polymer trajectories as before.
There are two additional conditions which we have to enforce. First of all, each polymer chain consists of fN segments. We can write this condition as

$$\int_{z_0}^0 dz\ \frac{ds}{dz}(z_0,z) = f. \tag{2.69}$$

Note, that we have chosen the free end at distance $z = z_0$ to be described by the $s = 0$ end of the chain, whereas the fixed end located at $z = 0$ is given by $s = f$. Here $s(z_0, z)$ is the function describing which segment of the polymer chain with total extension z_0 is located at height $z < z_0$. It can be obtained by inverting $z(z_0, s)$. Condition (2.69) is of course only true for a monodisperse distribution of polymer chain lengths. This will, however, be the case for all architectures examined in this thesis and simplifies the treatment of the configurational entropy.
The second condition is the incompressibility of the melt. Previously, we started by employing delta distributions involving the monomer concentrations to enforce this condition. Here we use a more geometric way to express the incompressibility. Let $A(z)$ be the area of the surface defined by the points with distance z from the interface, see figure 2.5 for an example. The incompressibility of the melt enforces that the number of segments in the volume between the surface at distance z and the surface at distance $z + dz$ is given by $\rho_0 A(z)dz$. On the other hand, we get an expression for the number of segments in this volume by considering the polymer chains described by their trajectories $z(z_0, s)$ and the free end distribution $g(z_0)$. We utilize that $-N\frac{ds}{dz}(z_0, z)\,dz$ is the number of segments deposited at a distance between z and $z + dz$ by a chain with free end at distance z_0, whereby $z < z_0$. Accounting for all chains which contribute to the deposition of segments at this distance, i.e. chains which have free ends at a distance greater than z, we can calculate the total number of segments at distances between z and $z + dz$. Equating this with the expression involving the area at distance z leads to

$$-\frac{N}{\rho_0} \int_z^L dz_0\ g(z_0) \frac{ds}{dz}(z_0,z) = A(z). \tag{2.70}$$

Essentially, we are left with the task of minimizing the free energy (2.68) with respect to the free end distribution $g(z_0)$ and the trajectories $z(z_0, s)$ under the additional conditions

(2.69) and (2.70). Instead of performing this minimization directly [74] we present another approach [59]. The first step is to introduce an external potential field $w(z)$ acting on the polymers, as has already been employed in the previous section, which is a function of the polymer path distance z. The coupled choice for $w(z)$ and $g(z_0)$ must ensure that the constraints for the lengths of chains (2.69) and the incompressibility of the melt (2.70) are met while simultaneously minimizing the free energy of the system. Adding the external field to (2.67) defines

$$\frac{f_{z_0}}{k_B T} \equiv \int_0^f ds \; \frac{3}{2a^2 N} \left| \frac{dz}{ds}(z_0, s) \right|^2 + w\left(z(z_0, s)\right). \tag{2.71}$$

We are interested in the mean path a polymer chain takes going from distance $z = z_0$ at $s = 0$ to $z = 0$ at $s = f$. This path is given by minimization of (2.71) for the corresponding external potential $w(z)$. In order to obtain this trajectory we employ the Euler-Lagrange equations which yields

$$\frac{3}{a^2 N} \frac{d^2}{ds^2} z(z_0, s) - \frac{d}{dz} w\left(z(z_0, s)\right) = 0. \tag{2.72}$$

The procedure of involving the external potential is convenient because we can derive its form by assuming that if all polymer chains are in mechanical equilibrium, there would be no tension at their free ends [59], i.e.

$$\frac{dz}{ds}(z_0, 0) \stackrel{!}{=} 0. \tag{2.73}$$

Hence, all chains start with vanishing stretch and, by virtue of (2.69), have to reach the grafting surface at $z = 0$ exactly after fN coarse-grained segments. Therefore, the potential $w(z)$ has to be an equal-time potential. This can be seen from (2.72) by making the analogy with a particle at rest at "time" $s = 0$, but starting from arbitrary "height" $z = z_0$, "falling" in a potential $w(z)$. Since the particle has to reach the interface at $z = 0$ precisely at "time" $s = f$, we know from classical mechanics that this equal-time potential is a parabola,

$$w(z) = -\frac{B}{2} z^2, \tag{2.74}$$

where we have dropped any constant terms since these would drop out in the following considerations anyways. From (2.72) and the assumed initial conditions we see that the polymer trajectories are given by

$$z(z_0, s) = z_0 \cos\left(\sqrt{\frac{BNa^2}{3}} s \right). \tag{2.75}$$

Since we require the path to fulfill $z(z_0, f) = 0$ we conclude

$$\sqrt{\frac{BNa^2}{3}} = \frac{\pi}{2f}. \tag{2.76}$$

Exploiting the analogy with classical mechanics again, we see from (2.71) and (2.75) that we essentially integrate over a quarter period of an oscillating trajectory and are therefore able to identify the integral over $\frac{3}{2a^2N} \left| \frac{dz}{ds} \right|$ with the integral over $-w\left(z(z_0, s)\right)$, which can easily be seen by inserting (2.74) and (2.75) into these expressions. This implies that f_{z_0}, as defined in (2.71), vanishes for all end-point positions z_0. It can be shown that this

corresponds to a minimization with respect to the end-point distribution $g(z_0)$ [59, 44]. With the identification of both integrals, we are also able to calculate the actual stretching free energy (2.67) of a single chain with a given free end-position,

$$\begin{aligned}\frac{f_{Conf,z_0}}{k_BT} &\equiv \int_0^f ds\ \frac{3}{2a^2N}\left|\frac{dz}{ds}(z_0,s)\right|^2 = \frac{3\pi^2}{8f^2Na^2}\int_0^f ds\ z^2(z_0,s) \\ &= -\frac{3\pi^2}{8f^2Na^2}\int_0^{z_0} dz\ z^2\frac{ds}{dz}(z_0,z)\,,\end{aligned} \tag{2.77}$$

where we have used (2.74) and (2.76) in the first step. We are now able to find a new expression [44] for the configurational free energy (2.68),

$$\begin{aligned}\frac{F_{Conf}}{k_BT} &= -\frac{3\pi^2}{8f^2Na^2}\int_0^L dz_0\ g(z_0)\int_0^{z_0} dz\ z^2\frac{ds}{dz}(z_0,z) \\ &= -\frac{3\pi^2}{8f^2Na^2}\int_0^L dz_0\ \int_0^L dz\ \Theta(z_0-z)g(z_0)z^2\frac{ds}{dz}(z_0,z) \\ &= -\frac{3\pi^2}{8f^2Na^2}\int_0^L dz\ \left(\int_z^L dz_0\ g(z_0)\frac{ds}{dz}(z_0,z)\right)z^2 \\ &= \frac{3\pi^2\rho_0}{8f^2N^2a^2}\int_0^L dz\ A(z)z^2 = \frac{3\pi^2 n}{8f^2Na^2V}\int_{V_I} d^3r\ z^2,\end{aligned} \tag{2.78}$$

where we have used the incompressibility constraint (2.70) in the second to last step. The integration in the final expression is performed over the whole volume of the respective domain V_I, which is filled by the (stretched) polymer chains. As has been discussed, z is the distance between the volume elements in V_I and the grafting surface, measured along the respective polymer trajectory which connects the respective volume element to a specific point on the surface. Equation (2.78) is a geometric measure for the free energy contribution due to the stretching of polymer chains in a given morphology. In this instance, we have derived it for the case of a incompressible melt. It is precisely this formula, on which we will base our argumentation for the existence of novel phases in triblock star-copolymers in chapter 4.

We would like to mention that the outlined derivation has been introduced in [59] for grafted polymers in a solvent. In this case, the potential arose due to excluded-volume effects of the polymer chains which contributed to the free energy. For our incompressible melt, we do not have free energy contributions of exactly this form, but rather utilize the potential in its simple parabolic shape to facilitate the expression for the free energy. We would like to mention that there are also attempts to identify corrections to the presented strong stretching theory using a more rigorous derivation of the formulas we presented in this section based on the mean-field approximation that has been established in last section [21, 61].

While (2.78) provides a very good approximation for highly stretched chains, there are still some limitations that come with it. Although this formula works well for polymers grafted to a flat interface or to the concave side of a curved interface, applying it to the convex side of a curved interface results in the unwanted occurrence of negative values of $g(z_0)$ when z_0 lies below a certain value. This would imply an unphysical negative density of free ends near the grafting surface rendering the applicability of (2.78) questionable. To overcome this, $g(z_0)$ must be chosen non-negative throughout the brush, leading to a certain

region near the grafting surface being void of any free ends, see e.g. [74]. This region is called the exclusion zone. Maybe surprisingly, an examination of the consequences of this exclusion zone for cylindrical brushes shows, however, that the analytical continuation of (2.78) for convex brushes provides a very good approximation for all but the most extremely curved surfaces [3]. A discussion of the magnitude and effect of the exclusion zone for various conditions can be found in [3, 5]. Hence we will continue to use (2.78) for our purposes since we will ultimately deal to a good approximation with cylindrical surfaces with reasonable curvatures.
Another approximation allowing for an analytical evaluation of the stretching contribution suited for the convex sides of strongly curved surfaces would be to assume that all free ends are located at the outermost distance from the interface [74]. However, the validity of this assumption quickly deteriorates for only moderately curved surfaces.

Besides the limitation due to the exclusion zone, one also has to account for the connectivity of different chains in a copolymer. This means that the minimization of the free energies (2.78) for different domains cannot be performed independently. More precisely, the local grafting densities at the interface between different domains have to be consistent with the copolymer architecture. In simple diblock copolymers for example, the grafting densities of both brushes have to be identical. To achieve this in complex morphologies the polymer trajectories have to be chosen accordingly. A study discussing these conditions and their application to polymeric systems is given in [42]. These effects and the boundary conditions given by additional interfaces enclosing the respective domain may lead to polymer trajectories which are not perpendicular to the interface and could even by curved. Since a quantitative evaluation of these effects is far from trivial for most complex morphologies, we refrain from accurately determining the polymer trajectories and rather use the simple conception of straight and perpendicular trajectories in (2.78), meaning that $z(\vec{r})$ denotes the distance from position $\vec{r}$ to the closest point on the grafting surface. In combination with the interfacial free energies mediated by the interfacial tensions (2.66) this facilitates an understanding for the formation ordered morphologies and how certain copolymer architectures can stabilize novel mesophases.
Moreover, a quantitative study overcoming these complications and relaxing the assumptions of the SST can be achieved by evaluating the full self-consistent field equations presented in the last section. This allows to verify the concepts developed by employing the SST equations and to calculate the stability of different structures more accurately. A numerical approach to solve the full self-consistent equations is presented in the next section.

2.3 Spectral method for solving the self-consistent equations

Although there are approaches to solve the SCFT equations numerically in real space [12, 83, 78, 79, 76, 41], we implement the spectral method [53] for this task. This allows us to calculate the free energies of periodic ordered microstructures. Since we know certain candidate morphologies we would like to compare, the spectral method allows for an efficient computation of all relevant quantities. This is vital because due to the complexity of some of our structures other more computationally demanding (real space) approaches are not feasible yet. Moreover, the boundary conditions for the three dimensional structures have to be chosen in either case such that methods which are trying to find the minimum free energy solution of the copolymer melt without a priori knowledge of it can be strongly influenced by

the assumed boundaries and might be trapped in metastable morphologies for example. Our approach in looking for new structures is hence given by applying the analytical formulas presented in the last section to understand what properties are important for an equilibrium structure and how these are influenced by the molecular architecture. With that, we identify possible candidate structures which can then be tested numerically to find the most suitable candidate for the equilibrium structure.
The spectral method starts with expanding all spatial functions, for example $\phi_I(\vec{r})$, as

$$\phi_I(\vec{r}) = \sum_i = \phi_{I,i} f_i(\vec{r}), \tag{2.79}$$

where $f_i(\vec{r})$, $i = 0, 1, 2, ...$ are orthonormal basis functions,

$$\frac{1}{V} \int d^3r \; f_i(\vec{r}) f_j(\vec{r}) = \delta_{ij}. \tag{2.80}$$

Furthermore, these basis functions posses the symmetry of the structure being considered and are chosen to be eigenfunction of the Laplacian operator,

$$\nabla^2 f_i(\vec{r}) = -\frac{\lambda_i}{\xi^2} f_i(\vec{r}), \tag{2.81}$$

where ξ is the length scale of the morphology which has to be determined during the minimization. Starting with $f_0(\vec{r}) \equiv 1$ we order the functions such that λ_i is a nondecreasing series. The unnormalized basis functions be found in [29] or can be constructed from symmetry considerations, cf. appendix B. Moreover, we define

$$\Gamma_{ijk} \equiv \frac{1}{V} \int d^3r \; f_i(\vec{r}) f_j(\vec{r}) f_k(\vec{r}). \tag{2.82}$$

Note that the λ_i and the Γ_{ijk} have to be calculated just once for each structure. We expand the partial partition functions similarly to (2.79),

$$q_{I,\iota}(\vec{r}, s) = \sum_i q_{I,\iota,i}(s) f_i(\vec{r}). \tag{2.83}$$

With this the diffusion equation, e.g. (2.30), reads

$$\frac{dq_{I,\iota,i}(s)}{ds} = \sum_j A_{I,ij} \, q_{I,\iota,j}(s), \tag{2.84}$$

where we have introduced the matrices

$$A_{I,ij} \equiv -\frac{a_I^2 N}{6} \frac{\lambda_i}{D^2} \delta_{ij} - \sum_k w_{I,k} \Gamma_{ijk}. \tag{2.85}$$

The initial condition for a free end is simply $q_{I,\iota,i}(0) = \delta_{i0}$ and the solution to (2.84) is given by

$$q_{I,\iota,i}(s) = \sum_j T_{I,ij}(s) \, q_{I,\iota,j}(0), \tag{2.86}$$

where

$$T_{I,ij}(s) \equiv \exp\left(A_I s\right)_{ij} \tag{2.87}$$

are the matrix exponentials of the respective matrices $A_{I,ij}$.
We evaluate this by performing a matrix diagonalization of the matrices $A_{I,ij}$,

$$A_{I,ij} = \sum_{km} U_{I,ik} D_{I,km} U^{-1}_{I,mj}. \tag{2.88}$$

The diagonal matrices $D_{I,ij}$ store the eigenvalues which we label by $d_{I,i} \equiv D_{I,ii}$. The respective columns of the matrices $U_{I,ij}$ are the corresponding normalized eigenvectors. Since the matrices $A_{I,ij}$ are symmetric, their eigenvalues $d_{I,i}$ will be real and the matrices $U_{I,ij}$ will be orthogonal, $U^{-1}_{I,ij} = U_{I,ji}$. With this we can write $A_{I,ij}$ as

$$A_{I,ij} = \sum_{k} d_{I,k} U_{I,ik} U_{I,jk} \tag{2.89}$$

and the exponential matrices as

$$T_{I,ij}(s) = \sum_{k} \exp\left(s d_{I,k}\right) U_{I,ik} U_{I,jk}. \tag{2.90}$$

This shows us how to calculate these matrices for given values of I and s, which can be used in the following equations, such as in (2.92).

In the same way as in (2.86) we obtain the solution for the other partial partition function,

$$q^{\dagger}_{I,\iota,i}(s) = \sum_{j} T_{I,ij}(f_{I,\iota} - s)\, q^{\dagger}_{I,\iota,j}(f_{I,\iota}). \tag{2.91}$$

In order to obtain the initial conditions for the polymer ends linked to other chains within the copolymer we translate the previously discussed $s \to 0$ limits of (2.35) and (2.36) to reciprocal space. The simple connection between two chain, in real space denoted $q_{I_1,\iota_1}(\vec{r},0) = q_{I_2,\iota_2}(\vec{r}, f_{I_2,\iota_2})$ for example, simply translates to $q_{I_1,\iota_1,i}(0) = q_{I_2,\iota_2,i}(f_{I_2,\iota_2}) \;\; \forall i$. The connection between three distinct chains $q_{I_1,\iota_1}(\vec{r},0) = q_{I_2,\iota_2}(\vec{r}, f_{I_2,\iota_2}) q_{I_3,\iota_3}(\vec{r}, f_{I_3,\iota_3})$ translates to $q_{I_1,\iota_1,i}(0) = \sum_{jk} \Gamma_{ijk} q_{I_2,\iota_2,j}(f_{I_2,\iota_2}) q_{I_3,\iota_3,k}(f_{I_3,\iota_3}) \;\; \forall i$.
Having calculated the partial partition functions, we are able to determine the single chain partition function and the segment concentrations. From (2.37) we get the expression for the single chain partition function in reciprocal space,

$$Q\left[\{w_I\}_{I\in\mathbb{I}}\right] = V \sum_{i} q_{I,\iota,i}(s) q^{\dagger}_{I,\iota,i}(s), \tag{2.92}$$

where the choice of the connection point between the partial partition functions, determined by I, ι and s, is arbitrary. To calculate the segment concentrations we follow (2.39) in reciprocal space,

$$\phi_{I,i} = \frac{V}{Q} \sum_{jk} \Gamma_{ijk} I_{I,jk}, \tag{2.93}$$

where we have introduced the matrices

$$I_{I,jk} \equiv \sum_{\iota=1}^{I^{max}} \int_0^{f_{I,\iota}} ds\; q_{I,\iota,j}(s) q^{\dagger}_{I,\iota,k}(s). \tag{2.94}$$

With the introduction of the eigenvalues $d_{I,i}$ and the orthogonal matrices $U_{I,ij}$ storing the respective eigenvectors, we can use the expressions (2.86), (2.91) and (2.90) to perform the

integration in (2.94),

$$I_{I,jk} = \sum_{\iota=1}^{I^{max}} \sum_{mn} \left[\frac{\exp\left(f_{I,\iota} d_{I,m}\right) - \exp\left(f_{I,\iota} d_{I,n}\right)}{d_{I,m} - d_{I,n}} \right] U_{I,jm} U_{I,kn} \bar{q}_{I,\iota,m}(0) \bar{q}^{\dagger}_{I,\iota,n}(f_{I,\iota}), \qquad (2.95)$$

where we have defined $\bar{q}_{I,\iota,i}(0) \equiv \sum_j q_{I,\iota,j}(0) U_{I,ji}$ and $\bar{q}^{\dagger}_{I,\iota,i}(f_{I,\iota}) \equiv \sum_j q^{\dagger}_{I,\iota,j}(f_{I,\iota}) U_{I,ji}$. Note that for equal eigenvalues $d_{I,m} = d_{I,n}$ the factor in square brackets in (2.95) reduces to $f_{I,\iota} \exp\left(f_{I,\iota} d_{I,m}\right)$.
The calculation of the other self-consistent equations in reciprocal space is straightforward. The incompressibility constraint (2.21) simply reads

$$\sum_{I \in \mathbb{I}} \phi_{I,i} = \delta_{i0}. \qquad (2.96)$$

for all values of i, and the self-consistent condition for the potential fields (2.22) can be written as

$$w_{I,i} = \sum_{J \neq I} \chi_{IJ} N \ \phi_{J,i} + \kappa_i. \qquad (2.97)$$

Let us now discuss the solution of the self-consistent equations (2.93, 2.96, 2.97) in detail. Having chosen the symmetry of our target structure, we are able to calculate the λ_i and the Γ_{ijk} values. Additionally, we require an initial guess for the fields which is ideally as close as possible to the actual solution. This can be achieved by constructing a geometric model (in real space) which then provides the segment concentrations $\phi_I(\vec{r})$. Usually, we have a discretized unit cell in real space and divide it into three distinct and perfectly segregated domains such that the resulting structure obeys the chosen symmetries. The segment concentrations $\phi_I(\vec{r})$ can then be translated to reciprocal space in a straight forward fashion yielding the components of this field,

$$\phi_{I,i} = \frac{1}{V} \int d^3r \ \phi_I(\vec{r}) f_i(\vec{r}). \qquad (2.98)$$

Since we are only able to treat a finite number of these components, we have to introduce a cut-off which is given by the number of basis functions we employ, $\#BF$, such that $0 \leq i < \#BF$. At this point it is possible to introduce changes to the initial segment concentration fields, e.g. by introducing random fluctuations or by damping higher-order terms. Note, however, that the $i = 0$ components of the segment concentrations are fixed by their assumed average values, $\phi_{I,0} = \langle \phi_I(\vec{r}) \rangle$. By also arbitrarily choosing $\kappa_0 = \langle \kappa(\vec{r}) \rangle = 0$, we fix the $\omega_{I,0}$ components by virtue of (2.97). To obtain an initial condition for the fields $\omega_I(\vec{r})$, or rather for its components $\omega_{I,i}$, we can use our initial condition for the segment concentrations in (2.97) and furthermore assume that all components κ_i are zero. We use this initial condition for the $\omega_{I,i}$ to enter the first iteration for the calculation of the self-consistent fields, which will be described in the following.

The self-consistent equations are solved through a number of iterations, each starting by looking at the fields of the potentials described by their fourier components $\omega_{I,i}$. We use these values to calculate the matrices $A_{I,ij}$, which have been defined in (2.85). Those matrices can then be used to calculate the single chain partition function Q, see (2.92), and the segment concentrations $\phi_{I,i}$, see (2.93). The detailed calculations involved in this task have been outlined above. We note that the main computational costs of each iteration occur during these calculations. More specifically, there are two operations limiting the

performance of the algorithm. First of all, we have to perform a matrix diagonalization[1] of the matrices $A_{I,ij}$ as described in (2.89). Secondly, we have to perform a couple of matrix multiplications[2] to calculate the segment concentrations $\phi_{I,i}$, cf. (2.95). Both operations render the computational cost of each iteration to be of the order $\mathcal{O}((\#BF)^3)$.
Operations involving the Γ_{ijk}, see e.g. (2.85) or (2.93), may seem costly but can be computed efficiently by utilizing the fact that most elements Γ_{ijk} are equal to zero.
Having calculated the $\phi_{I,i}$, we determine the κ_i components using the assumed values for $\omega_{I,i}$ and equations (2.96) and (2.97). The detailed calculations differ for the individual copolymer architectures and the resulting expressions are provided in appendix C. Finally, we are able to put in the values we just obtained for $\phi_{I,i}$ and κ_i in (2.97) to calculate new values for the potential fields which we label $\bar{\omega}_{I,i}$. If the $\bar{\omega}_{I,i}$ coincide with the values $\omega_{I,i}$ used to perform the calculations of all fields they are called self-consistent and we have found the solution to our problem. Otherwise, we need a way to choose other fields $\omega_{I,i}$ which come closer in achieving this self-consistency. Since we essentially need to find fields such that $\bar{\omega}_{I,i} - \omega_{I,i} = 0 \ \ \forall i$, we have to employ a root finding algorithm. Several methods[3] can be used for this, but we present only one which turns out to work quite well for our task. Namely, we employ the Anderson mixing scheme [1] for the spectral approach to solve the self-consistent equations as demonstrated in [49]. For this method, we need to store the $\omega_{I,i}$ and the evaluated $\bar{\omega}_{I,i}$ in a history, since we will need the values of the last few iterations to find the $\omega_{I,i}$ components for the next iteration. Hence, we introduce the index (k) to label the number of the respective iteration. The values of the potential fields used and derived in the kth iteration are from now on labeled $\omega_{I,i}^{(k)}$ and $\bar{\omega}_{I,i}^{(k)}$, respectively.
Aside from the implementation demonstrated in [49], the Anderson mixing scheme has been employed for the solution of the self-consistent field equations before, however, mainly following the real space approach, see e.g. [79]. Furthermore, the implementation for the spectral approach presented in [49] benefits from a generalization for the mixing parameter [16].
Here we show the main steps for implementing the Anderson mixing scheme to solve of the spectral self-consistent equations. First of all, we compute the differences

$$d_{I,i}^{(k)} = \bar{\omega}_{I,i}^{(k)} - \omega_{I,i}^{(k)} \tag{2.99}$$

for all values of (k) stored in our history. We use these to define a measure

$$\text{error} \equiv \sqrt{\frac{\sum_{I,i} \left(d_{I,i}^{(k)}\right)^2}{\sum_{I,i} \left(\omega_{I,i}^{(k)}\right)^2}} \tag{2.100}$$

which quantifies the error, or in other words the numerical inacurracy, in the self-consistent equations (2.97). If the error (2.100) lies below a certain threshold[4] we consider the self-consistent equations as being solved and we are able to use the obtained fields to calculate

[1] The simple implementation uses a matrix diagonalization scheme called *Symmeig* taken from numerical recipes [66], whereas the implementation for the cluster uses the *dsyev* routine of LAPACK provided by the Intel®Math Kernel Library.

[2] In the simple implementation these matrix multiplications are hard-coded. For the cluster implementation we use the *cblas_dgemm* routine of BLAS provided by the Intel®Math Kernel Library.

[3] Our earlier implementations employed Broyden's method as described by numerical recipes [66]. However, this method requires the calculation of the derivatives of $\bar{\omega}_{I,i} - \omega_{I,i}$ with respect to the components $\omega_{I,i}$. Since the $\bar{\omega}_{I,i}$ depend highly non-linearly on these, the derivatives have to be approximated by finite differences resulting in a large number of extensive calculations needed, especially when using a large number of basis functions.

[4] Typically, we used values between 10^{-4} and 10^{-5}.

the free energy of the structure. If not, we have to find improved estimates for the components $\omega_{I,i}^{(k+1)}$ in the next iteration based on the values of a number, say n_r, of the previous iterations. For this purpose we define a symmetric matrix

$$W_{mn} \equiv \sum_{I,i} \left(d_{I,i}^{(k)} - d_{I,i}^{(k-m)}\right)^2 \left(d_{I,i}^{(k)} - d_{I,i}^{(k-n)}\right)^2 \tag{2.101}$$

and a vector

$$V_m \equiv \sum_{I,i} \left(d_{I,i}^{(k)} - d_{I,i}^{(k-m)}\right)^2 d_{I,i}^{(k)} \tag{2.102}$$

for $m, n = 1, ..., n_r$. We use these to calculate the coefficients

$$C_n \equiv \sum_{m=1}^{n_r} (W^{-1})_{nm} V_m, \tag{2.103}$$

which allow to combine the previous iterations by defining

$$\Omega_{I,i}^{(k)} = \omega_{I,i}^{(k)} + \sum_{n=1}^{n_r} C_n \left(\omega_{I,i}^{(k-n)} - \omega_{I,i}^{(k)}\right), \tag{2.104}$$

$$D_{I,i}^{(k)} = d_{I,i}^{(k)} + \sum_{n=1}^{n_r} C_n \left(d_{I,i}^{(k-n)} - d_{I,i}^{(k)}\right). \tag{2.105}$$

The fields for the next iteration are then given by

$$\omega_{I,i}^{(k+1)} = \Omega_{I,i}^{(k)} + \lambda D_{I,i}^{(k)}, \tag{2.106}$$

where $0 < \lambda \leq 1$ is an arbitrary mixing parameter. The usual Anderson mixing uses $\lambda = 1$, but using this value leads to problems when there are not enough previous iterations available to build up a good estimate for the next iteration. Therefore, in order to overcome this problem which necessarily arises in the first few iteration steps, we gradually increase the mixing parameter, $\lambda = 1.0 - 0.9^k$. For the mixing itself, we combine the values of all the available previous iterations up to the N_r most recent[5], hence $n_r = \min\{k-1, N_r\}$. In conclusion, we employ the Anderson mixing scheme to calculate the fields for the next iteration but allow for an increasing mixing parameter λ to overcome problems in the first few iterations.

After we have determined the correct self-consistent fields, we can use these to calculate the mean-field free energy. According to (2.26), in reciprocal space this free energy reads

$$\frac{F\left[\{\phi_I\}_{I\in\mathbb{I}}, \{w_I\}_{I\in\mathbb{I}}, \kappa\right]}{nk_BT} = -\ln\left(\frac{Q}{V}\right) - \frac{1}{2}\sum_{J\neq K\in\mathbb{I}} \chi_{JK} N \sum_i \phi_{J,i}\phi_{K,i}. \tag{2.107}$$

The last remaining step is to adjust the size of the unit cell[6], denoted ξ, so as to minimize the free energy (2.107). Since the mean-field free energy is an extremum with respect to the self-consistent fields, it is sufficient to require

$$\frac{\partial}{\partial\xi} \ln\left(\frac{Q}{V}\right) = 0 \tag{2.108}$$

[5] Usually, one chooses $N_r \approx 30$.

[6] The size of the unit cell ξ (or equivalently the periodicity of the structure) is usually measured in units of the radius of gyration, in our notation defined as $\sqrt{\frac{Na^2}{6}}$.

for minimizing the free energy with respect to the unit cell size [49]. The partial derivative in (2.108) can be approximated by finite differences. If we treat complex structures with additional degrees of freedom (e.g. the $\frac{c}{a}$ ratio or angles of the unit cell), we can use the same method to minimize the free energy with respect to these parameters. For this we just have to replace the differentiation with respect to ξ in (2.108) by a differentiation with respect to the particular parameter. We do not perform these minimizations within out actual SCFT program, but rather use the prescribed spectral method to calculate the free energy (2.107) for a given set of parameters and then use external scripts to adjust these parameters such that the obtained free energies approach a minimum.

In this section, we have presented the spectral method to numerically solve the self-consistent equations. This allows us to calculate different properties, and especially the mean-field free energies, of different candidate morphologies for a given copolymeric system. By minimizing the free energy of a given structure with respect to its internal degrees of freedom for a given set of structure-independent parameters which define the architecture of the copolymer, we are able to identify the equilibrium structure as the structure with the lowest (minimum) free energy. If we identify the equilibrium structure for the whole range of adjustable architectural parameters we can construct a phase diagram. This diagram shows the stability of a number of suitable candidate structures in dependence of the properties of the copolymers.
As has been mentioned in the beginning of this section, there are also different real space implementations to solve the self-consistent equations which in principle would allow to calculate the equilibrium structures without a priori knowledge of the respective morphologies [12, 83, 76, 41]. While these approaches reach their limitations when applied to the computationally demanding mesophases of interest in this thesis, they could, however, provide an approach to look for new structures and to confirm the calculations of the spectral method. Moreover, other numerical methods, for example molecular dynamic simulations, can be implemented to see if the proposed structures form for the assumed parameter values. Different methods to examine structure formation could therefore provide a valuable extension to the analysis performed in this thesis.

In the next chapters we demonstrate the application of the methods developed throughout this chapter to understand the self-assembly process for certain copolymer architectures of interest. We also present phase diagrams, which have been constructed using the spectral approach, in order to show the stability of different structures in dependence of the detailed molecular parameters.

Chapter 3

Self-assembly of diblock copolymers

The simplest example of block copolymers are diblock copolymers, which are made by covalently linking two immiscible polymer chains at one of their ends, cf. figure 1.1(a). For this reason, these systems have been the focus of many studies and melts of diblock copolymers constitute the primary example for a successful application of the SCFT [47, 19, 13, 22, 48]. This chapter reviews the mesophases found in self-assembled diblock copolymer melts and shows how the SCFT is utilized to examine them, before we introduce novel concepts for more complex architectures in the following chapters. For a good introduction to the topics of this chapter we refer to [47]. We devote special attention to bi- and tri-continuous structures, characterized by two or three intertwined labyrinths, respectively, which have been found in these systems .

Section 3.1 demonstrates the phase diagram for diblock copolymer melts, as calculated by the spectral method, and compares it with the experiment. Furthermore, we discuss the structures formed in these systems and briefly mention the theoretical methods which have been developed in order to explain this phase diagram.

To understand the essential driving mechanisms for diblock copolymer self-assembly, we employ the SST in section 3.2. In the limit of strong segregation, the interfaces between the two polymeric species become narrow and the morphologies are described by the shape of these surfaces. As will be shown, the SST affords an explanation for the increasing curvature of these interfaces upon increasing the imbalance between the volume fractions of the polymer chains. Besides the need to adopt a certain preferred curvature, another concept, referred to as packing frustration, is introduced which determines the global embedding of the interfaces.

The most complex phase found for diblock copolymers in the melt state is the so-called bicontinuous Gyroid structure. We discuss this structure in detail in section 3.3 and explain the reasons for its existence. Additionally, we mention other bicontinuous structures relevant for diblock copolymer self-assembly. Bicontinuous structures are characterized by two intertwined network-like labyrinths, which are in the case of diblock copolymers formed by the minority species and separated by a matrix of the majority component.

Due to the existence of bicontinuous structures in self-assembled systems, this thesis addresses the obvious question of whether the formation of tricontinuous structures, i.e. structures characterized by three interwoven labyrinths, is also feasible. Section 3.4 presents a tricontinuous structure observed in systems related to diblock copolymer self-assembly and reflects about the reasons for its formation. This way, we cover the tricontinuous structures observed so far experimentally, before directing our attention to the possibility of finding novel tricontinuous structures in other polymeric systems in the next chapters.

3.1 Phase diagram for diblock copolymer melts

Diblock copolymers provide one of the most well-examined systems to study self-assembly and structure formation. Astonishingly, different soft-matters systems with the potential for structure formation exhibit the same structures as found for diblock copolymers. One of the most prominent examples, besides block copolymers, are assemblies of surfactant molecules or lipids. Commonly, these molecules consist of a hydrophobic chain (or *tail*) attached to a hydrophilic head group. Head and tail of these molecules are hence immiscible and solutions of these molecules show morphologies similar to those found in diblock copolymer systems [73]. This shows a certain universality of the mechanism behind this self-assembly irrespective of the precise chemical realization of the system.

The typical starting point for theoretical investigations of diblock copolymers is the melt state, where we have a pure system of these macromolecules without any additional components. For simplicity, we demonstrate the case where both polymer species have the same statistical segment length. As will be shown more profoundly in the next section, this essentially leaves us with two parameters describing our system of AB diblock copolymers. Henceforth, A and B denote the two chemical species involved. The first of these parameters is the volume fraction of one species, say A, which is labeled f. A low value of f describes a system where the polymer chains of species A are much shorter than the B chains to which they are linked. For $f = 0.5$ we end up with the balanced case where both chains have equal length. The second parameter that is important for our system, χN, is the product of the (microscopic) interaction parameter χ, which has been introduced in (2.6), and the total number of segments of each copolymer, N. As it turn out, χN is the appropriate measure for the segregation strength of our system. For $f \approx 0.5$ and χN above a certain threshold, we expect a spatial segregation of both species into a structures with equal domains for both species. Indeed, the AB diblock copolymers self-assemble into a lamellar mesophase, depicted in figure 3.1. For different values of f this morphology changes and one also observer structures, where the domains occupied by species A and B are different in shape. Figure 3.2 demonstrates the theoretical phase diagram for AB diblock copolymers, evaluated by the SCFT methods, and the mesophases it comprises. Besides the lamellar structure at $f \approx 0.5$, one observes morphologies where the minority component forms a hexagonal arrangement of cylinders (Hex), a body-centered cubic (BCC) or a close-packed (CP) arrangement of spheres, or two intertwined labyrinths, corresponding to the Gyroid (Gyr) structure. Note that more recent studies also identified a single-network structure, called the Fddd (O^{70}) morphology, at weak segregations [82, 77]. However, if χN is too low, no structures forms and the polymer chains just form a homogeneous, disorder phase (Dis). This theoretically determined phase diagram is in good agreement with experiments. Figure 3.3 shows the experimentally obtained phase diagram for diblock copolymers. There are some deviations from the theoretical phase diagram in figure 3.2. The differences along the disorder-order transition are due to fluctuation effects which become important in this

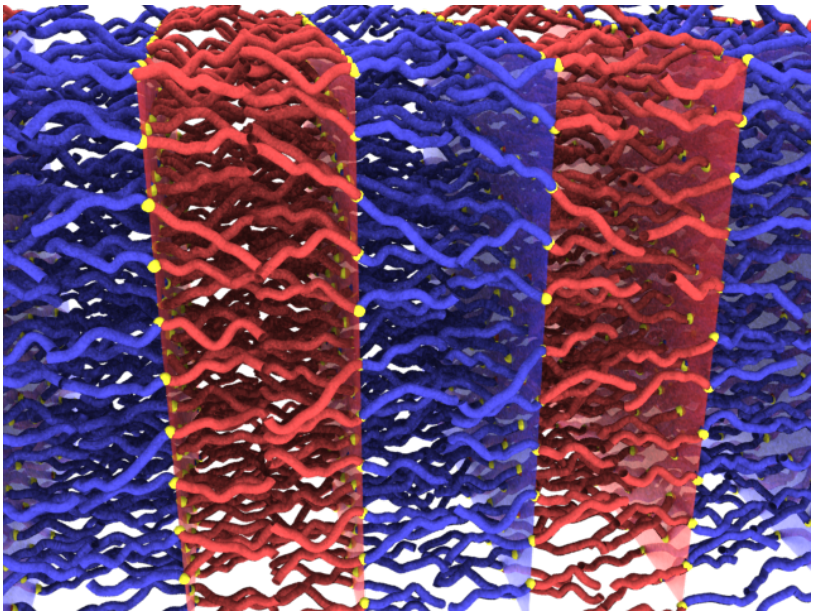

Figure 3.1: Artistic representation of a lamellar morphology, found in balanced ($f = 0.5$) diblock copolymer melts at sufficient segregation.

region [20]. The asymmetry around $f = \frac{1}{2}$ in the experimental phase diagram can be partly accounted for by different statistical segment lengths for species A and B [52]. Furthermore, one will not only observe the equilibrium minimum free energy mesophases in experiments, but rather metastable solutions because the polymer dynamics may get trapped in one of these configuration. An example is the hexagonally perforated lamellar (HPL) phase which is present in the experimental phase diagram and can be described by perforating the sheets of the minority component in a hexagonal arrangement of holes such that the sheets of the majority component are connected via these perforations.

The theoretical treatment of inhomogeneous polymeric systems by mean-field theory was developed in [28, 26]. It was applied to interfaces between immiscible polymer chains and already considered interfaces in diblock copolymers as a particular example. However, this study did not discuss the existence of different morphologies but rather studied the physics of segregation while having the lamellar structure in mind. A study considering the weak segregation limit and focusing on the onset of microphase separation was presented in [40]. It was able to explain the formation of different morphologies observed for sufficiently large values of χN. The structure examined are sometimes referred to as the classical phases of diblock copolymer melts and comprise the lamellar, (hexagonal) cylindrical and (body-centered cubic) spherical mesophases. With the introduction of the SST in [74], it became possible to understand the existence of these classical phases for well-segregated melts, providing further insight into the mechanism of their self-assembly. The spectral method [53] for solving the SCFT made it possible to construct the phase diagram for intermediate segregation thereby bridging the gap between the two analytical limits of weak and strong segregation [51]. Additionally, it was possible to identify the bicontinuous Gyroid

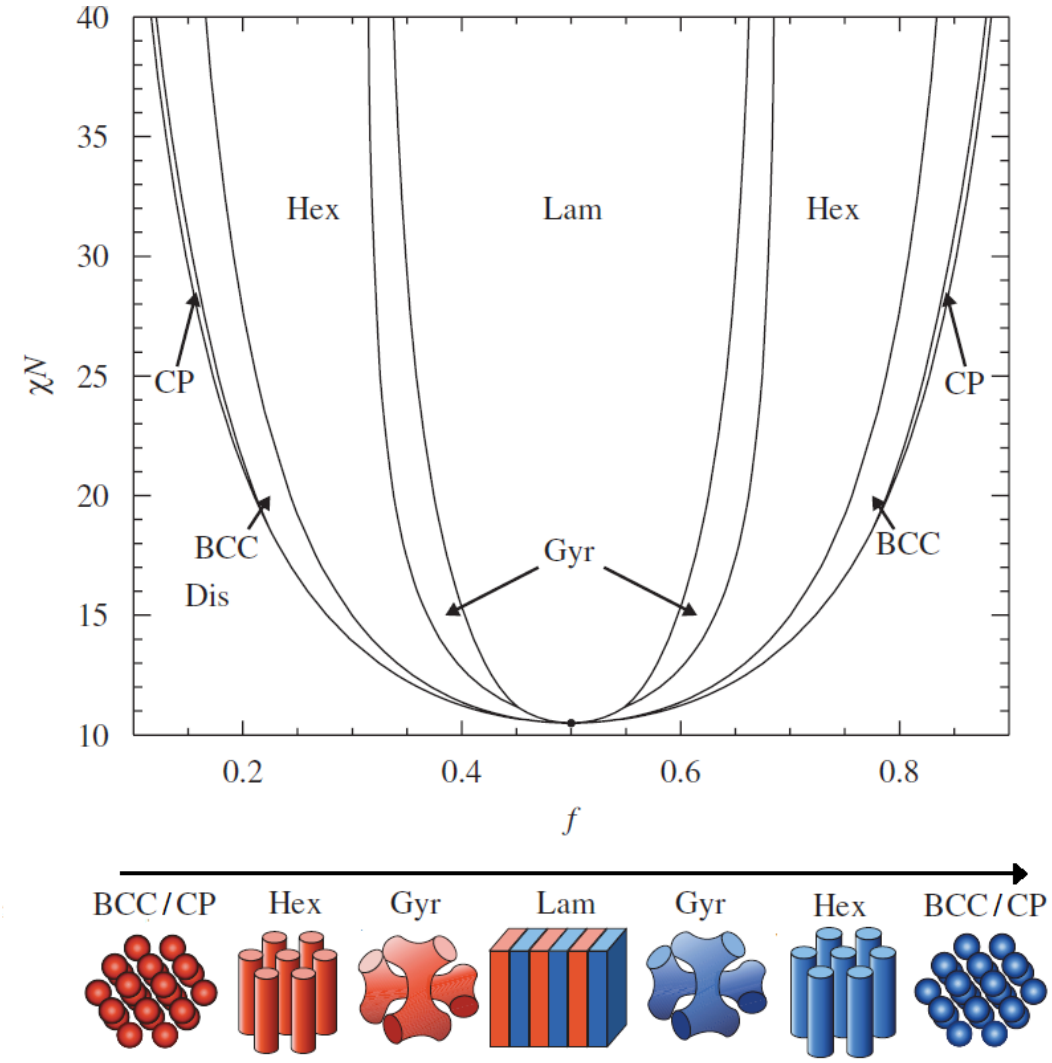

Figure 3.2: SCFT phase diagram for diblock copolymer melts with equal statistical segment lengths for both polymer species. The diagram shows the stability regions of different ordered structures in dependence of the two characteristic system parameters. These are the volume fraction of the species A (shown in red), f, and the segregation strength between both species, χN. The morphologies are, ordered by increasing molecular asymmetry, a lamellar phase (Lam), a bicontinuous Gyroid morphology (Gyr), a hexagonal arrangement of cylinders (Hex), and a body-centered cubic (BCC) or close packed (CP) arrangement of spheres. These mesophases are schematically depicted below the phase diagram. The volumes occupied by polymer chains of species A are shown in red, whereas the volumes shown in blue are filled by species B. For clarity, the polymeric majority component is not shown. The phase diagram and the pictures of the mesophases involved have been taken from [22]. Note that more recent phase diagram also identify an additional single-network structure at lower segregation [82, 77].

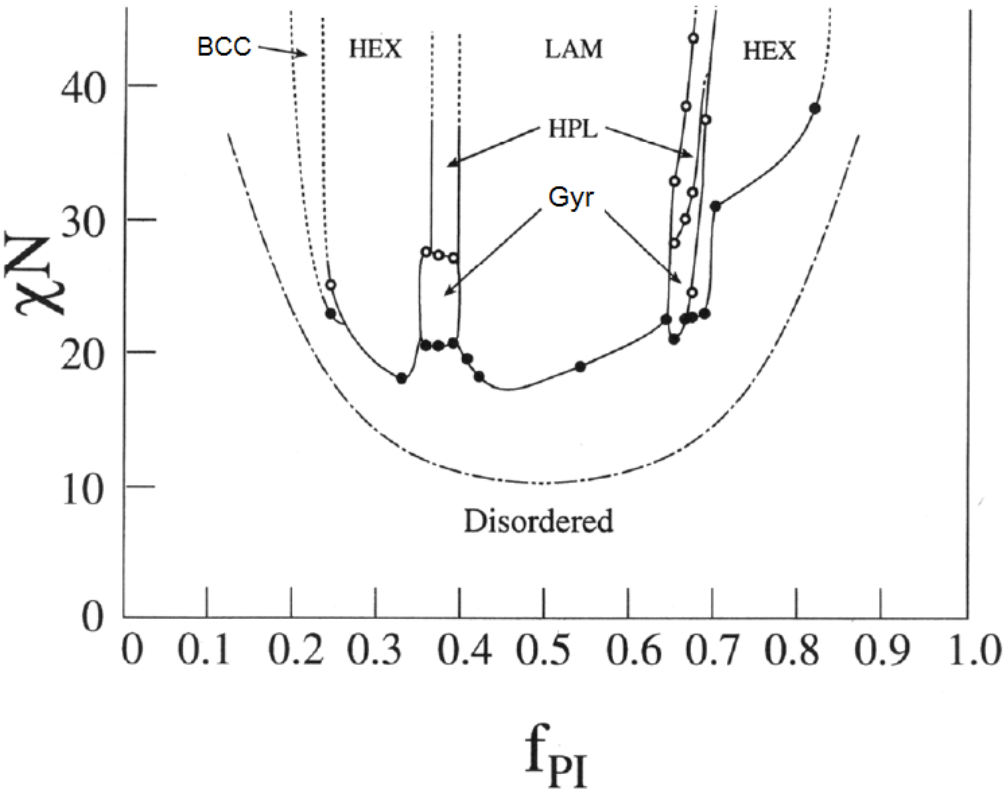

Figure 3.3: Experimental phase diagrams for polyisoprene-polystyrene diblock copolymers, where f_{PI} denotes the volume fraction of polyisoprene. Dots denote the experimental data points for transitions between different phases, while the solid curves delineate the stability regions of the different phases observed but might not correspond to precise phase boundaries. The phase diagram has been taken from [38].

as a stable phase for intermediate segregations[1].
Our study of triblock star-copolymers benefits from these concepts, originally developed to understand systems of diblock copolymers.

3.2 The role of curvature and packing frustration

To understand the reasons for the formation of the structure emerging in diblock copolymer melts, we employ the analytical formulas developed in section 2.2. These allows us to identify a geometric concept these structures are striving for and in fact shows that nature chooses the best suited morphology to fulfill certain geometric requirements. Specifically for diblock copolymers, the structures will, depending on the volume fractions of the two components, adopt interfaces with a preferred curvature with the additional constraint that these interfaces have to be embedded, in a certain sense, in a homogeneous fashion. The demonstration of the fruitfulness of these ideas motivates us to use the same concepts to develop new geometric design principles for other copolymeric systems, such as those that will be presented in the following chapters.

Let us consider the SST for diblock copolymers in detail. From equations (2.66) and (2.78) we get the free energy contributions due to the interfacial tension and the stretching of the polymer chains, respectively. Note that we have one type of interfacial tension, defined by the contacts between species A and B, and two kinds of stretching contributions, one from brushes of species A and the other from brushes of type B. By putting all contributions together according to (2.23), we end up with the SST expression for the free energy per molecule,

$$\frac{F}{nk_BT} = Na\sqrt{\frac{\chi_{AB}}{6}}\frac{A_{AB}}{V} + \frac{3\pi^2}{8Na^2V}\left[\frac{1}{f^2}\int_{V_A} d^3r\ z^2 + \frac{1}{(1-f)^2}\int_{V_B} d^3r\ z^2\right]. \tag{3.1}$$

Here f denotes the volume fraction of species A, which sets the volume fraction of species B to $1-f$. V_K describes the region occupied by species $K \in \{A, B\}$, A_{AB} is the surface area of the interfaces between both species and V the volume of the system. For the sake of simplicity, we have assumed the same statistical segment length a for both polymer species. Note that it is sufficient to evaluate all geometric measures, A_{AB}, V, $\int_{V_K} d^3r\ z^2$, for a single unit cell of each morphology. However, the physical size of this unit cell, ξ, is not fixed yet. The structure chooses ξ such as to minimize its free energy (3.1). By noting that the interfacial term scales as $1/\xi$, whereas the stretching terms scale as ξ^2, we can perform this minimization, see (D.1) and (D.2), and obtain the minimum (and scaling invariant) free energy,

$$\frac{F}{nk_BT} = (\chi N)^{\frac{1}{3}}\frac{3}{2^{\frac{2}{3}}}\left\{\frac{\pi^2}{16}\frac{A_{AB}^2}{V^3}\left[\frac{1}{f^2}\int_{V_A} d^3r\ z^2 + \frac{1}{(1-f)^2}\int_{V_B} d^3r\ z^2\right]\right\}^{\frac{1}{3}}. \tag{3.2}$$

The equilibrium morphology will be the one which minimizes (3.2). Since the prefactors in (3.2) do not depend on the structure, it is sufficient to consider

$$\frac{F}{nk_BT} \propto \frac{\tilde{F}}{nk_BT} \equiv \left\{\frac{A_{AB}^2}{V^3}\left[\frac{1}{f^2}\int_{V_A} d^3r\ z^2 + \frac{1}{(1-f)^2}\int_{V_B} d^3r\ z^2\right]\right\}^{\frac{1}{3}}. \tag{3.3}$$

[1] Note that the Gyroid morphology is not stable within the SST framework.

in order to find the equilibrium mesophase.

Using this expression and probing the geometries of the classical phases allows to calculate the volume fractions f for the phase transitions between them [74]. While there have been studies demonstrating the geometric concepts behind the observed phase sequence [60], we want to show a more rigorous derivation to elucidate the need for a structure to adopt a certain preferred curvature. We therefore refrain from reviewing previous work and present a simple argument based on the SST expression of the free energy (3.3).

Let us consider a surface element, which is representative for the interfaces of a given structure, i.e. a patch of a cylinder in the hexagonally arranged cylinder mesophase. Note that in diblock copolymers all interfaces between distinct species are also the grafting surfaces for the respective brushes. Let this surface fragment have constant values for its mean and Gaussian curvature at every point, denoted H_0 and K_0, respectively. Both values can, however, be arbitrarily chosen. Let us further w.l.o.g. assume that the orientation of the surface is such that $H_0 \geq 0$. Let us now consider parallel surfaces to this one. A parallel surface is simply obtained by moving each point of the original surface a distance, say $r > 0$, along its (point-)normal. We assume that the original and all parallel surfaces constructed from it will be regular. If A_0 is the surface area of the original surface, the surface area of the parallel surface will be given by [11]

$$A(r) = A_0 \left[1 \pm 2H_0 r + K_0 r^2\right]. \tag{3.4}$$

Note that according to our choice for H_0, the $+$ sign corresponds to parallel surfaces with larger surface areas, which are therefore located at the *outer* side of the original surface, while the $-$ sign yields surfaces with lower areas to the *inner* side. We identify the region spanned by parallel surfaces to the inner side of the original surface with distance $0 \leq r \leq r_{In}$ as the volume occupied by the polymer brush of the minority component and the region spanned by parallel surfaces on the outer side with $0 \leq r \leq r_{Out}$ as the volume occupied by the majority species. These volumes are then given by

$$V(r) = \int_0^r dr' A(r') = A_0 \left[r \pm H_0 r^2 + \frac{K_0}{3} r^3\right], \tag{3.5}$$

where we choose the $+$ sign for the volume of the majority species, V_{Out}, and the $-$ sign for the volume of the minority component, V_{In}. For a given volume fraction of the minority species, f, we have a correlation between these volumes,

$$\frac{V_{Out}}{V_{In}} = \frac{\left[r_{Out} + H_0 r_{Out}^2 + \frac{K_0}{3} r_{Out}^3\right]}{\left[r_{In} - H_0 r_{In}^2 + \frac{K_0}{3} r_{In}^3\right]} \stackrel{!}{=} \frac{1-f}{f}. \tag{3.6}$$

Let us introduce the main curvature radii of the surface, r_1 and r_2, which are reciprocal to the principal curvatures κ_1 and κ_2. We choose r_1 to be the smaller of both radii. With the main curvature radii we can express the mean and Gaussian curvature as $H_0 \equiv \frac{1}{2}\left(\frac{1}{r_1} + \frac{1}{r_2}\right)$ and $K_0 \equiv \frac{1}{r_1}\frac{1}{r_2}$, respectively. The maximum distance for r_{In}, which we want to adopt, is given by requesting that $A(r)$ must not be negative. By virtue of (3.4) this leads to $r_{In} = r_1$. Henceforth, we write $H_0 r_1 = \frac{1}{2}\left(1 + \frac{r_1}{r_2}\right)$ and $K_0 (r_1)^2 = \frac{r_1}{r_2}$. Note that by our convention we have $-1 \leq \frac{r_1}{r_2} \leq 1$ and $r_1 \geq 0$. Using $r_{In} = r_1$ and rearranging (3.6) allows us to identify $\frac{r_{Out}}{r_{In}}$ as the smallest (real and positive) solution of the polynomial equation

$$\frac{1}{3}\frac{r_1}{r_2}\left(\frac{r_{Out}}{r_{In}}\right)^3 + \frac{1}{2}\left(1 + \frac{r_1}{r_2}\right)\left(\frac{r_{Out}}{r_{In}}\right)^2 + \frac{r_{Out}}{r_{In}} - \frac{1-f}{f}\left[\frac{1}{2} - \frac{1}{6}\frac{r_1}{r_2}\right] = 0, \tag{3.7}$$

for fixed values of f and r_1/r_2. This works for all curved surfaces but not for the (flat) lamellar structure. Here, we must rather choose $H_0 = 0$ and $K_0 = 0$ and simply get $\frac{r_{Out}}{r_{In}} = \frac{1-f}{f}$.

From (3.3) we can calculate the free energy associated with a structure characterized by interfaces made of the described surface element and grafted polymer brushes associated with the volumes to each side of this surface. At this point of description there are no constraints hindering us from choosing $z(\vec{r})$ to be the shortest distance to the interface. Note that we calculate the stretching of both polymer brushes via (2.78) whereas [74] used another expression for the brush on the outer side of the interface. However, due to other studies [3, 5] we believe that our approach is equally or even better suited, at least for moderate curvatures. This explains the small deviations between our results and those in [74]. It is sufficient to consider the case where species A constitutes the minority component, $0 \leq f \leq \frac{1}{2}$, in (3.3) which yields

$$\frac{\tilde{F}}{nk_BT} = \left\{ \frac{A_0^2}{\left(\frac{1}{f}V_{In}\right)^3} \left[\frac{1}{f^2} \int_{V_{In}} dz\ A_{In}(z) z^2 + \frac{1}{(1-f)^2} \int_{V_{Out}} dz\ A_{Out}(z) z^2 \right] \right\}^{\frac{1}{3}} . \tag{3.8}$$

Inserting the values for the surface areas (3.4) and volumes (3.5) associated with the parallel surfaces and performing the integrals results in

$$\frac{\tilde{F}}{nk_BT} = \left\{ \frac{f}{3} \frac{\left[\frac{1}{4} - \frac{3}{20}\frac{r_1}{r_2}\right]}{\left[\frac{1}{2} - \frac{1}{6}\frac{r_1}{r_2}\right]^3} + \frac{1-f}{3} \frac{\left[1 + \frac{3}{4}\left(1 + \frac{r_1}{r_2}\right)\frac{r_{Out}}{r_{In}} + \frac{3}{5}\frac{r_1}{r_2}\left(\frac{r_{Out}}{r_{In}}\right)^2\right]}{\left[1 + \frac{1}{2}\left(1 + \frac{r_1}{r_2}\right)\frac{r_{Out}}{r_{In}} + \frac{1}{3}\frac{r_1}{r_2}\left(\frac{r_{Out}}{r_{In}}\right)^2\right]^3} \right\}^{\frac{1}{3}} . \tag{3.9}$$

Again, the lamellar mesophase poses an exception because we can not obtain a r_1/r_2 ratio for it and must set $H_0 = K_0 = 0$ instead. In this case expression (3.8) simply results in $\frac{\tilde{F}}{nk_BT} = \left\{\frac{1}{3}\right\}^{\frac{1}{3}}$ independent of the volume fraction f. To obtain the values for the classical phases, we just have to use the respective r_1/r_2 ratio. For spheres this would be $r_1/r_2 = 1$, for cylinders $\frac{r_1}{r_2} = 0$. For a (hypothetical) minimal surface as an interface, we would have $r_1/r_2 = -1$. Generally, negative values for r_1/r_2 indicate negative Gaussian curvatures and hence saddle-shaped surface patches. However, different ratios r_1/r_2 will result in different free energies.

Thus the strategy to obtain the preferred curvature of an interface for a given volume fraction f is as follows. We use f and any r_1/r_2 ratio to obtain $\frac{r_{Out}}{r_{In}}$ via (3.7). Using these values we are able to evaluate the free energy (3.9). By finding the minimum of this free energy with respect to r_1/r_2 for a fixed f, we obtain the preferred curvature, i.e. the optimal r_1/r_2 ratio, or equivalently the preferred ratio of principal curvatures κ_2/κ_1. Figure 3.4 shows this preferred curvature for all relevant volume fractions. However, we have to account for the extra treatment of the lamellar mesophase, which will yield lower free energies than any morphology with curved interfaces for high enough volume fractions. This is indicated by the vertical line in figure 3.4. Therefore, there is only a particular interval of f for which the self-assembly process will prefer curvatures with negative r_1/r_2 ratios. This is for example observed in the (metastable) hexagonally perforated lamellar phase, which is also called catenoid lamellar phase since the perforations in its minority component are described by catenoid-shaped interfaces. More prominently, however, these ratios can be achieved by bicontinuous structures where the interfaces are parallel surfaces to a triply-periodic minimal surface, as will be discussed in the next section. This curvature argument therefore explains

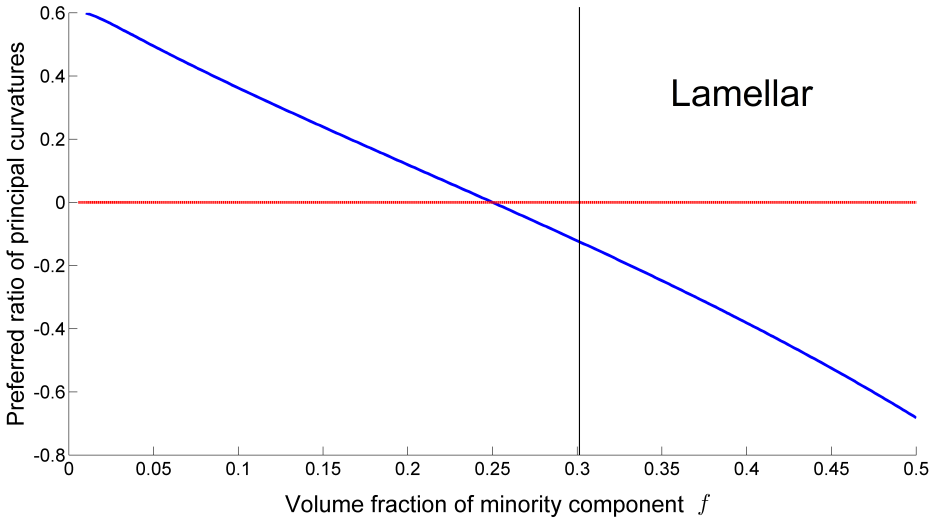

Figure 3.4: Preferred curvature of the interfaces in diblock copolymer melts, as measured by the ratio r_1/r_2, or equivalently the preferred ratio of principal curvatures κ_2/κ_1, as a function of the volume fraction, f, of the the minority component. A horizontal line at $\kappa_2/\kappa_1 = 0$ serves as a guide to the eye. The vertical line shows the volume fraction after which no curvature at all is preferred and where the system adopts a lamellar morphology. For an interval between this line and the value where the preferred ratio becomes zero, the systems prefers surfaces with negative Gaussian curvature.

the sequence of mesophases observed in diblock copolymer melts, and in particular why we find e.g. bicontinuous phases between the lamellar and the cylindrical mesophase.
To compare the free energies of structures with surfaces of the preferred curvature to those corresponding to the classical phases observed in diblock copolymers, we employ (3.9). By inserting the corresponding values for the r_1/r_2 ratios of the classical phases and by accounting for the extra treatment for the flat lamellar phase, we can calculate their free energies and compare them with the free energy of surfaces of preferred curvature. To this end we define

$$\Delta_F \equiv \frac{\left[\tilde{F}_{structure}\right]^3 - \left[\tilde{F}_{preferred}\right]^3}{\left[\tilde{F}_{preferred}\right]^3} \tag{3.10}$$

as the relative difference between the cubic free energies of a given structure to the cubic free energy of a surface with preferred curvature at the same volume fraction f. This difference is plotted in figure 3.5. We see that above a certain volume fraction $f \gtrsim 0.3$ the lamellar mesophase yields a lower free energy than that of the optimally curved surface and is therefore the equilibrium morphology in this regime. On the other side, curved interfaces are preferred for lower volume fractions. In diblock copolymer melts these curvatures are realized by the Gyroid structure, and by the classical structures of certain arrangements of cylinders, which provide the best curvature for $f \approx 0.25$, and spheres, being the morphology of choice for even lower volume fractions. We note that effects of conformational asymmetry in the diblock copolymer architecture can be incorporated into this treatment [60].

So far we have not discussed how these curved or flat interfaces can be embedded in

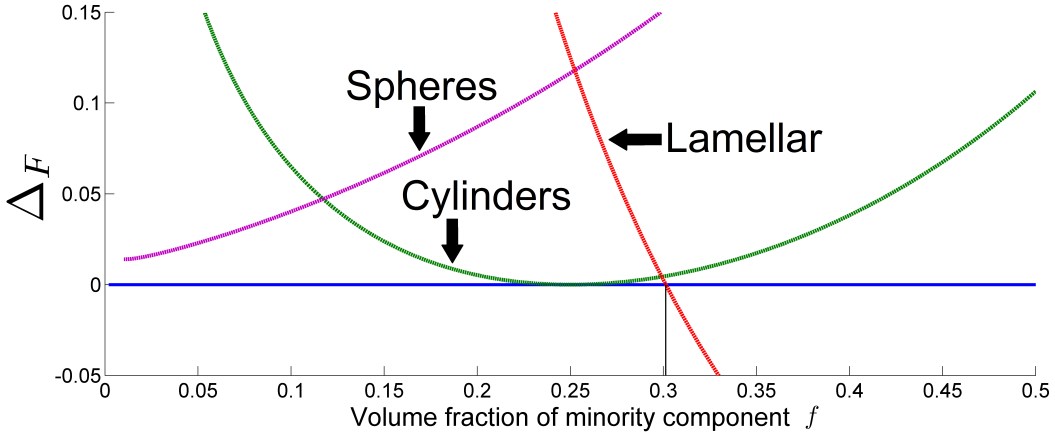

Figure 3.5: SST estimates for the free energies of different structures. We plot Δ_F, as defined in (3.10), for all classical mesophases found in diblock copolymers and for all relevant volume fractions, f, of the minority component. $\Delta_F = 0$, as sketched by the horizontal line, corresponds to the free energy of a (hypothetical) surface adopting the preferred curvature and is hence the minimum free energy for all curved surfaces. The flat lamellar mesophase, however, has to be treated separately and provides a lower free energy for volume fractions $f \gtrsim 0.3$, which is highlighted by a vertical line. For $f \approx 0.25$ the preferred surface corresponds to a cylinder, for $f \to 0$ to a sphere. The deducible transitions between the classical phases are in agreement with [74], and smaller deviations can be attributed to the different treatment for the free energy of brushes grafted to the convex side of the interfaces.

space and have just referred to the observed mesophases as possible realizations of certain curvatures. This question for the optimal embedding is in general far from trivial and gives rise to the formation of only a certain number of suitable structures. Specifically, we have to take into account that polymer chains in the melt state have to fill space uniformly. For a clarification of this problem consider the case $f \approx 0.25$ where the system wants to form cylindrical interfaces. Hence, the overall structures will consist of an arrangement of cylinders, where the inside of the cylinders is filled by the minority species and the surroundings are occupied by the majority component. While our previous derivation shows no problem for treating the inner part of the cylinder (as long as different cylinders do not intersect), the treatment of the brushes on the outer (convex) side of the cylinders relies strongly on the precise arrangement of these cylinders in space. Our derivation assumed that the outer brush is bounded by a parallel surface at distance r_{Out} to the interface which encloses the minority component, cf. the left part of figure 3.6. However, these cylinders can not be arranged such that they fill space on the one hand and do not intersect each other on the other. Rather, certain parts of the outer brush would have to stretch further than the others to fill the remaining portions of space. The higher the deviations in these stretching radii, the higher the free energy. Hence the optimal arrangement yields the smallest deviations for the radii of the outer brush and corresponds to the hexagonal arrangement shown in figure 3.6 where the outer brushes are confined to hexagonal prims rather than cylinders. The inability to have both, interfaces with constant curvature and polymer brushes with homogeneous height is termed packing frustration and this concept will be transfered to melts of copolymers of different architecture in chapter 4. Analogously, for $f \to 0$ where the surfaces of preferred curvature are spheres, we must find the most homogeneous packing of

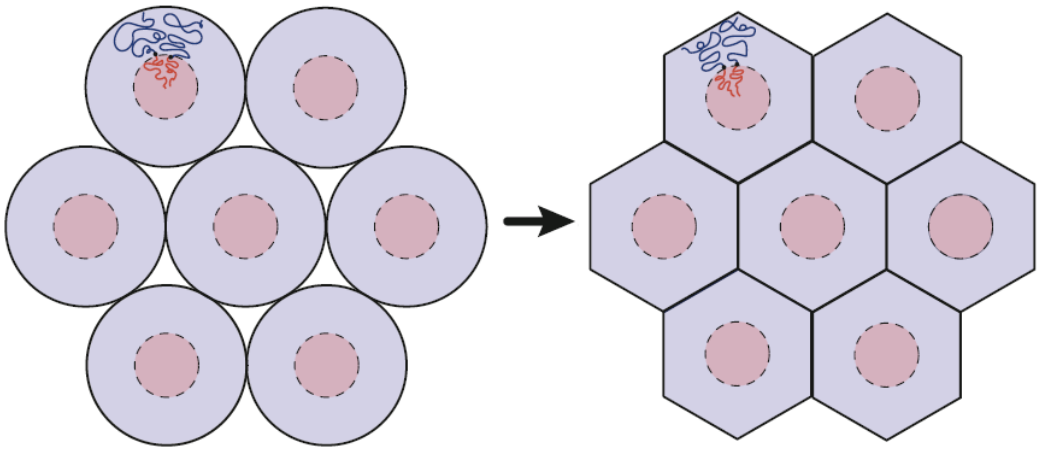

Figure 3.6: Illustration of packing frustration for the cylindrical microphase in a diblock copolymer melt. The minority component of the copolymer (shown in red) occupies the inner part of the cylinders, thereby allowing the majority component (shown in blue) to be located at the outer part of the cylinders. This configuration is beneficial for the stretching of the majority component and therefore also for the whole molecule. Ideally, the height of the outer brush should be uniform, which would result in the formation of perfect cylinders, as shown on the left. However, in the melts state the polymers have to uniformly fill space which requires them to fill the gaps between the perfect cylinders. The resulting configuration is shown on the right where the outer brushes form hexagons rather than cylinders. The picture has been adopted from [22].

spheres that minimizes deviations in the radii (or heights) of the outer brushes. This is given by the body-centered cubic arrangement. For the bicontinuous phases located between the lamellar and cylindrical mesophase, the deviations of brush height occur primarily for the minority component which forms network-like labyrinth, cf. section 3.3. Here, deviations in the channel radii of the labyrinths can be mapped to deviations in the height of the brushes, which identifies the Gyroid structure as the best suited candidate of all possible morphologies [71]. The lamellar phase on the other hand is free from any packing frustration.
In reality, the interfaces are not given by surfaces of perfectly constant curvature but show deviations from these to attenuate the effects of inhomogeneous brush heights on the cost of higher surface areas. A study examining these interfaces for finite segregation strength by employing the spectral method of the SCFT, cf. section 2.3, is given in [50]. This study examined the mean curvature of interfaces in different mesophases and linked deviations in the mean curvatures to the need to account for the packing frustration of the respective morphology.

3.3 Bicontinuous mesophases

Let us have a closer look at the bicontinuous Gyroid morphology, situated between the lamellar and the cylindrical mesophase in the phase diagram, which allows for interfaces with negative Gaussian curvature. These interfaces can be described by parallel surfaces to both sides of the so-called Gyroid surface, shown in figure 3.7. The Gyroid surface is a triply-periodic minimal surface, which means that its mean curvature vanishes identically.

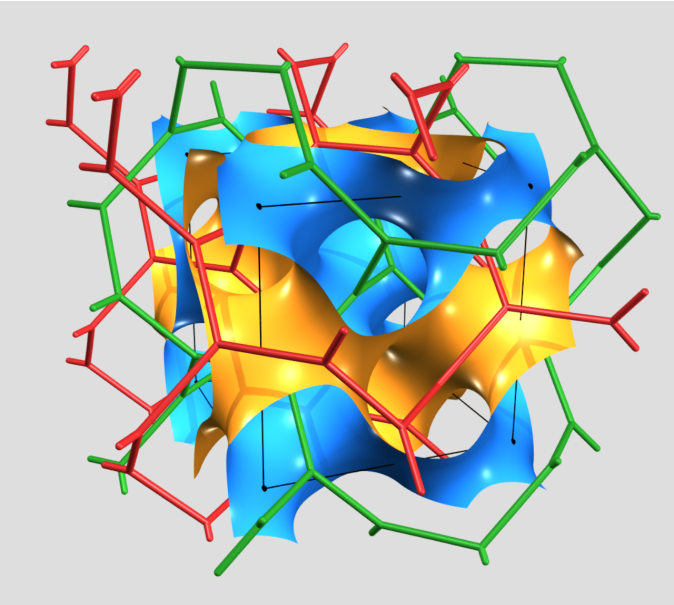

Figure 3.7: The Gyroid surface, colored blue on one side and orange on the other Also shown are the so-called *srs* nets [65] which characterize the two domains separated by the Gyroid surface. Both nets are enantiomers and are shown in green and red, respectively. In diblock copolymer melts, the minority component occupies the regions corresponding to a dilated version of both nets. The majority component separates both networks and can hence be described by a dilated version of the Gyroid surface. The picture has been taken from [35].

Furthermore, it provides an embedding of a two-dimensional surface with negative Gaussian curvature in three-dimensional space. The key point, which is one of the reasons for its occurrence in nature, is that the Gyroid surface is one of the best embeddings of a triply-periodic surface in terms of minimizing deviations in Gaussian curvature. Therefore, it allows for triple-periodic parallel surfaces with narrow mean curvature distributions to both of its sides and, in fact, divides space into two labyrinths of identical volume. Each labyrinth is a continuous[2] object and can be characterizes by a three-dimensional net which visualizes its topology, as shown in figure 3.7. The interfaces between the polymer species can then, to a first approximation, either be described as parallel surfaces to this Gyroid surface, or they can be seen as the surfaces of a dilated version of both nets. Since the parallel surfaces yield very homogeneous mean curvature distributions, they are ideal for self-assemblies of diblock copolymer melts provided the preferred curvature matches the average curvature of the parallel surfaces. Additionally, these parallel surface could be transformed to constant mean curvature surfaces by slight deformations. Besides the need for constant mean curvature interfaces, we also need to account for the packing frustration in a morphology. In fact, when it comes to the described construction via minimal surfaces, the Gyroid allows for a very homogeneous packing of polymer chains. If we approximate the interfaces between the species by parallel surfaces, the variation in the height of the brushes pointing towards the minimal surface would vanish by definition. Also, the variation in height for the brushes on the other side of the interfaces is relatively narrow [71]. This explains the ubiquity of the

[2]This means that for each pair of two points located in the same labyrinth, there will be a path connecting these points which lies fully inside this labyrinth.

Gyroid in many self-assembled systems [31, 35].

There are also two additional bicontinuous morphologies found in certain systems of diblock copolymers or related molecules, e.g. lipids or surfactants. They are, however, absent in diblock copolymer melts. These are based on the Diamond and the Primitive triply-periodic minimal surfaces. Like the Gyroid surface, these surfaces also minimize variations in Gaussian curvature. However, their network domains are not as homogeneous in terms of their channel radii leading to higher packing frustrations [71]. For this reason these structure are not stable in the melt state but can form when additional components are present. For surfactants one usually has an additional solvent present in the system. In the case of diblock copolymers, the addition of homopolymers of the minority species, which occupy the space otherwise filled by highly stretched chains, can relieve this packing frustration and stabilize other bicontinuous phases [46].

Further extensions of the molecular architecture can also result in mesophases where one or multiple polymeric species form a continuous network-like labyrinthine domain. As a natural extension of diblock copolymers consider linear triblock copolymer, cf. figure 1.1(b), where an additional polymer chain of a third species is attached to a free end of the diblock copolymer. A study investigating ordered network phases in these systems can be found in [15, 57].

3.4 Tricontinuous mesophases

The finding of structures characterized by two network-like intertwined labyrinths has led to the examination of possible geometries for these bicontinuous phases and to the search for possible extensions of tricontinuous phases. Instead of just two channels, tricontinuous morphologies exhibit three intertwined domains. Just like the bicontinuous structures, these structures can be described by triply-periodic minimal surfaces. However, they exhibit additional branch lines where three surface patches meet. The branch lines also present one-dimensional regions in space where all three network domains meet. A mathematical discussion of such structures and their role for self-assembled soft-matter systems has been given in [36]. Based on curvature arguments one of these morphologies, which we call the $3etc(193)$ structure, was proposed as a suitable candidate and was in fact afterwards discovered experimentally [25]. Figure 3.8 shows the branch lines and the minimal surfaces in a unit cell of the $3etc(193)$ structure. The experimental observation [25] of a tricontinuous mesoporous material with a silica pore wall used a specially designed cationic surfactant template and is therefore a prime example for a self-assembled tricontinuous structure. The surfaces which separate distinct species, in this case the silica from the pore space, can be approximatively seen as parallel surfaces to patches of minimal surfaces that separate space into three network-like domains. Based on the curvature arguments of section 3.2, this tricontinuous structure is thus located between the lamellar and the cylindrical phase.
We used the spectral method, cf. section 2.3, to test the stability of this tricontinuous structure in diblock copolymer melts. To achieve this, we calculated the free energies of all morphologies observed in diblock copolymer melts, as well as the free energy of the $3etc(193)$ structure. We assumed a segregation strength of $\chi N = 16$ and looked at volume fraction in the interval $0.3 \leq f \leq 0.42$. Figure 3.9 shows the resulting free energies. By identifying the mesophases of lowest free energy, we can deduce the volume fractions for which the individual structure are stable. Our calculations are in agreement with the phase diagram shown in figure 3.2. The tricontinuous structure, however, does not represent the equilibrium mor-

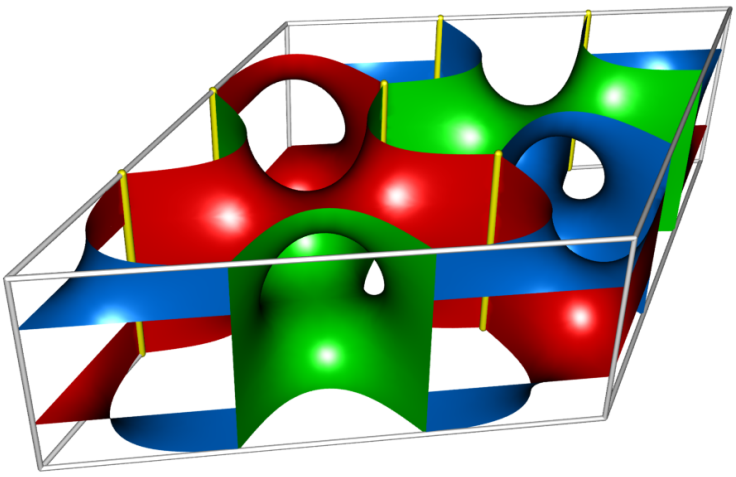

Figure 3.8: Branch lines (yellow) and minimal surfaces (red, green and blue) in a unit cell (framed by white lines) of the $3etc(193)$ structure. This tricontinuous structure divides space into three intertwined labyrinths, indicated by the three colors of the minimal surface. Each colored side points into one of these network-like labyrinths.

phology for any considered parameter. However, it is close to the lowest free energy at the transition from the Gyroid to the hexagonal cylindrical phase.
Furthermore, we minimized the free energy of the $3etc(193)$ structure with respect to its c/a ratio. The optimal ratios we found correspond extremely well to the experimentally found ratio of $c/a \approx 0.954$ with an error of ± 0.005.
If we wish to argue that the SCFT should be able to predict the stability of this tricontinuous phase we have to account for discrepancies between the experimental conditions and the assumptions that went into our calculations. Some of these differences could be overcome by making alterations to the SCFT, for example by changing the statistical segment lengths of both species, by altering the degree of immiscibility χN, or by adding additional components, e.g. solvents, to the diblock copolymer system. However, there could be different effects, which can not be incorporated in the present SCFT treatment, that lead to the formation of the $3etc(193)$ structure. These could be fluctuation effects, further types of interaction present in the experimental system, e.g. due to the silica source, or dissimilarities between the high-molecular weight polymer regime and the driving forces controlling the smaller surfactant molecules used in the experiment. The tricontinuous morphology could, however, just be a metastable state in which the dynamics of the system gets stuck. This is believed to be the case for the hexagonally perforated lamellar (HPL) phase in the experimental phase diagram for polyisoprene-polystyrene diblock copolymers, cf. figure 3.3.

Nevertheless, the study [25] shows that careful design of molecular constituents can lead to the formation of complex, tricontinuous morphologies. We note that the observation of another tricontinuous structure in thermotropic liquid crystals has also been published [86]. Besides the existing tricontinuous structures, polycontinuous structures with an even higher number of intertwined continuous network domains could in principle be valid models for self-assembled morphologies in soft-matter systems. A discussion based on curvature and packing arguments is a wise starting-point to identify suitable candidates for self-assembled

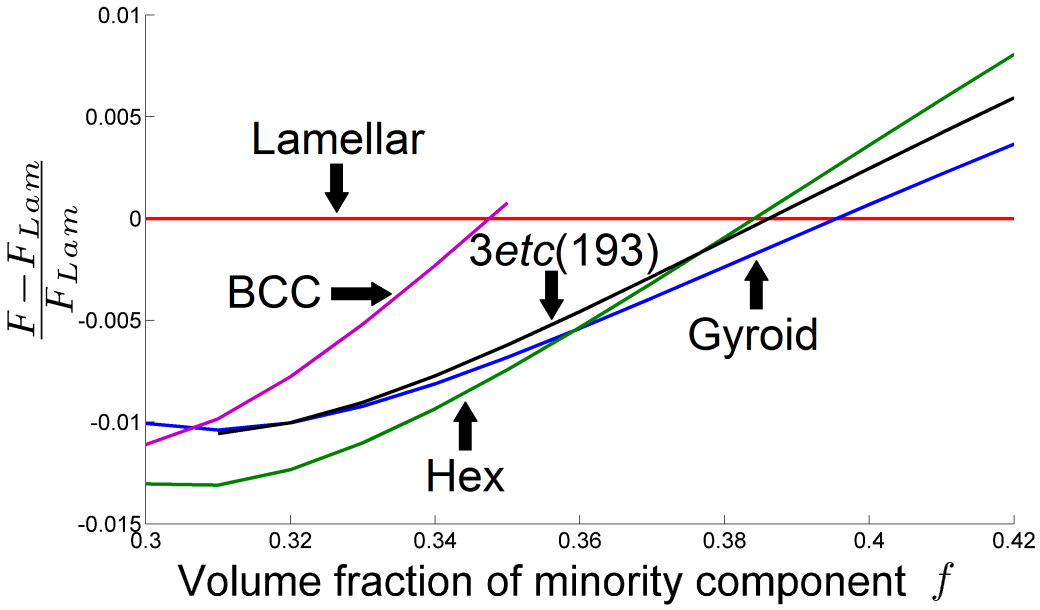

Figure 3.9: Relative free energies, cf. (2.107), plotted against the volume fraction of the minority component, f, for a diblock copolymer melt at segregation strength $\chi N = 16$, assuming identical statistical segment lengths for both species. For the purpose of comparability, we plot the relative free energy difference between the respective morphology (with free energy F) and the lamellar phase (with free energy F_{Lam}), evaluated at the same volume fractions. Besides the mesophases observed in diblock copolymer melts, we also examine the $3etc(193)$ structure. The morphology with the lowest free energy, for a fixed value of f, represents the equilibrium phase at that volume fraction. The transitions between different phases are in agreement with figure 3.2. The tricontinuous structure, however, is not thermodynamically stable at any volume fraction.

morphologies in systems of diblock copolymers, surfactants or lipids [72].

In this thesis, however, we will focus not on diblock copolymers, but on star-shaped (triblock) copolymers. The curvature arguments we present in this chapter are not directly transferable for these architectures, but the derivation of the concepts of preferred curvatures from the SST can be altered leading to different driving mechanism for the self-assembly of star-shaped molecules. However, these mechanisms are established on the same theoretical basis and the same methods can be used to examine the formation of tricontinuous structures in melts of star-shaped copolymers.

Chapter 4

Triblock star-copolymer self-assembly

In chapter 3 we saw that bicontinuous structures can form in melts of diblock copolymers. The extension of bicontinuous morphologies are tricontinuous morphologies for which we present some examples in chapter 5. This thesis is devoted to the question whether tricontinuous structures can be observed in triblock copolymer systems, whereby each of the three polymeric species forms one of the three network-like labyrinthine domains.
However, it is not initially clear how the chains of the third polymer species should be attached to the diblock copolymer. The two immediate possibilities are the formation of a linear or a star-shaped molecule, cf. figure 1.1. Furthermore, the parameter space of the three component system is much larger compared to the two component system due to the existence of two independent volume fractions as well as interactions between each pair of species. In this thesis we restrict ourselves to the most symmetric case of triblock polymer architectures, being (balanced) triblock star-copolymers, figure 1.1(c), with equal volume fractions for all species and identical interactions between all of them. We note that network-like structures have been found and investigated in linear triblock copolymers. However, these morphologies usually exhibit up to two network-like domains, each of which is filled by an individual species. These domains are then embedded in a matrix formed by the remaining component, cf. [15, 76, 57]. We on the other hand are looking for structures which in fact yield three network domains. For this purpose, we investigate star-shaped triblock copolymers. In the balanced case (i.e. equal interactions and volumes) it can be expected that the three domains are of identical shape and therefore might form three identical networks.

As has been shown by experiments [55], the morphologies observed for triblock star-copolymers over a wide region of their phase space are a variety of columnar arrays which reveal polygonal tilings in their cross sections, cf. figure 1.4. A treatment by the aforementioned numerical real space SCFT methods [78, 41] focuses on some of these tilings. In the case of equal volume fractions and equal interactions one usually observes the 6.6.6 tiling reminiscent of a three-colored honeycomb structure, also depicted in figure 1.4. Clearly, these morphologies do not have the three-dimensional complexity we are looking for and hence it is necessary to change the molecular architecture in order to tune the self-assembly process such that it forms more complex mesophases. We employ the SST to understand the reasons for the self-assembly process in triblock star-copolymer melts in this chapter,

before using the more accurate numerical methods in chapter 6.

Section 4.1 applies the SST to the usual triblock star-copolymers and introduces the geometric ideas responsible for the self-assembly process of these molecules. We find that the equilibrium solution for balanced triblock star-copolymers, the honeycomb pattern, has the drawback that polymer chains have to stretch in an unfavorable way, thus yielding high packing frustration.

We can further stress these stretching effects by introducing an extended or functional core to the center of the triblock star-copolymers. By using the expressions of the SST, we show that terms associated with this stretching contribution can be further pronounced. This allows us to destabilize the formation of the honeycomb pattern and hence facilitates the observation of novel structures. Section 4.2 demonstrates this ideas and introduces a geometric measure which relates the arrangement of the molecular centers in a given structure to its stretching contribution to the free energy.

In chapter 5 we will then determine these stretching contributions, or equivalently the packing frustration, associated with different columnar and tricontinuous candidate structures. Furthermore, we quantify the energy contributions due to their interface geometries. An understanding of the driving forces governing the self-assembly process in triblock star-copolymer melts can be obtained by using these two measures. The geometric ideas and design principles developed here will be substantiated by the construction of the phase diagram with the full numerical SCFT method in chapter 6.

4.1 Strong segregation theory for triblock star-copolymers

In the strong segregation limit the individual chains of a (simple) triblock star-copolymer are highly stretched away from their common covalent bond in the molecular center. Therefore, we have to deal with extended polymer brushes for each species, which are grafted to quasi-one-dimensional regions where the covalent bonds are located. We refer to them as the branch lines of a given mesophase. The contacts between pairs of chemically distinct species are limited to thin interfaces that separate the individual polymer brushes. All interfaces are terminated by branch lines and each branch line has three interfaces, each corresponding to a particular pair of species, attached to it. The contributions to the free energy are due to the interfacial tension associated with these interfaces on the one hand, and the stretching of all polymer brushes on the other, as has been discussed in section 2.2. The free energy per copolymer and in units of k_bT, cf. equations (2.66) and (2.78), for a simple triblock copolymer is then in general given by

$$\frac{F}{nk_BT} = \frac{1}{2} \sum_{I \neq J \in \{A,B,C\}} Na\sqrt{\frac{\chi_{IJ}}{6}} \frac{A_{IJ}}{V} + \sum_{I \in \{A,B,C\}} \frac{3\pi^2}{8 f_I^2 Na^2 V} \int_{V_I} d^3r \; z^2(\vec{r}), \tag{4.1}$$

where A_{IJ} is the surface area of all interfaces between the domains occupied by species I and J, respectively. V_I represents the spatial volume which defines domain I and V is the total volume of the system. $z(\vec{r})$ denotes the polymeric path distance between the volume element at position $\vec{r}$ and the position on the branch line where polymer chains stretching into this volume element are attached.
We note that different molecular architectures can be used to change certain parameters. The statistical segment length a, for example, could be different for each polymer species

accounting for different stiffnesses of distinct polymer chains. While f_I is fixed for given volume ratios between the polymer species in a simple triblock copolymer system ($f_I = 1/3$), its value can be altered by changing the detailed molecular architecture. Attaching multiple chains of each species to every copolymer, instead of using just one chain per species, changes the formula (4.1), which can effectively be described by changing the values f_I, cf. [60]. The use of branched instead of linear polymer chains has similar effects [22]. Thus we will continue to use the parameters f_I instead of inserting assumed volume fractions to take this into account. The parameter a, however, is assumed to be equal for all species and we absorb its deviations in other parameters. In the case of the second term in (4.1) this can be accounted for by different values of f_I. For the first term, an asymmetry of the statistical segments lengths a of two polymers at an interface will effectively change the interfacial tension [27], which we can absorb in the interaction strengths χ_{IJ}.

Let us now restrict to the case of balanced triblock star-copolymers with formally identical polymer chains for all species. Therefore, we are left with a single parameter, $f_I = f \ \forall I$. Additionally, the χ_{IJ} parameters are assumed to be equal for all possible interactions, $\chi \equiv \chi_{AB} = \chi_{AC} = \chi_{BC}$. Expression (4.1) then takes the form

$$\frac{F}{nk_BT} = Na\sqrt{\frac{\chi}{6}}\frac{A_{ABC}}{V} + \frac{3\pi^2}{8f^2Na^2V}\int_{V_{ABC}} d^3r \; z^2(\vec{r}), \tag{4.2}$$

where A_{ABC} is the total surface area of all interfaces between two distinct domains. V_{ABC} denotes the volume region associated with the domains of species A, B, C. At this point of the analysis this simply corresponds to the total volume of the system. Note that it suffices to evaluate this expression for a single unit cell of the respective morphology.
The first term in (4.2) describes the energy cost due to unfavored contacts between distinct polymer species and can effectively be seen as the product of a surface tension times the surface area of the interface, A_{ABC}. The second term is the entropic cost caused by stretching polymer chains within the structure. Due to the incompressibility of the copolymer melt, the chains have to stretch in order to assure equal density throughout the whole system. Let ξ be the unit cell size of the respective structure. The first contribution will change proportional to $1/\xi$, the second one proportional to ξ^2. The structure will choose a lattice scaling such that its total free energy will be minimized, cf. (D.1) and (D.3) in the appendix. After performing this minimization the free energy is given by

$$\frac{F}{nk_BT} \propto \left[\frac{A_{ABC}^2}{V^3}\int_{V_{ABC}} d^3r \, z^2(\vec{r})\right]^{\frac{1}{3}}, \tag{4.3}$$

where we neglected coefficients which are independent of the structures geometry and are hence irrelevant for deciding which structure represents the minimum free energy solution. In the case of diblock copolymers the nodes between the different polymer chains were located at the interfaces and $z(\vec{r})$ was roughly the distance between a volume element and its closest interface. The combination of both free energy contributions then resulted in different preferred interface curvatures, depending on the volume fractions of the two polymer chains, cf. section 3.2. In triblock star-copolymers on the other hand, expression (4.3) will not result in preferred interface curvatures since we do not have an interface between a pair of brushes but rather three polymer brushes which are grafted to a common branch line.

We noted in section 2.2 that the presented integrals in (4.1, 4.2, 4.3) are known not to be perfectly accurate even in the SST limit. Firstly, one has to account for the effects of the

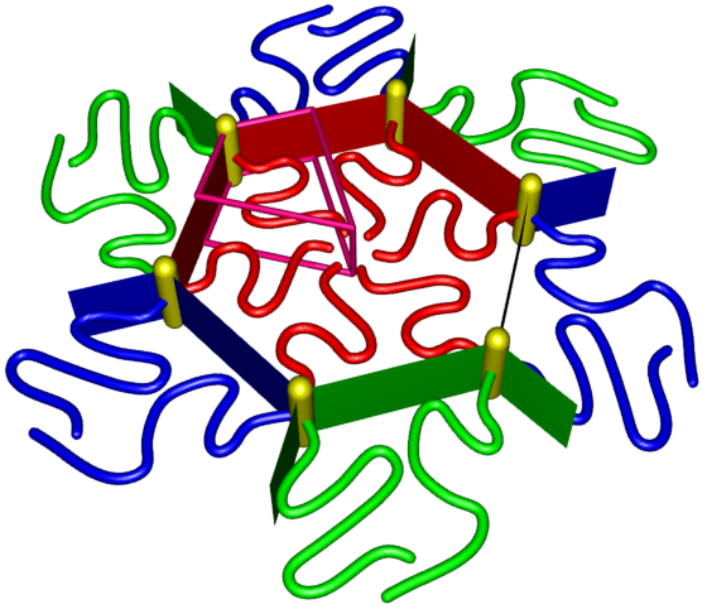

Figure 4.1: Artistic representation of the honeycomb structure, self-assembled by balanced triblock star-copolymers. The molecules are arranged such that polymers of each individual species (red, green and blue) form columnar arrays with hexagonal cross section. The branch lines (shown in yellow) are located at the corners of these hexagons. Interfaces between distinct polymer species are indicated as surfaces connecting these branch lines and are colored such that each side of the surface adopts the color of the domain it is facing. The purple framed region indicates the volume occupied by red chains attached to a specific branch line. Its shape allows to asses the degree of packing frustration in this morphology.

exclusion zone [3, 5] which are, with regard to simple triblock star-copolymers, important for the highly convex brushes emerging from quasi-one-dimensional lines. The other important correction is due to the equality of grafting densities for all three polymer brushes at each point on the branch lines, cf. [42]. This means that the (infinitesimal) region occupied by chains of species A emerging from a particular point at the branch lines has to have the same volume as the regions occupied by chains of species B or C which are attached to the same point. The precise shape of these brush regions rely on the choice of the (possibly curved) polymeric paths. Therefore, these paths have to be chosen accordingly, making an accurate calculation of the integral non-trivial.
Per definition, morphologies in balanced triblock star-copolymer melts are required to have equal volumes for all three domains. Since there is nothing which would allow one domain to stand out against the others, we further assume that all domains are congruent.
The structure observed in experiments is the 6.6.6 tiling [55], henceforth called honeycomb structure for the sake of convenience, which allows for interfaces with the least surface area between the three distinct domains. Figure 4.1 gives an artistic impression for the self-assembly of triblock star-copolymers in this mesophase. Morphologies based on the honeycomb are observed in a variety of other physical systems where interfaces are employed to divide space into different compartments under the influence of surface tension. Therefore, the formation of the honeycomb structure is evident with regard to the surface tension term in (4.2). However, we also have to take the stretching of polymer chains into

account, encoded by the second term in (4.2). In fact, we demonstrate that the honeycomb does *not* provide a suitable structure for minimizing the stretching of polymer chains and therefore suffers high degrees of packing frustration.

To begin with, recall the discussion of packing frustration in diblock copolymer melts in section 3.2 which tells us that the polymer brushes should be globally packed such that they minimize their stretching contribution. In the melt state, this leads to a close packing of polymer brushes with as little deviations in the brush heights as possible. In diblocks this packing was, for example, realized by arranging cylinder forming brushes in a hexagonal (close packed) arrangement or by arranging spherical brushes in a body-centered cubic arrangement. Both configurations yield the most homogeneous solutions in terms of brush heights for the respective topology. In triblock star-copolymers we necessarily are confronted with polymer brushes grafted to one-dimensional branch lines which resembles the cylindrical mesophase in diblock copolymer melts when considering packing frustration effects. The best solution to the packing problem is demonstrated by nature itself which self-assembles diblock copolymers into the hexagonal close-packed arrangement of cylinders whereby the centers of the cylinders form a triangular lattice, cf. figure 3.6. The analogous preferred arrangement for triblock star-copolymers would then be to arrange the branch lines in this triangular lattice with three chemically distinct polymer brush emerging from each line. The domains formed by each individual species and the interfaces between pairs of polymer species must somehow comply with this arrangement. We introduce two columnar structures which adopt this arrangement of branch lines, as well as a tricontinuous structures which comes fairly close to it, in chapter 5 for this very reason. The arrangement of branch lines in the honeycomb structure, however, differs significantly from a triangular lattice. A closer look at the alignment of branch lines reveals that it is far from being perfect with respect to packing frustration because chains emerging from the branch lines have to stretch far into the center of the hexagonal domains to fill space evenly, cf. figure 4.1 and figure 4.2(a). A good way to illustrate this stretching effect in the view of SST is to look at the volumes closest to each branch line. These approximately represent the regions in space which will on average be filled by polymer chains emerging from the respective branch line. This region, i.e. the Voronoi cell of the branch line, is indicated by the purple frame in figure 4.2(a) and possesses a triangular shape in the case of the honeycomb structure. In order to minimize stretching costs, the shape of these volumes should be as close to a cylinder as possible, thereby avoiding that some volume elements are much farther away from the branch line than all others.

The honeycomb structure yields Voronoi cells with triangular cross sections affording a space filling tiling of the plane but has the disadvantage that chains extending into the edges of these triangles have to stretch relatively far. Quadratic and hexagonal instead of triangular Voronoi cells would also tile the plane by regular polygons, as demonstrated in figure 4.2(b) for the latter case, but would furthermore reduce the packing frustration.

Certain arrangements of branch lines thereby lead to a favorable structure from a purely entropic point of view. For a given branch line arrangement, however, interfaces have to be inserted in order to divide the structure into three domains giving rise to energy costs associated with the surface area of these interfaces. In the next chapter, we present different tricontinuous structures with arrangements of branch lines that are favorable in terms of packing frustration and that furthermore allow for only slightly higher interfacial energies.

The next section shows that the introduction of an extended or functionalized core to the centers of the copolymers exacerbates the importance of packing frustration. This destabilizes the honeycomb structure, forming in the usual triblock star-copolymer melts, and leads the way to self-assembly of other intricate geometries.

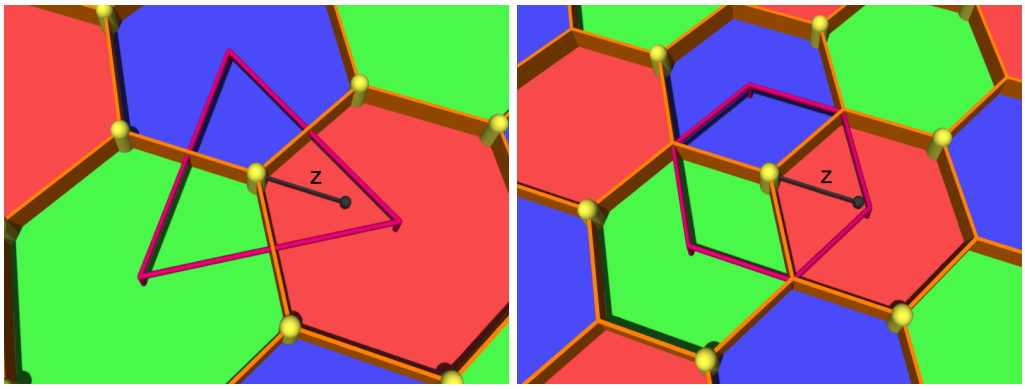

(a) (b)

Figure 4.2: Schematic representation of the degree of chain stretching, also termed packing frustration, present in two columnar phases. Different colored areas (red, green, blue) indicate domains occupied by distinct polymer species. These domains are separated by interfaces (shown in orange). The branch lines (shown in yellow) indicate the location of the molecular centers of the triblock star-copolymers. Each branch defines its own Voronoi cell. As an example, one of these Voronoi cells is framed by purple lines. These regions are defined as all volume elements which are closer to this respective branch line than to any other and represent the regions into which chains emerging from the branch line must extend. For clarity, one of these volume element is depicted by a black dot and its distance to the next branch line, which in this simple case corresponds to the polymeric path distance z, is indicated. (a) The usual honeycomb structure. The Voronoi cell adopts a triangular shape which results in high deviations of brush heights, i.e. high packing frustration, because chains extending into the outer corners of the triangles (i.e. into the centers of the hexagonal domains) have to stretch much farther than chains moving parallel to an interface. (b) The alternative honeycomb structure, cf. chapter 5, is obtained by placing branch lines at every second corner of the hexagonal domains. The Voronoi cell of this structure has a hexagonal cross section, which is closer to the ideal (but in the melt state not realizable) cylindrical shape compared to the triangular shape in (a). Therefore, this structure yields more homogeneous brush heights and reduced packing frustration on the cost of higher interfacial areas. The scale of (a) and (b) is chose such that the areas of the Voronoi cell cross sections are equal in both cases.

4.2 Effects of introducing an extended core into star-copolymers

The precise influence of a core in the center of triblock star-copolymers can be treated in different ways, each corresponding to different experimental realizations, cf. figure 4.3. We present some of the more relevant constructions and show their influence on the geometrical understanding of the self-assembly process. Our focus will then be directed to the realization of the core by a fourth polymer species. This new species forms an extended center of the molecule onto which the other chains are attached, see figure 4.3(c), enabling us to examine this type of system with the usual SCFT and SST methods. However, different types of realizations are conceivable, e.g. rigid cores, figure 4.3(a), representing aromatic molecular centers, and will result in qualitatively comparable results. Further connections

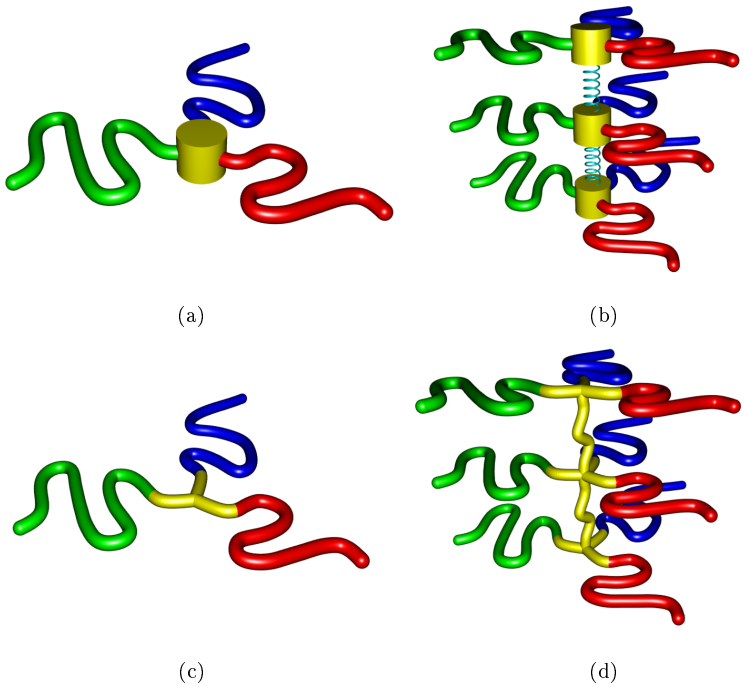

Figure 4.3: Delineation of possible architectures of star-copolymers with a functional and extended core. Three polymer chains of different species (red, green and blue) are attached to a core in the molecular center, shown in yellow. (a) The core is modeled as a rigid object, indicating a realization based e.g. on an aromatic molecular center. (b) Same as (a) but additional molecular features of the core can induce bonds between adjacent copolymers. (c) The core is modeled by a star-shaped configuration of polymer chains of a fourth species to which the other chains are attached. This allows us to treat these molecules with the usual SCFT methods. (d) Same as (c) but the polymer chains in the molecular center are connected to adjacent centers. This model shows the possibility of assuming bonds between copolymers even in the purely polymeric regime. Here, the system consists of dendronized polymers rather than single copolymer molecules.

to experimental situations will be given in chapter 7 at the end of this thesis.

To begin with, let us utilize the core to impose some sort of bond between adjacent cores, as illustrated in figure 4.3(b) or figure 4.3(d). This can be achieved chemically in several ways. Also, there are numerous approaches to model these interactions theoretically. We could, for example, postulate a fixed distance between adjacent molecules or model the bonds as springs between neighboring cores. However, let us for the sake of simplicity just assume that the bonds between adjacent cores will result in fixing the *average* distance between the molecules. Starting again from (4.2), we are in this case not able to perform the minimizations with respect to the scaling of the unit cell since this would violate our assumption of fixed molecular distances. In fact, by fixing the average distance between molecules, h, as well as the volume of each copolymer, $\frac{N}{\rho_0}$, we obtain the conditions $hn = L$ and $\frac{N}{\rho_0} n = V$, where L is the total length of branch lines in the structure. These restrictions will not allow the system to choose the scale of the unit cell, ξ, to minimize its free energy

as before, but will rather set ξ, leading to the final expression for the free energy

$$\frac{F}{nk_BT} \propto \tilde{h}\frac{A}{\sqrt{LV}} + \frac{L}{V^2}\int_{V_{ABC}} d^3r\, z^2(\vec{r}), \tag{4.4}$$

where we defined

$$\tilde{h} \equiv \left(\rho_0 h a^2\right)^{\frac{3}{2}} \frac{8}{3\pi^2\sqrt{6}}\sqrt{\chi_{AB}N}f^2. \tag{4.5}$$

Note that the effects of the exclusion zone still may lead to significant deviations in this expression. Furthermore, the condition regarding the grafting densities of polymer chains is still present. The main insight from the free energy in (4.4) is that it consists of two contributions, both of which provide geometric measures for a structure. The balance between them can be tipped in either way by appropriately changing the value of $\tilde{h}$. The first expression, $A/\sqrt{LV}$ is an appropriate measure to quantify the free energy due to the interfacial area within the structure, whereas the second one, $L/V^2\int_{V_{ABC}} d^3r\, z^2(\vec{r})$, assesses the stretching free energies due to packing frustration effects and is given by the arrangement of branch lines and, in addition, by the precise form of the polymer paths emerging from them. By changing the average distance of molecular centers we can therefore, in principle, increase the importance of packing frustration compared to the interfacial tension. We carry on by extending this concept to other realizations involving an extended core, which will eventually afford a more rigorous and quantitative analysis by the full SCFT method.

Let us therefore consider another approach which assumes that our copolymers have the form depicted in figure 4.3(c) and hence have a fourth polymeric species, X, forming the molecular core. In the following, the volume fractions of this species is denoted ϕ, whereas f_X denotes this volume fraction plus additional architectural effects, for example due to stiffer polymer chains in the core. Assuming the core occupies the volume region V_X we therefore have $\frac{1}{V}\int_{V_X} d^3r = \phi$. For simplicity, we assume that the interactions between species X and every other species (X-A, X-B, X-C) are equal, $\chi_X \equiv \chi_{AX} = \chi_{BX} = \chi_{CX}$. The free energy (4.1) now has to account for additional interfaces enclosing the core region, as well as the fact that the polymer brushes are not grafted to quasi-one-dimensional lines anymore but rather to these new interfaces,

$$\begin{aligned}\frac{F}{nk_BT} =& \frac{Na}{\sqrt{6}}\left[\frac{\sqrt{\chi}A_{ABC} + \sqrt{\chi_X}A_X}{V}\right] \\ &+ \frac{3\pi^2}{8Na^2V}\left[\frac{1}{f^2}\int_{V_{ABC}} d^3r\; z^2(\vec{r}) + \frac{1}{f_X^2}\int_{V_X} d^3r\; z^2(\vec{r})\right],\end{aligned} \tag{4.6}$$

A_X denotes the surface area of the interfaces between the polymeric core and the other species. In (4.6) $z(\vec{r})$ describes the polymeric path distance between a certain volume element and its associated point on these interfaces. The first integration is performed over the volume which is not occupied by the core, V_{ABC}, and, similarly to before, represents the stretching of polymer chains of species A, B, C which are now grafted to the interface between the core and the rest of the system and must stretch in order to fill the volume V_{ABC}. Additionally, there is a entropic contribution due to the stretching of chains of species X in the core volume V_X. As usual, we minimize with respect to the size of the unit cell, cf. equations (D.1) and (D.4). The free energy then takes the form

$$\frac{F}{nk_BT} \propto \left\{\frac{\left(A_{ABC} + \sqrt{\frac{\chi_X}{\chi}}A_X\right)^2}{V^3}\left[\int_{V_{ABC}} d^3r\, z^2(\vec{r}) + \left(\frac{f}{f_X}\right)^2\int_{V_X} d^3r\, z^2(\vec{r})\right]\right\}^{\frac{1}{3}}. \tag{4.7}$$

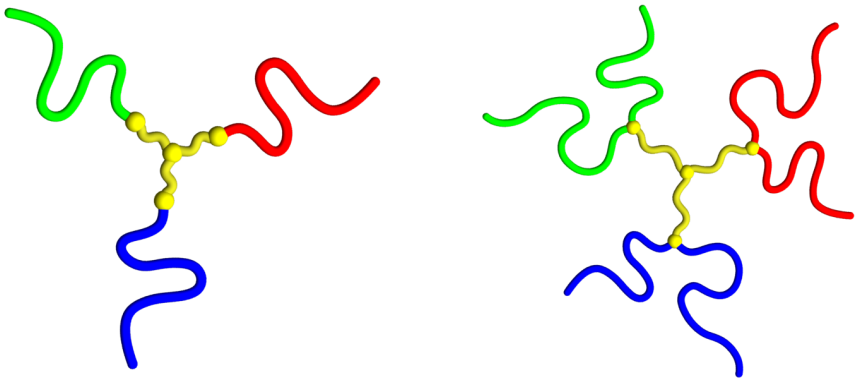

(a) (b)

Figure 4.4: Molecular architectures of special interest for this thesis. The red, green and blue chains form the outer brushes in the meshophases and the yellow chains form the core region which can be seen as a dilated version of the branch lines of the simple triblock star-copolymer system. Yellow dots indicate covalent bonds between distinct polymer chains. (a) Triblock star-copolymer with an extended polymeric core, cf. figure 4.3(c). (b) Same as (a) but with two chains of each outer species attached to the polymeric core. This dual-chain triblock copolymer architecture will pronounce the stretching contribution of the outer brushes when compared to the stretching in the polymeric core.

The coefficient $(f/f_X)^2$ weights the importance of the stretching of chains in the core domain V_X relative to the stretching of the outer brushes and is set by the volume fractions of species A, or equivalently B or C, and species X. However, as has been pointed out, these fractions can be further altered by changing the molecular architecture [60]. As we mentioned ϕ simply denotes the volume fraction of species X while f_X also incorporates these effects. Likewise, the volume fraction of each outer brush (A, B, C) is given by $(1-\phi)/3$ whereas f incorporates architectural effects. Using stiffer polymers of species X will effectively increase the value of f_X and is conceptually closer to the idea of a rigid core. Furthermore, the value of f can effectively be lowered by attaching multiple arms of each species A, B, C to the polymer chains of species X in the center of the molecule, cf. figure 4.4(b). Both architectural changes will therefore decrease the ratio $(f/f_X)^2$ allowing us to focus on the stretching of the outer brushes.
We briefly reassess the effects of the exclusion zone, which are still present in the outer (convex) brushes of species A, B, C. For a sufficiently extended core region, however, these corrections become negligible since the curvature of the grafting surface decreases [3]. For the polymer brushes of species X on the other hand, we do not have an exclusion zone because these are located on the concave side of the interface [74]. Instead, we have the situation that three polymer chains of this species are connected in the center of each molecule, see figures 4.3(c) and 4.4. Due to this connection we expect changes to the presented integral expression for the core domain. The resulting corrections are, however, expected to be minor for strongly stretched brushes [60].

The main correction which still has to be taken into account, especially when looking at mesophases in melts of triblock star-copolymers with extended cores, is that grafting densities at the interfaces of the core should be locally equal for polymer chains belonging to the core and for those of the outer species [42]. For copolymer architectures involving

multiple chains of a particular species, cf. figure 4.4(b), this simply corresponds to the combined grafting density of all chains of this species. A geometric understanding of this constraint can be obtained similarly to simple star-copolymers. Consider the chains grafted to a certain surface patch dS of the interface. On the one hand, these would be chains of a species of an outer brush, say A, and chains belonging to one of the polymeric arms of species X that form the cores on the other hand. Due to the constraint of equal grafting densities, the volume $V_{A;dS}$, occupied by chains of species A grafted to the surface patch must be in fixed relation to the volume $V_{X;dS}$, occupied by chains of species X emerging from the same surface patch. This relation is given by the volume fraction of both species. In our case we have[1] $\frac{1-\phi}{\phi} = \frac{V_{A;dS}}{V_{X;dS}}$. As before, the precise shape of the regions occupied by the brushes attached to the surface patch dS depend on the (possibly curved) polymeric paths and vice versa, rendering their determination arduous. As a result, the distances $z(\vec{r})$ between a volume element and its corresponding grafting point at the interface can not be evaluated by just looking at the shortest distance between those points because this would in general violate the grafting density constraint. In fact, a precise determination of the polymeric path distances would lead to a more elaborate analysis [42].
Consequently, an accurate SST analysis is futile for most of the complex morphologies presented in chapter 5 and we will stick with the simple evaluation of $z(\vec{r})$ as the shortest distance to the next interface enabling us to get some insight into the driving mechanism of self-assembly albeit not accounting for all conditions. Furthermore, the described copolymer architectures can be treated even more rigorously with the numerical SCFT method which, as we will show, confirms the predictions deducible from (4.7). Therefore, we will focus an simple geometrical arguments obtained from the SST and use the full SCFT for a quantitative analysis.

As before, the extended core is used to pronounce a structure's packing frustration. This time, we did not fix a value for the unit cell size ξ, but allowed the system to adopt a value that minimizes its free energy. By introducing additional interfaces for the core region, however, we increased the interfacial free energy contribution which means that the structure will choose a bigger ξ, cf. (D.1). The important point is that these additional interfaces only depend on the arrangement of branch lines since they are essentially the bounding surface of a dilated version of them. This means that we increase the size of the unit cell independent of the original interfacial areas between species A, B and C. The higher values of ξ then will, by virtue of (D.1), increase the stretching free energies and therefore the effects of packing frustration.

While the two SST expressions (4.4) and (4.7) are different in detail, they have the same effects in terms of emphasizing the importance of packing frustration which translates to the need of closely packing the branch lines within a mesophase. To see this, and to motivate a parameter which quantifies the packing frustration of different branch line arrangements, we look at the limit in which the terms associated with the pure branch line geometry are much greater than the energy contributions due to the interfaces between the A, B and C domains. In (4.4) this is easily done by setting $\tilde{h} \to 0$ and just looking at the second part of the expression which will henceforth be expressed as ${}^{L}/_{V} \left\langle z^2 \right\rangle_{ABC}$. $\left\langle z^2 \right\rangle_{ABC}$ denotes the spatial average of $z^2(\vec{r})$ with respect to the volume V_{ABC}.

Looking at (4.7), we assume that $\sqrt{\frac{\chi_X}{\chi}} A_X \gg A_{ABC}$ and that the stretching contribution

[1] Note that we have considered a single arm of the core (species X) being attached to the surface patch dS for this formula.

of chains of species X is negligible ($f/f_X \to 0$). This leads to $\frac{F}{nk_BT} \propto {}^{A_X^2}/_{V^2} \left\langle z^2 \right\rangle_{ABC}$.

For simplicity, let us assume that the cores form cylindrical domains of total branch line length L with equal radii R everywhere, hence $A_X = 2\pi RL$. Using this and linking R and L to the volume of the core domain, $\pi R^2 L = \phi V$, we end up with

$$\frac{F}{nk_BT} \propto \frac{L}{V} \left\langle z^2 \right\rangle_{ABC} . \tag{4.8}$$

As before, we omitted factors that do not depend on the geometry of the structure. Both concepts, bonds between adjacent cores and extended cores, have the same effect of increasing the importance of packing frustration, quantified by (4.8). The only difference is that by assigning a volume to the core domain the branch lines become dilated thereby restricting the volume average $\langle ... \rangle_{ABC}$ to the space not occupied by the cores.

Chapter 5

Geometric analysis of tricontinuous and columnar mesophases

This chapter gives an overview of possible candidate geometries for triblock star-copolymer self-assembly. The main focus is directed to tricontinuous structures where each of the three polymeric species forms a continuous, triply-periodic network-domain. Furthermore, we present the columnar honeycomb structure, observed in melts of simple triblock star-copolymers, and two additional columnar morphologies which will become relevant upon considering architectural changes for the star-copolymers.
We depict structures that divide space into compartments such that all compartments are congruent and filled by a particular polymeric species (one particular color in the images). Furthermore, the volume of the compartment(s) associated with a particular species has to be equal for all three polymeric components and neighboring compartments must comprise distinct species. A necessary property of all candidate morphologies is the presence of one-dimensional regions in space where three different domains meet. We refer to them as *triple lines*. The covalent bonds in the molecular center of simple star-copolymers must then be placed on these lines. However, in principle there might be such triple lines, which are *not* decorated by molecular centers, but rather have the free ends of distinct chains meeting at them. An example will be given by the *alternative honeycomb* structure. To be precise, we denote the triple lines that also represent the locations of the molecular centers as *branch lines*, indicating the branching of three polymer chains grafted to the same bond at these lines. In contrast to columnar structures, tricontinuous structures do not exhibit multiple compartments of the same species but rather form a single continuous network domain for each polymeric component.

In principle, there is an infinite amount of possible (tricontinuous) structures which obey the topological conditions posed by the star-copolymer architecture. Therefore, we only focus on a handful of structures which have been constructed based on geometrical notions and which have furthermore proven themselves to be suitable candidates for the specific task of self-assembling in systems of star-copolymers. An initial identification of some suitable tricontinuous morphologies was achieved in [37] where certain (purely) geometric notions led to an analysis which estimated the possibility of their formation in systems of three-arm star-shaped molecules. Here, we adopt some of the presented geometries and partly gener-

alize their structure such that they become suitable for mesophases in copolymer melts.
The nomenclature for tricontinuous structures is based on [65]. Let us consider the $3etc(193)$ structure as an example. This morphology was introduced in section 3.4, cf. figure 3.8. The name of such tricontinuous structures always starts with the cipher 3, indicating that the structure can be described by three labyrinthine domains that are identical with regard to their shapes. These domains, or channels, can be described by network graphs which run through the centers of the channels and are labeled according to the reticular chemistry structure resource database [65]. In the case of the $3etc(193)$, these would be so-called *etc* nets. Lastly, we specify the number of the space group, which defines the symmetry of a structure, in parentheses. To be more precise, we have to decide if we treat the individual network-domains as symmetrically distinct or not. If they are regarded to be symmetrically distinct, this means that we do not allow symmetry operations which map a domain onto one of the others. In the case of the $3etc(193)$ on the other hand, all network channels correspond to the pore space and can therefore, for physical reasons, be treated as symmetrically equivalent, allowing symmetry operations which interchange them. This results in the space group , $P\frac{6_3}{m}cm$ with number 193 as given by [23]. For another example of this nomenclature, consider the already discussed bicontinuous Gyroid structure in figure 3.7, which consists of *two* identical, so-called *srs* networks with symmetry group $Ia\bar{3}d$, i.e. number 230, when treating the domains as symmetrically equivalent. Hence the name for this Gyroid, as it forms in diblock copolymer melts, would be $2srs(230)$. However, from here on we shall consider all domains to be symmetrically distinct because we assume that they are filled by different chemical species. In the case of the three-colored analog to the $3etc(193)$ structure, cf. figure 3.8, we would have a reduced symmetry ($P\bar{6}m2$, number 187), which results in the name $3etc(187)$.
The two further columnar candidates where identified based on geometric notions which were discussed in detail in the last chapter and their names simply stem from the effort to adequately describe their appearance.

The construction of the models for all structures presented here starts with an initial configuration of interfaces within a unit cell which separate the different compartments from each other. For the columnar structure this construction is obvious and can be performed by hand. We used the powerful software *Houdini* (www.sidefx.com) to construct, manipulate and visualize the three-dimensional geometric data of all structures. For the case of tricontinuous structures, we start by specifying the spatial arrangement of the three network graphs which describe the morphology. A simple Voronoi construction for the vertices of this graph yields interfaces that form a cell around each vertex. We exclude interfaces which are intersected by an edge of the network to achieve a (polygonal) representation of the interfaces that separate the three network domains. In the next step, we used the *surface evolver* software [7] to refine these interfaces and relax them to their minimal surface area configuration while keeping the topology of the domains unchanged. This minimal surface version of the interfaces is a useful approximation for the final configuration since we are confronted with interfacial tensions for all interfaces in our system, cf. section 2.2.
A simple self-written program allows us to obtain the triple lines (i.e. the branch lines in most cases) within the structure by identifying all edges with three surface patches (i.e. polygons) attached to them. By inserting cylinders around the branch lines we can specify a dilated version of these lines which serve as the initial guess for the region that is occupied by the extended molecular cores where necessary. These (dilated) branch lines will be shown in yellow in the following images, while the surfaces are colored red green and blue such that all surface patches of a given color are facing the same network domain. The unit cell of

each structure is framed. Besides for purposes of visualization, these initial configurations are used for our calculations. On the one hand, we use them to evaluate geometric attributes which are based on the SST and were introduced in chapter 4. On the other hand, we also use them in chapter 6 to obtain the initial configurations for the density fields which enter the spectral method to numerically solve the self-consistent equations, cf. section 2.3.

We believe that the illustration of various candidate morphologies is useful because it provides the reader with certain visual images for which we can employ the concepts that have been developed based on the SST in the last chapter. Moreover, this chapter provides a summary of suitable candidate structures and allows us to compare them with each other. After giving a brief overview of each morphology we estimate their relevance for the self-assembly process by assessing their geometry based on two measures that have been developed in the last chapter. These measures stem from expression (4.4) and quantify the energetic contribution due to the interface configuration, $A/\sqrt{LV}$, and the degree of packing frustration which can be mainly attributed to the arrangement of branch lines, $L/V \left\langle z^2 \right\rangle_{ABC}$. Both measures are independent of the precise choice of the unit cell (and independent of its length scale ξ), as must be the case. We note that the precise evaluation of $L/V \left\langle z^2 \right\rangle_{ABC}$ depends on the actual coarse-grained polymer trajectories within the mesophase because these will determine how the polymeric path distances, $z(\vec{r})$, are calculated, cf. section 2.2. The polymer paths in turn depend on the interface configuration since polymer chains of a particular species are confined to their respective domain. Instead of performing an accurate and therefore highly computational treatment we simply evaluate both geometric measures independently.
This means that we approximate the interfaces in the structure by their minimal surface versions and disregard possible deformations due to packing frustration effects. For the calculation of the packing frustration term we neglect the presence of interfaces and simply evaluate the polymeric path distance $z(\vec{r})$ as the shortest distance between the volume element at position $\vec{r}$ and the next branch line.
The calculation of the interfacial area A, the volume V, and the lengths of branch lines L within a unit cell can be easily achieved numerically by utilizing the aforementioned polygonal representation of the structure. The integrals involved in $\left\langle z^2 \right\rangle_{ABC}$ are obtained by a voxelization of the unit cells volume followed by calculating the distances between each voxel and the next branch line.

5.1 Columnar candidate morphologies

We start by presenting columnar candidate morphologies where an analytical calculation of their geometric properties and free energies is feasible. An accurate treatment of these columnar structures in the context of the SST is possible due to their symmetries. Specifically, the coarse-grained polymer paths must extend radially from the molecular centers on straight paths. This is also true after incorporating an extended core. To facilitate a concrete calculation for triblock star-copolymers with an extended core that accounts for different volume fractions of the cores, we make the assumptions that the core species forms cylindrical compartments centered around the branch lines. This is generally not the case but should become increasingly accurate for a strong segregation strength of the core species X with the other species, when compared to the segregation strengths between the other components, i.e. in the limit $\frac{\chi_X}{\chi} \to \infty$. The precise calculations and the resulting expressions for the free energy can be found in appendix E. A comparison between these analytical

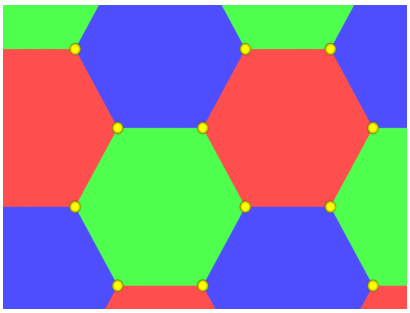

Figure 5.1: Illustration of the usual honeycomb structure observed in triblock star-copolymer melts [55]. Adjacent compartments are occupied by distinct species, represented by the three different color (red, green, blue). The yellow dots indicate the location of branch lines. This particular arrangement of branch lines exhibits high chains stretching (or packing) frustration, due to the relatively large distance between the branch lines and the centers of the hexagonal compartments, which was discussed in the previous chapter. As is the case for all columnar structures, this figure simply shows a cross-section of the actual morphology.

expressions and numerical results will be performed in the next chapter.

Here, we just give a brief introduction of the columnar phases and discuss their relevance for triblock star-copolymer self-asembly based on geometric measures.

5.1.1 The (three-colored) honeycomb structure

The honeycomb structure observed in simple triblock copolymer melts was discussed at length in the previous chapter. Figure 5.1 illustrates its geometry which yields high packing frustration due to its arrangement of branch lines, ${}^{L}\!/_{V} \left\langle z^2 \right\rangle_{ABC} \approx 0.192$. However, the energetic contribution due to interfacial tension is very small, and can be quantified by ${}^{A}\!/_{\sqrt{LV}} \approx 1.32$.

A first idea to improve the packing frustration of the honeycomb structure would be to continuously transform this structure in order to change its branch line arrangement. Figure 5.2 shows this transformation which consists of two continuous steps. First of all, the hexagons of the honeycomb structure are transformed to yield a rectangular arrangement of branch lines. This transformation is characterized by angles $120° \leq \alpha \leq 90°$. Secondly, the resulting structure can be appropriately sheared thereby transforming the rectangular into a triangular arrangement. This step is described by angles $90° \leq \alpha \leq 60°$. With respect to the honeycomb structure, this transformation is not very useful, even after introducing a core. The reason for this is that the volumes of each polymer species associated with the same branch line segment (possibly mediated by the core domain) have to be equal, cf. section 2.2. Hence these volumes are not simply given by the regions closest to the respective branch line (i.e. its Voronoi region) and can not be combined to form quadratic or hexagonal cross sections, as can easily be seen from figure 5.2. This shows the problem of an independent treatment of both geometric measures. We are generally forced to account for the influence of interfaces when evaluating the packing frustration term and vice versa. If we quantify the degree of packing frustration of the pure branch line arrangements shown in figure 5.2 while neglecting the interfaces, we can see that this transformation relieves the packing frustration of the geometry. Figure 5.3 illustrates the degree of packing frustration

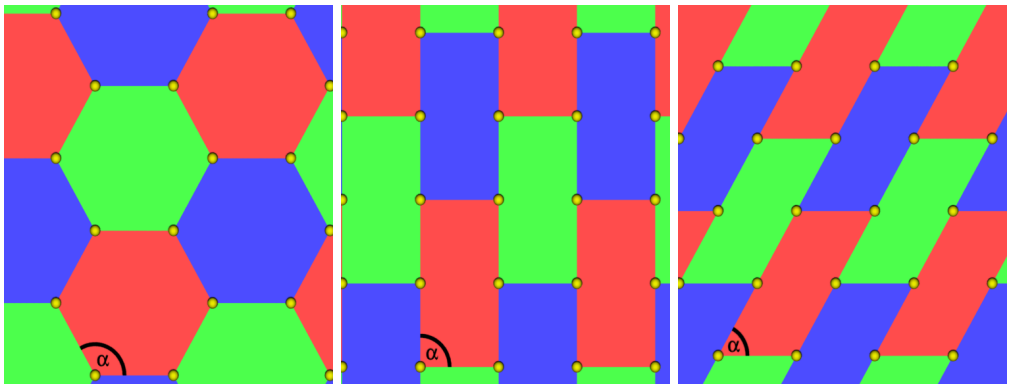

(a) (b) (c)

Figure 5.2: Continuous transformation of parallel branch line arrangements. Starting from the arrangement of the honeycomb structure, shown in (a), the hexagons can be gradually transformed into rectangles, shown in (b). This process can be described by changing the angle α from 120° to 90°. The quadratic branch line arrangement in (b) can be further improved by appropriately shearing the structure leading to an entropically favorable triangular arrangement of branch lines, depicted in (c). This step is characterized by changing α from 90° to 60°. Although this transformation will not reduce the free energy of the honeycomb structure it can be useful for other morphologies with parallel branch lines.

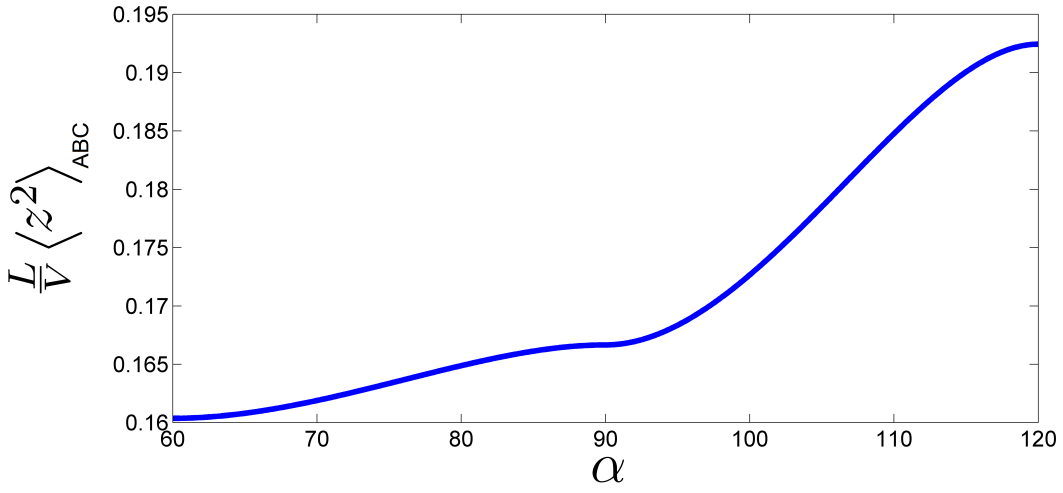

Figure 5.3: Packing frustration, as measured by ${}^{L}/_{V}\,\langle z^2\rangle_{ABC}$, for arrangements of parallel branch lines characterized by the angle α, cf. figure 5.2. The arrangement of branch lines on a quadratic lattice ($\alpha = 90°$) and especially on a triangular lattice ($\alpha = 60°$) yields a significantly lower packing frustration compared to the usual honeycomb structure ($\alpha = 120°$).

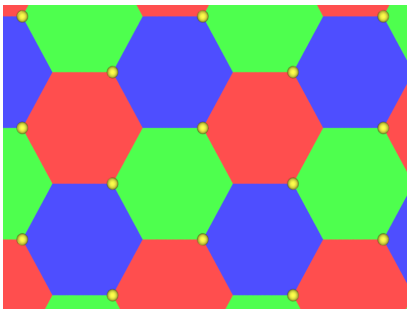

Figure 5.4: The alternative honeycomb structure has the same shape with respect to the red, green and blue domains as the usual honeycomb structure, but yields a different branch line configuration. Here, only every second vertex of the hexagons is decorated with molecular centers (i.e. every second triple line is also a branch lines). This arrangement is preferable in terms of packing frustration. Upon appropriately rescaling the structure such that the volume (or cross-sectional area) associated with a branch line segment of fixed length is the same as for the usual honeycomb, we see that this structure exhibits higher interfacial energies.

for all angles α.
Therefore, this transformation can in principle be useful for tricontinuous structures with parallel branch lines where it can decrease their packing frustration, cf. subsection 5.2.5. In these cases, the *local* imbalance between volumes of different species assigned to the same branch line segment can be relieved by twisting the interfaces along the branch lines thereby balancing these volumes on a larger scale. The local imbalance can then get resolved by choosing the polymer paths accordingly, such that they do not just extend perpendicular to the branch lines but also partly parallel to them. However, this will increase the polymeric path distances and with that also the packing frustration when compared to assumption of perpendicular and straight polymer paths. Note that this local imbalance combined with the need to minimize interface areas will in fact set the $\frac{c}{a}$ ratio for the tricontinuous equilibrium structure to a finite value.

Figure 5.3 shows that aligning branch lines on a triangular lattice ($\alpha = 60°$) results in a significant reduction of packing frustration. Thus we present two columnar structures which adopt this arrangement.

5.1.2 The alternative honeycomb structure

The alternative honeycomb, shown in figure 5.4, employs an arrangement of branch lines on a triangular lattice and therefore minimizes packing frustration. This is confirmed by the measure $\frac{L}{V}\left\langle z^2\right\rangle_{ABC} \approx 0.160$. Its interface configuration, however, yields higher energetic contributions than the usual honeycomb, $\frac{A}{\sqrt{LV}} \approx 1.86$. Note that every second vertex of the hexagonal compartments in this structure is *not* decorated by molecular cores. Hence, all six vertices of the hexagons are triple lines but only every second is a branch line.

One might argue that the interfacial contribution to the free energy should be the same as for the usual honeycomb because of their comparable appearances. This, however, is not the case and can be best illustrated by enforcing that the volume (or in this case cross-

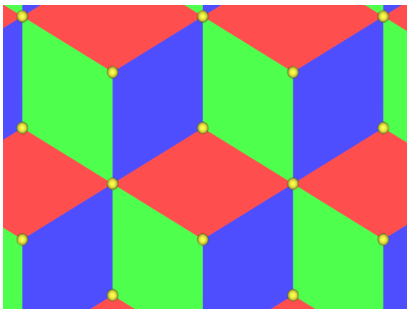

Figure 5.5: The columnar sixfold tiling where every third branch line is surrounded by six instead of the usual three compartments. Like in the alternative honeycomb morphology, the branch lines are aligned on a triangular lattice leading to low packing frustration. The interfacial energy benefits from the fact that the interfaces directly connect adjacent branch lines without forming additional vertices as was the case in the alternative honeycomb structure. However, this direct connection is globally only realizable when allowing for the sixfold connections of interfaces at every third branch line which results in additional interfaces and leads to an overall larger interfacial area.

sectional area) associated with a branch line, i.e. the volume of the Voronoi regions, should be equal in both cases, thus setting V to the same value in both structures, if one assumes a fixed length L. Since only every second vertex of the hexagons is occupied by a branch line in case of the alternative honeycomb morphology, the interfacial area contained in each Voronoi region is larger than for the usual honeycomb. Figure 4.2 depicts these Voronoi regions such that the interfaces within them can be compared.

5.1.3 The sixfold tiling

There is another columnar structure with an arrangement of branch line on a triangular lattice. Figure 5.5 shows this morphology which we call the sixfold tiling due the fact that every third branch lines has not three but six adjoining compartments. This assembly was already suggested as a possible mesophase for triblock star-copolymer self-assembly in [63] but was not recognized for the entropically favorable branch line arrangement. Since this arrangement is the same as for the alternative honeycomb, we obtain the same degree of packing frustration $\frac{L}{V}\left\langle z^2\right\rangle_{ABC} \approx 0.160$. The interfacial contribution on the other hand is larger $\frac{A}{\sqrt{LV}} \approx 2.15$. This is, however, only true for infinitely thin branch lines, i.e. for the self-assembly of simple triblock star-copolymers without a core. Upon introducing an extended core the interfacial areas of the sixfold tiling and the alternative honeycomb change in different ways such that the sixfold tiling will by favored for high enough volume fractions of the core, cf. appendix E.

5.2 Tricontinuous candidate morphologies

This section discusses possible tricontinuous candidate mesophases where each polymeric species forms a single continuous network-like domain rather than multiple columnar compartments. The branch lines in these structures are generally curved and can be aligned arbitrarily to each other. This affords a variety of interesting closed-packed branch line arrangement and thus structures with reduces packing frustration. Still, the branch lines

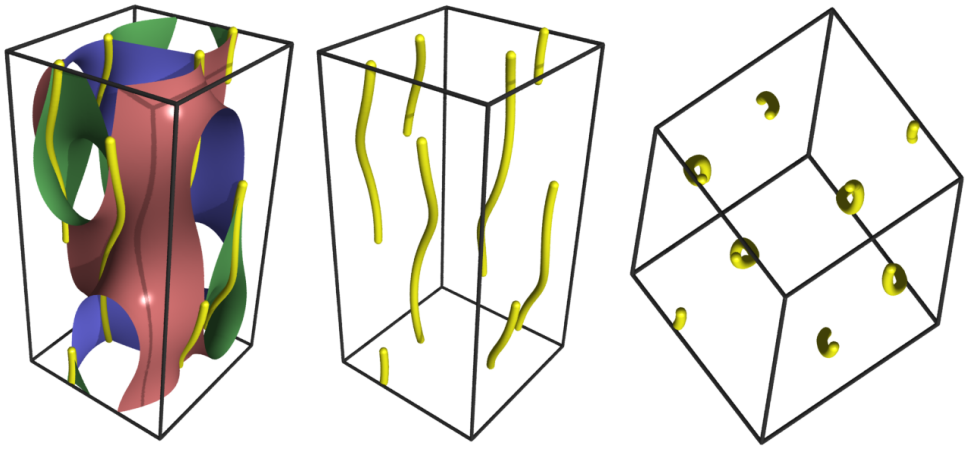

(a) (b) (c)

Figure 5.6: Representation of the $3cds(1)$ morphology. (a) Interfaces and branch lines. (b) Branch lines only. (c) Top view of branch lines, which form helices that are nearly arranged on a quadratic lattice.

could also be aligned parallel to each other, making the transition we examined in figures 5.2 and 5.3 relevant for tricontinuous structure associated with such branch line alignments.

5.2.1 $3cds(1)$

We start by demonstrating a structure with no symmetries, if one considers all domains to be symmetrically different, in figure 5.6. This $3cds(1)$ structure is made of intertwining three *cds* nets and can be described in a tetragonal unit cell with $c/a = 2$. However, as it turns out, it is outclassed by the following structures when it comes to triblock star-copolymer self-assembly. Nevertheless, it provides a first step to achieve a structure that yields only slightly higher interfacial energies compared to the honeycomb, $\frac{A}{\sqrt{LV}} \approx 1.61$, but already exhibits less packing frustration, $\frac{L}{V}\left\langle z^2\right\rangle_{ABC} \approx 0.179$. This due to the fact that the branch lines form helices which are packed on a nearly regular quadratic lattice and hence have less packing frustration than the frustrated arrangement of branch lines in the honeycomb, cf. section 5.1.

5.2.2 $3srs(24)$ and $3dia(24)$

Figure 5.7 present two structures that, if one would treat the different domains as symmetrically equivalent, exhibit cubic symmetry. The first, $3srs(24)$, is chiral and has been introduced as a "Cubic Archimedean Screw" [14] while the second, $3dia(24)$, is achiral. The *srs* nets of the $3srs(24)$ structure have been introduced as the nets describing the channels of the Gyroid, cf. figure 3.7, while the *dia* nets of the $3dia(24)$ structure are the nets describing the well known diamond structure. Both structures are equal in terms of the geometric attributes associated with interface area, $\frac{A}{\sqrt{LV}} \approx 1.78$, and packing frustration, $\frac{L}{V}\left\langle z^2\right\rangle_{ABC} \approx 0.166$. Therefore, the numerical SCFT method shows only marginal differences in the free energies of both mesophases. The similar packing frustration can be ascribed to the fact that both structures adopt the same arrangement of branch lines, which

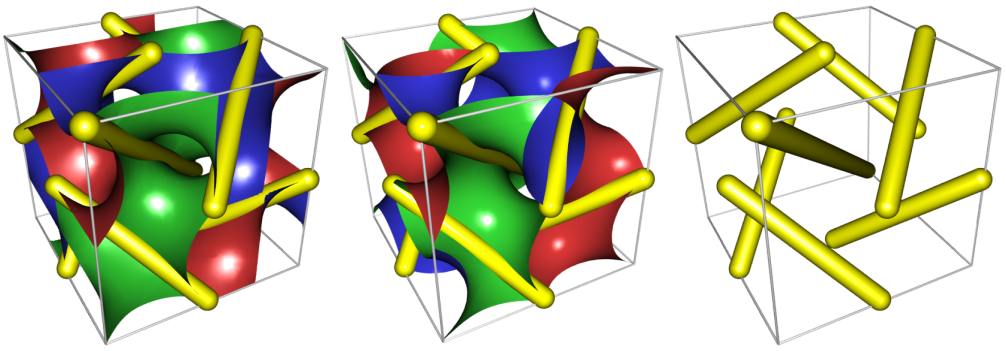

(a) (b) (c)

Figure 5.7: Representation of two tricontinuous morphologies with a cubic unit cell. The uncolored versions of these structures (with symmetrically equivalent domains) has cubic symmetry. (a) Interfaces and branch lines in the $3srs(24)$ structure. (b) Interfaces and branch lines in the $3dia(24)$ structure. (c) Branch lines of both morphologies, following the densest cubic cylinder packing [64].

corresponds to the densest cubic cylinder packing if one would replace the branch lines by cylinders with maximal radius, such that they do not intersect each other [64]. This close-packing of branch lines (or rather of cylinders which follow these lines) is directly linked to the comparatively low degree of packing frustration in these structures.

5.2.3 $3qtz(145)$ family

So far we have shown individual candidates. In figure 5.8, we introduce a morphology with a single free parameter, in this case the unit cell's c/a ratio, which therefore creates a whole family of structures. Like the $3srs(24)$, the structures in this family are also chiral. For a couple of c/a ratio, we obtain domains which are characterized by regular (i.e. undistorted) nets. For $\frac{c}{a} \approx 0.7049$ the domains can be characterized by three *eta* nets, for $\frac{c}{a} = \frac{3}{2\sqrt{2}} \approx 1.0607$ the channels are described by three regular *qtz* nets and for $\frac{c}{a} = \frac{3\sqrt{3}}{2} \approx 2.5981$ we can describe them by *bto* nets. However, for most relevant $\frac{c}{a}$ ratios, the structure is best described by the *qtz* net, hence the name for this family. The branch lines of this structure are more or less curved, depending on the $\frac{c}{a}$ ratio. In all cases, however, the branch lines reside in planes. These planes are parallel to the plane spanned by the crystallographic lattice vectors $\vec{a}$ and $\vec{b}$ and three planes are equidistantly stacked within each unit cell, cf. figure 5.8(b). Furthermore, the lines in each plane are aligned parallel and with fixed distance to their respective neighbors. The branch lines in two adjacent planes, however, are twisted by an angle of 120°. For appropriate $\frac{c}{a}$ ratios this yields a good configuration in terms of packing frustration, as figure 5.9(a) shows. Additionally, figure 5.9(b) indicates that the interfacial energies are also competitive with those of other tricontinuous structures.

5.2.4 $3ths(109)$ family

Next, we introduce a family of tricontinuous structures with branch lines decorating a quadratic lattice. Figure 5.10 shows this $3ths(109)$ family which can be described in a tetragonal unit cell. The free parameter characterizing this family is the c/a ratio of the unit cell. For $c/a = \sqrt{2} \approx 1.41$ the network domains can be described by regular *dia* nets

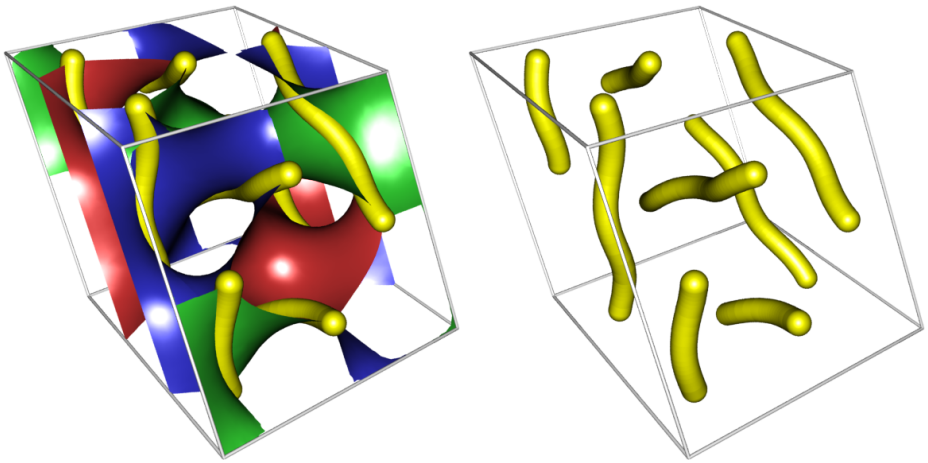

(a) (b)

Figure 5.8: Representation of the $3qtz(145)$ family. (a) Interfaces and branch lines in the $3qtz(145)$ structure, shown here with $\frac{c}{a} = \frac{3}{2\sqrt{2}}$. The crystallographic lattice vector $\vec{c}$ is perpendicular to all planes of branch lines. (b) Planes of parallel branch lines are stacked on top of each other with a twist of 120°.

(the nets describing the diamond structure), and for $c/a = 2\sqrt{3} \approx 3.46$ they correspond to so-called *ths* nets, which we adopt to describe this family.
Besides the reduced packing frustration of the quadratic lattice this family also benefits from low interfacial terms, especially for large c/a ratios. Figure 5.11 incorporates a comparison between these terms (described by the curves with $\alpha = 90°$) for a wide range of c/a ratios. It can be seen that the interfacial term favors a large c/a ratio. The changes in packing frustration arise due to the fact that the branch lines form helices rather than straight lines except for $c/a \approx \sqrt{2}$ or for very large c/a ratios. Note that our treatment does not account for a precise calculation of the packing frustration effects due to the simplified assumption of straight polymer paths. The error we make by employing this assumptions gets worse for larger c/a ratios due to the fact that the interfaces will impose increasing deviations to the polymer paths and therefore higher packing frustrations. Therefore, the self-assembly chooses a preferred c/a ratio which is set by the balance between decreasing interfacial energies for larger c/a ratios on the one hand and increasing packing frustration on the other.

5.2.5 $3ths(5)$ family

Besides the possibility to change the c/a ratio in the $3ths(109)$ family, we can also induce changes to these morphologies by shearing the unit cell, i.e. by changing the angle α between the crystallographic $\vec{a}$ and $\vec{b}$ vectors. The idea behind this transformation is the transition from the quadratic arrangement of branch lines to the triangular one, cf. figure 5.2. This will decrease the packing frustration but only marginally increase the interfacial energies, as is shown in figure 5.11. Note that the errors we make by the assumption of straight polymer paths are even worse than in the case of the $3ths(5)$ family, especially for large c/a ratios. This means that figure 5.11 can only give a qualitative description of the mechanisms behind the self-assembly process. Since the $3ths(109)$ family looses symmetries during this

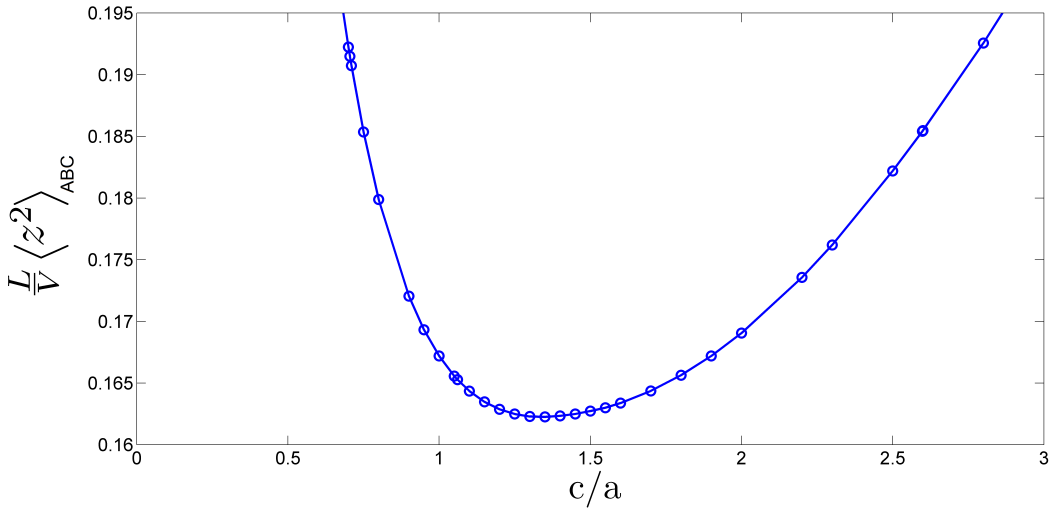

(a)

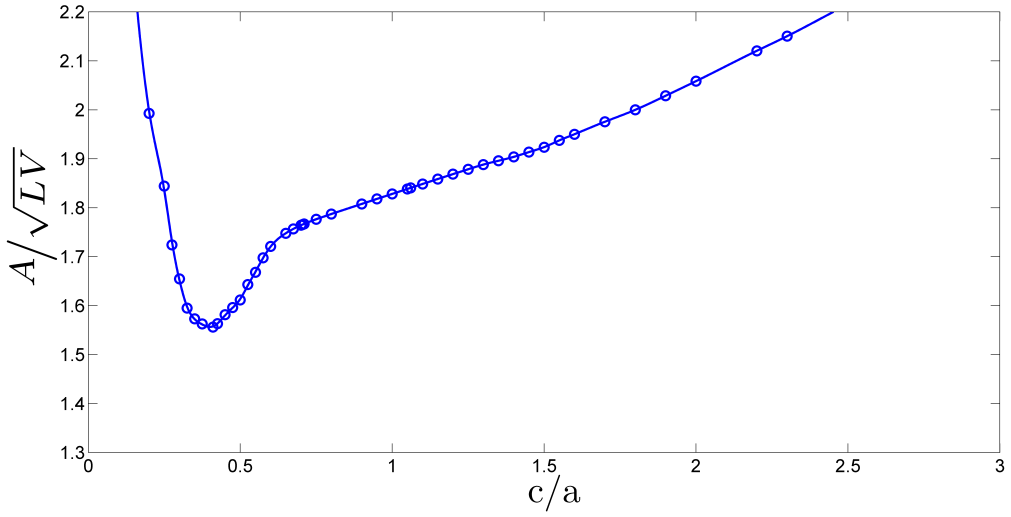

(b)

Figure 5.9: Geometric attributes of the $3qtz(145)$ family for a range of relevant c/a ratios. Open circles indicate data points, lines serve as a guide to the eye. (a) Packing frustration associated with the branch line arrangements. (b) Energetic contributions due to the interface configuration.

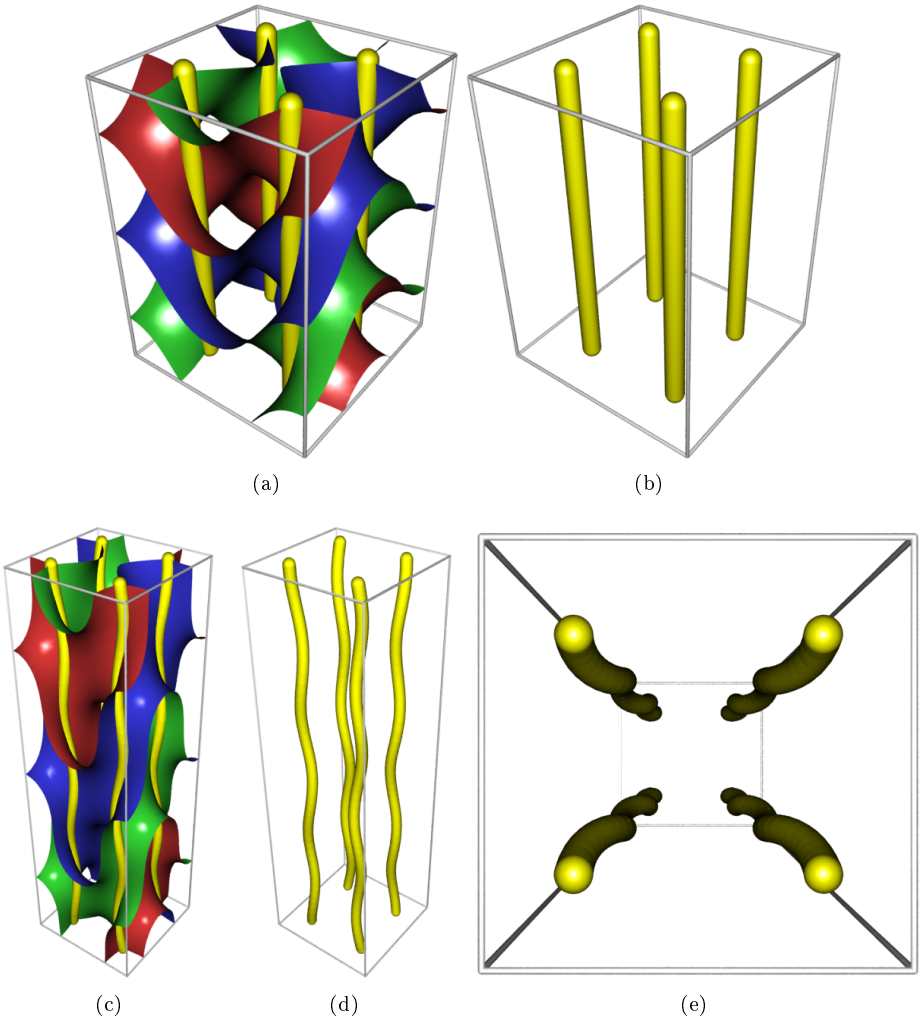

Figure 5.10: Representation of the $3ths(109)$ family. (a) Interfaces and branch lines for $c/a = \sqrt{2}$, whereby the crystallographic $\vec{c}$ vector points upwards. (b) Branch lines for $c/a = \sqrt{2}$. These are straight lines that are arranged on a perfect quadratic lattice. (c) Interfaces and branch lines for $c/a = 2\sqrt{3}$. (d) Branch lines only for $c/a = 2\sqrt{3}$. (e) Top view of branch lines for $c/a = 2\sqrt{3}$, which form helices arranged on a quadratic lattice.

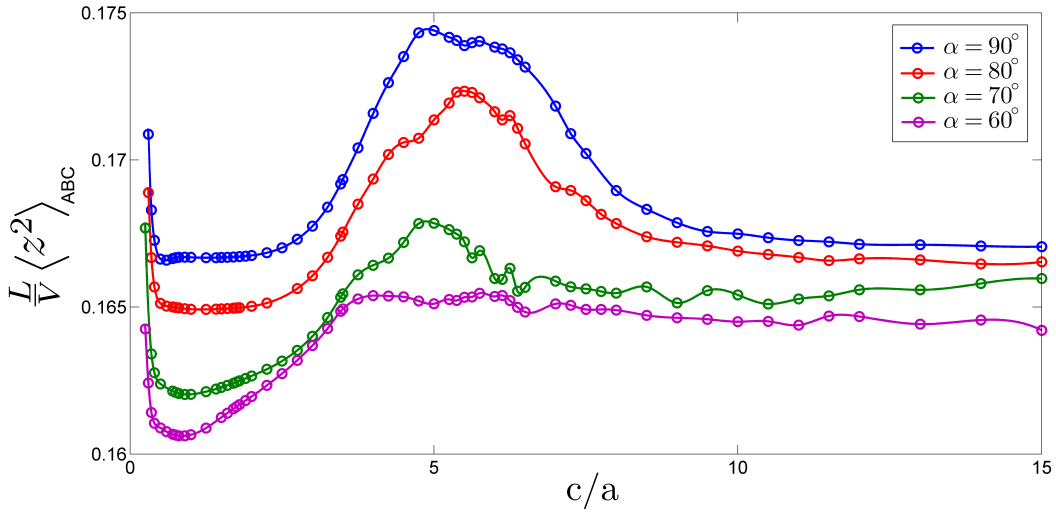

(a)

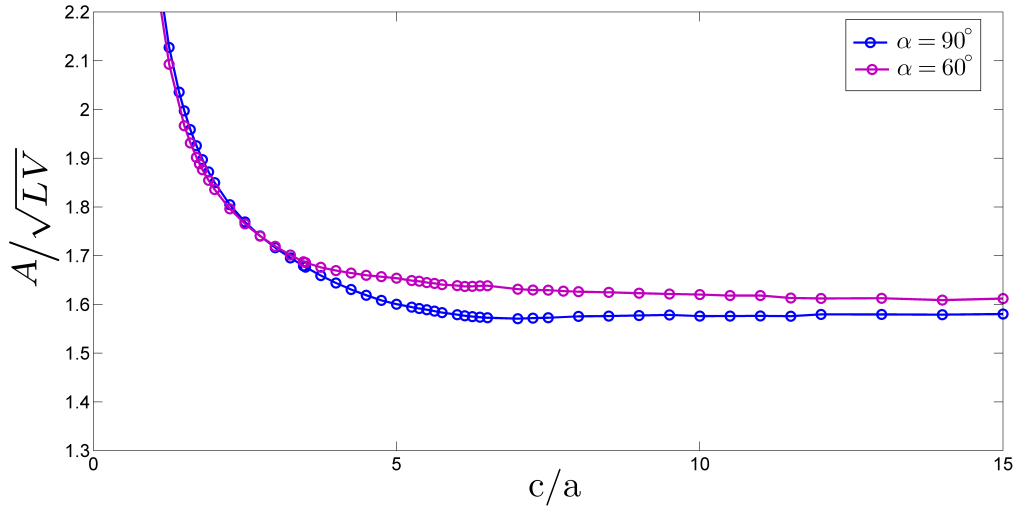

(b)

Figure 5.11: Geometric attributes of the $3ths(5)$ family for a range of relevant c/a ratios and some angles α. $\alpha = 90^\circ$ describes branch lines arranged on a quadratic lattice and thus corresponds to the $3ths(109)$ family, while $\alpha = 60^\circ$ means an arrangement that follows a triangular lattice, cf. figure 5.2. However, the actual branch lines might not be straight but rather undulated or curled, cf. figures 5.10(e) and 5.12(f). Open circles indicate data points, lines serve as a guide to the eye. (a) Packing frustration associated with the branch line arrangements. (b) Energetic contributions due to the interface configuration.

process we end up with the $3ths(5)$ family which has, besides its translational symmetries, only a single two-fold symmetry ration left. As it turns out, this transformation can further decrease the free energy of the $3ths(109)$ family and the more general morphologies of the $3ths(5)$ family constitute the tricontinuous structures best suited for self-assembly of triblock star-copolymers with an extended core. Figure 5.12 shows a particular member of this family which is characterized by $\alpha = 70°$ and $c/a = 4.5$ and provides a suitable candidate for most parameters of the triblock star-copolymer system. However, all values for α and c/a ratios are in principle possible and their optimal values depend on the parameters of the system.

5.3 Comparison of the candidate morphologies

We give a brief summary that compares the candidate morphologies that have been introduced in this chapter. Table 5.1 lists the most suitable candidates and their respective geometric measures for their interface configurations and their degree of packing frustration.

We see that the honeycomb represents the best structure in terms of its interface configuration but shows the a high degree of packing frustration when compared to the other candidate geometries. The triangular arrangement of branch lines, adopted by the two other columnar structure, the alternative honeycomb and the sixfold tiling, on other hand provides the lowest degree of packing frustration. However, the associated columnar structures exhibit high interfacial energies. The tricontinuous structures are intermediate with respect to both contributions and it can be expected that the region of their thermodynamic stability is located between those of the honeycomb and the other columnar structures when increasing the importance of packing frustration. This will be demonstrated in the next chapter, where we also identify a member of the $3ths(5)$ family, with parameters $c/a \approx 4.5$ and $\alpha \approx 70°$, to be a stable phase in melts of triblock star-copolymers with an extended core. In fact, we already see that this structure turns out to be highly competitive based on the geometric discussion of this chapter, cf. table 5.1.

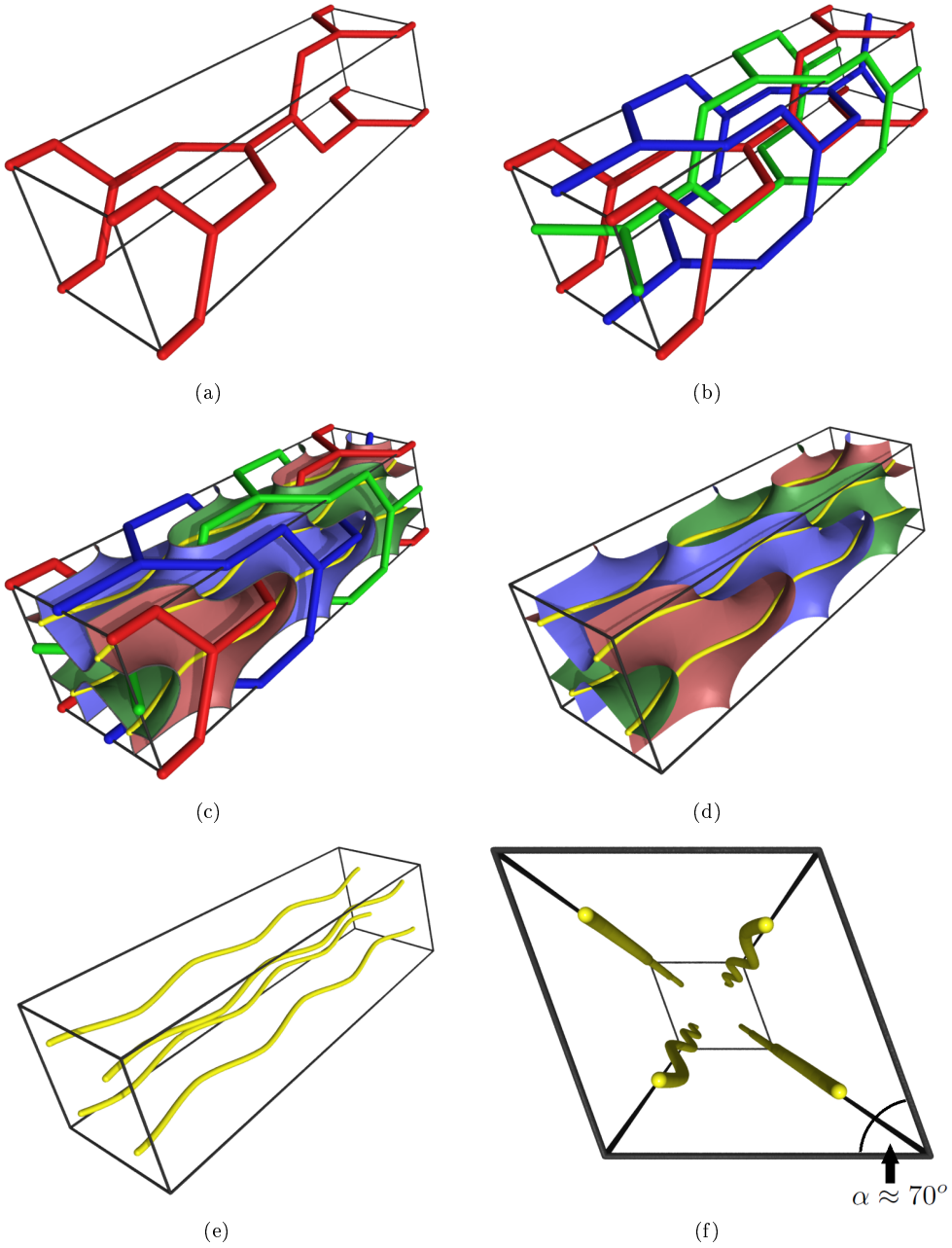

Figure 5.12: Representation of the 3*ths*(5) family using the member characterized by the angle $\alpha = 70°$ and $c/a = 4.5$. The optimal configuration, however, depends on the system. The demonstrated values have been used in the calculations and provide a suitable guess for most systems. The lattice vector $\vec{c}$ corresponds to the longest side of the unit cell and the angle α is indicated in (f). (a) A single distorted *ths* network, characterizing the individual labyrinthine domains. (b) Three interwoven *ths* nets characterize this particular morphology. (c) Complete picture of the 3*ths*(5) structure, including the three nets, interfaces between distinct domains, and branch lines. (d) Interfaces and branch lines. (e) Branch lines only. (f) Top view of branch lines which form undulated lines following a two-dimensional rhombic lattice.

Structure	Symmetry	c/a	α	$A/\sqrt{LV}$	$L/V \left\langle z^2 \right\rangle_{ABC}$
Honeycomb	$p3m1$			1.32	0.192
$3cds(1)$	$P1$			1.61	0.179
$3ths(109)$	$I4_1md$	$\sqrt{2}$		2.04	0.167
$3ths(109)$	$I4_1md$	$2\sqrt{3}$		1.68	0.169
$3ths(109)$	$I4_1md$	4.5		1.62	0.174
$3ths(109)$	$I4_1md$	8		1.58	0.169
$3ths(5)$	$I121$	$2\sqrt{3}$	70	1.68	0.165
$3ths(5)$	$I121$	4.5	70	1.63	0.167
$3ths(5)$	$I121$	8	70	1.59	0.166
$3ths(5)$	$I121$	$2\sqrt{3}$	60	1.69	0.165
$3ths(5)$	$I121$	4.5	60	1.66	0.165
$3ths(5)$	$I121$	8	60	1.63	0.165
$3srs(24)$	$I2_12_12_1$			1.78	0.166
$3qtz(145)$	$P3_2$	0.45		1.58	0.268
$3qtz(145)$	$P3_2$	0.7049		1.77	0.192
$3qtz(145)$	$P3_2$	1.0607		1.84	0.165
$3qtz(145)$	$P3_2$	1.3		1.89	0.162
$3qtz(145)$	$P3_2$	2.5		2.22	0.182
Alternative honeycomb	$p3$			1.86	0.160
Sixfold tiling	$p2$			2.15	0.160

Table 5.1: Summary of suitable candidate mesophase geometries for ABC star-copolymer self-assembly, including the respective measures for their interface configuration, $A/\sqrt{LV}$, and their packing frustration, $\frac{L}{V}\left\langle z^2 \right\rangle_{ABC}$ (rounded to significant digits). Each structure is labeled following the notation of [65], with the space group number in parentheses. Where applicable, structural parameters (c/a ratio, angle α of the unit cell) are provided to distinguish different members of a tricontinuous family. Note that the data for $\left\langle z^2 \right\rangle_{ABC}$ is obtained by assuming straight polymer paths to the next branch line. Therefore, deviations between the actual packing frustration and these values are expected, especially for members of the $3ths(5)$ family with large $\frac{c}{a}$ ratios. The data shows the general tendency that an increase in the interface term $A/\sqrt{LV}$ is accompanied by a lower stretching term $L/V \left\langle z^2 \right\rangle_{ABC}$, at least for the most suitable candidates.

Chapter 6

Phase diagram for triblock star-copolymers with an extended core

In this chapter we present the numerical results for determining the equilibrium mesophase in triblock star-copolymer melts via the full SCFT. We provide profound evidence that the introduction of a polymeric core to the molecular architecture can stabilize the formation of novel phases including a tricontinuous triply-periodic phase composed of three intertwined networks. This states the final proposition of this thesis and merges the geometric considerations of the last chapters.

We employ the spectral method [53] with the Anderson mixing scheme [49] to numerically solve the self-consistent field equations, cf. section 2.3. The algorithms have been implemented by ourselves, following the descriptions found in literature [53, 47, 78, 22, 48, 49, 41] that have been tailored to our needs as presented in chapter 2. We tested our program on a few simpler molecular architectures, e.g. diblock copolymers as demonstrated in section 3.4, before turning our attention to the molecular architectures of triblock star-copolymers, and specifically to those with an extended core made of a fourth polymeric species with (possibly) multiple arms of species A, B and C attached to it, cf. figure 4.4. After approximately identifying the regions of stability of tricontinuous phases for various architectures and molecular parameters, we tried to ascertain the phase boundaries thus enabling us to construct phase diagrams for different architectures. These phase diagrams describe a given system in terms of two parameters. Firstly, this is the volume fraction of the core, denoted ϕ, which is linked to the surface area of the interfaces between the core species X and the rest of the system. Secondly, we vary the interaction strength between the core and the rest of the system, χ_X, while keeping the interaction strength among the other species, χ, fixed. More precisely, we plot the ratio $\frac{\chi_X}{\chi}$ to ensure a consistent comparison between different systems.
First of all, it has to be noted that all of the presented columnar and tricontinuous structures will supersede the usual honeycomb structure in terms of their stability if one increases the volume fraction ϕ and the ratio $\frac{\chi_X}{\chi}$ sufficiently, in agreement with our notion of an increased emphasis on packing frustration. However, we still have to identify the equilibrium solution for a given set of molecular parameters among these candidate morphologies. As it turns out, the equilibrium structure will either be given by one of the new columnar phases or by

a member of the tricontinuous $3ths(5)$ family. We found no exception to this rule for all investigated systems.
Due to the low symmetry of this structure we run into the problem that many basis functions are needed to accurately calculate its free energy. Therefore, we used $\#BF = 7000$ basis functions (cf. section 2.3) for this structure which implies a high computational demand[1]. Also, performing a minimization with respect to the precise shape of the unit cell (i.e. its c/a ratio and its angle α) is not viable for all sets of parameters and we hence use a configuration, namely $c/a = 4.5$ and $\alpha = 70°$, that is a reasonable configuration for all system parameters of interest. The actual free energy of this tricontinuous family might hence still be marginally lowered by tuning these values.
The columnar morphologies can be accurately calculated with a couple of hundreds of basis function putting no significant limits to the their computational demand.
This means that we have to restrict ourselves to exploratory studies to identify the stability of certain tricontinuous morphologies and that we can only consider a few system more thoroughly by constructing their phase diagrams.

An obvious starting point for our investigations is to consider the architecture in figure 4.4(a), being a simple star-shaped triblock system extended by a polymeric core which forms a star-shaped molecular object of species X that has a single chain of species A, B and C attached to it and assumes equal statistical segment lengths for all species. We identified a narrow window of stability of the tricontinuous $3ths(5)$ morphology for this system which is bounded by the usual honeycomb for small and weakly segregated cores and by the sixfold tiling for large cores, provided that the segregation between species A, B and C is strong enough to already induce microphase separation without an extended core. This window of stability can, however, by further broadened by attaching multiple chains of each species A, B and C to the polymeric core or by using stiffer polymers of species X. The calculations indicate that increasing both, the number of chains of the outer species (A, B and C) and the statistical segment length of the core, a_X, will result in qualitatively the same behavior as in the previous case, but with an increased window of stability for the tricontinuous phase. This corresponds well to the concepts of section 4.2 where both effects can be uniformly described by lowering the ratio $\frac{f}{f_X}$ in (4.7) and hence decreasing the importance of chain stretching effects within the core. This aids our geometric view of highlighting the packing frustration effects of the *outer* species while treating the core domain as a rigid (cylindrical) object.

To find a balance between stressing the effects of packing frustration while keeping the molecular architecture as simple as possible, we decided to concentrate on the case of triblock star-copolymers depicted in figure 4.4(b), where two instead of just one chain of each outer species is attached to the polymeric core. The statistical segment lengths are still the same for all species A, B, C and X.
Let us first consider a system with $\chi N = 40$ which implies a moderately segregated melt that forms the usual honeycomb structure in absence of a core. We present the phase diagram of this system in figure 6.1. For high enough core volumes ϕ and a high enough interfacial tension of the core domain, measured by the ratio $\frac{\chi_X}{\chi}$, the honeycomb destabi-

[1] Note that the first implementation of the spectral method in 1994 used up to $\#BF = 400$ basis functions for the most complex morphology, which was the Gyroid in diblock copolymer melts [53]. Since the complexity of each iteration of the spectral method is of the order $\mathcal{O}((\#BF)^3)$, we would have over 5000 times longer computation times. Fortunately, the algorithms involved in the spectral method have been, and still are being, optimized, cf. [49]. Nevertheless, a free energy calculation with $\#BF = 7000$, including the minimization with respect to the unit cell size ξ, for a single set of system parameters takes almost two days even with the optimized computing cluster version. Therefore, the accuracy in free energies is still limited by the number of basis functions deterring us from investigating strongly segregated systems.

lizes and the equilibrium structure is given by the tricontinuous $3ths(5)$ morphology. For even higher core volumes the equilibrium morphology is the sixfold tiling, as expected due to its triangular arrangement of branch lines which minimizes packing frustration, as well as its comparatively low interfacial area for high enough volume fractions, cf. appendix E. The tricontinuous structure is intermediate in terms of both packing frustration and interface configuration, cf. section 5.3, and is therefore located between the two columnar phases.
The diagram itself was obtained by calculating the free energies of all competing mesophases for certain parameters of ϕ and $\frac{\chi_X}{\chi}$, indicated by markers in the diagram. Based on a Delaunay triangulation for the evaluated parameter points we can obtain a free energy surface for each candidate morphology by lifting the vertices of the triangulation according to their calculated free energies at the associated parameters. Based on interpolation we can then estimate the phase boundaries within the diagram.
We also checked for the possibility that the cylinder forming core domains in these mesophases might agglomerate to spherical objects since this would further decrease packing frustration, cf. the formation of spherical micelles in diblock copolymer melts at very asymmetric molecular architectures, outlined in chapter 3. However, due to additional interfaces between A, B and C this is not yet favorable for the $\frac{\chi_X}{\chi}$ ratios we investigated.

Figure 6.2 demonstrated a second example of a phase diagram. We consider the same molecular architecture as before and set the segregation strength between species A, B and C to a lower value of $\chi N = 25$. If we do not incorporate a core to the dual-chain triblock star-copolymers, the melt would form a homogeneous disordered state in this case because the segregation strength is too low. However, by adding an extended and well enough segregated core, we can induce microphase separation and a variety of mesophases is found. Just above the onset of microphase separation a narrow region of stability for the usual honeycomb phase can be observed. At marginally higher core volumes we can again stabilize the tricontinuous $3ths(5)$ phase which is stable in a wide parameter region. This time, this phase borders on the alternative honeycomb phase which surrounds the stability region of the $3ths(5)$ structure. For sufficiently high core volumes, we obtain the sixfold tiling pattern as before.

The transition point between the alternative honeycomb and the sixfold tiling is, in the limit of high χ_X/χ ratios, well described by the analytical calculation, see appendix E. Furthermore, we can obtain the volume fractions and segregation ratios for the transitions between the usual honeycomb and the alternative honeycomb and between the alternative honeycomb and the sixfold tiling from the numerical calculation. Figure 6.3 shows the location of these transitions and compares them with the analytical calculations of appendix E. Deviations between the phase boundaries of the numerical SCFT calculations and the analytical predictions can be partially attributed to the discrepancies between the strong segregation theory that was used for the analytical calculations and the weak or moderate segregations that had to be chosen for the numerics. Moreover, we employed the simplified assumption of a cylindrical core in our analytical treatment, whereas the density fields obtained by the spectral methods show that the core domains can become significantly deformed in order to minimize the surface area of the interfaces between species A, B and C at the expense of increasing their own interfacial area. Nevertheless, the SST provides qualitative agreement with the full SCFT which further confirms our geometric notions for the self-assembly process in star-copolymer melts.

We presented the existence of a region of stability for the tricontinuous $3ths(5)$ phase

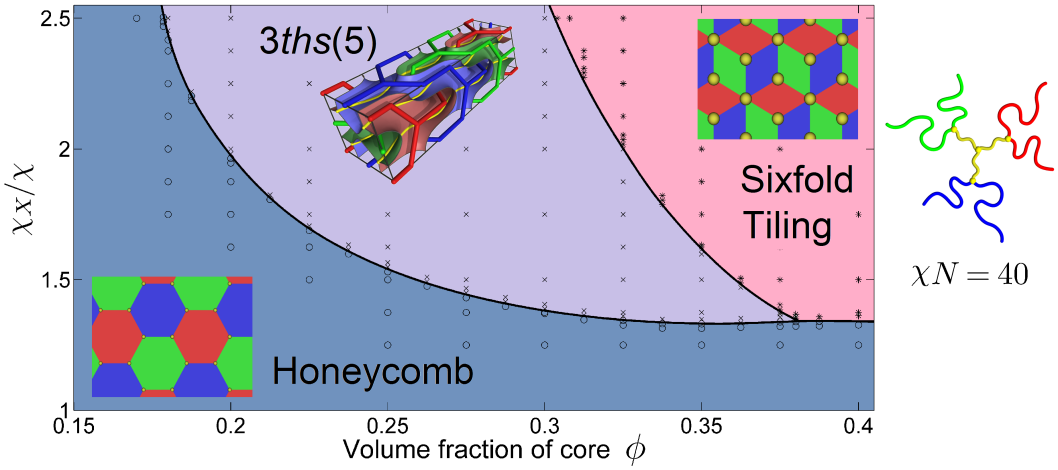

Figure 6.1: Phase diagram for dual-chain triblock star-copolymers with and extended core. The segregation strengths between species A, B and C was set to $\chi N = 40$. The stability of different structures is shown with respect to the volume fraction of the molecular core of species X, denoted ϕ, and the ratio of the segregation strengths, χ_X/χ. Markers indicate data points where the free energy has been calculated for the competing structures. Solid black lines indicate phase boundaries and are based on interpolation of these free energies. The stability regions of the different phases are separated by these lines and are further highlighted by different coloring and differently shaped markers. Moreover, the denotation of each stable phase is given together with an illustration in the respective region of the phase diagram. The molecular architecture of the constituent molecules and the segregation strength between A, B and C are shown to the right of the phase diagram. At $\chi N = 40$ the simple triblock system is moderately segregated and forms the usual honeycomb structure, shown at the bottom left in the phase diagram. For sufficiently pronounced cores, this morphology will be destabilized giving rise to the formation of the triply-periodic $3ths(5)$ structure consisting of three interwoven continuous network-domains. If the volume fraction of the core is further increased, one observes the formation of the sixfold tiling pattern shown at the top right side of the phase diagram.

when an extended and well segregated core is included in the molecular architecture. According to SST calculations, this region can be broadened by changing the molecular architecture such that the stretching contributions of the outer species is further pronounced while keeping the necessity to account for atomistic configurations within the core minimal. Our numerical calculations confirm this idea and the presented phase diagrams are strong evidence that it is possible to form ordered mesophases composed of three continuous network domains in soft-matter systems.

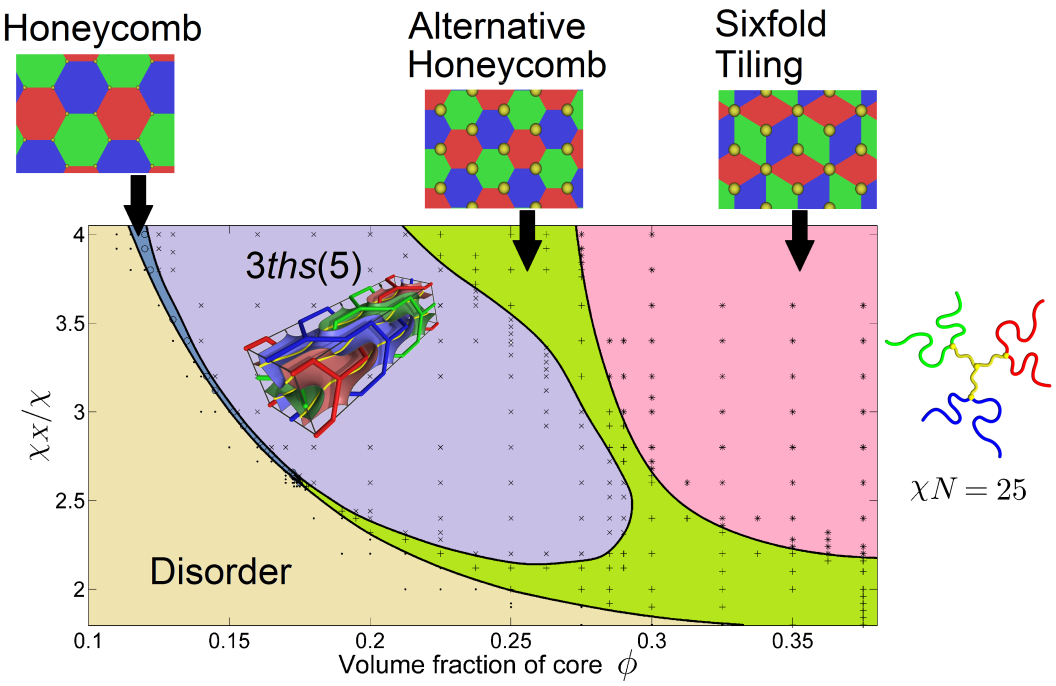

Figure 6.2: Phase diagram for dual-chain triblock star-copolymers with and extended core. The segregation strengths between species A, B and C was chosen to be $\chi N = 25$. The stability of different structures is shown with respect to the volume fraction of the molecular core of species X, denoted ϕ, and the ratio of the segregation strengths, χ_X/χ. Markers indicate data points where the free energy has been calculated for the competing structures. Solid black lines indicate phase boundaries and are based on interpolation of these free energies. The stability regions of the different phases are separated by these lines and are further highlighted by different coloring and differently shaped markers. Moreover, the denotation of each stable phase is given together with an illustration in the respective region of the phase diagram. The molecular architecture of the constituent molecules and the segregation strength between A, B and C are shown to the right of the phase diagram. At $\chi N = 25$ the simple triblock system does not microphase separate at all and the homogeneous disordered phase provides the equilibrium solution of the melt. For sufficiently pronounced cores, we can induce microphase separation, giving rise to the formation of the honeycomb in a very narrow region of stability. Furthermore, we observe the triply-periodic $3ths(5)$ structure consisting of three interwoven continuous network-domains for a wide parameter region. In this case, the $3ths(5)$ structure's region of stability is surrounded by the stability region of the alternative honeycomb morphology. If the volume fraction of the core is further increased, one observes the formation of the sixfold tiling pattern again.

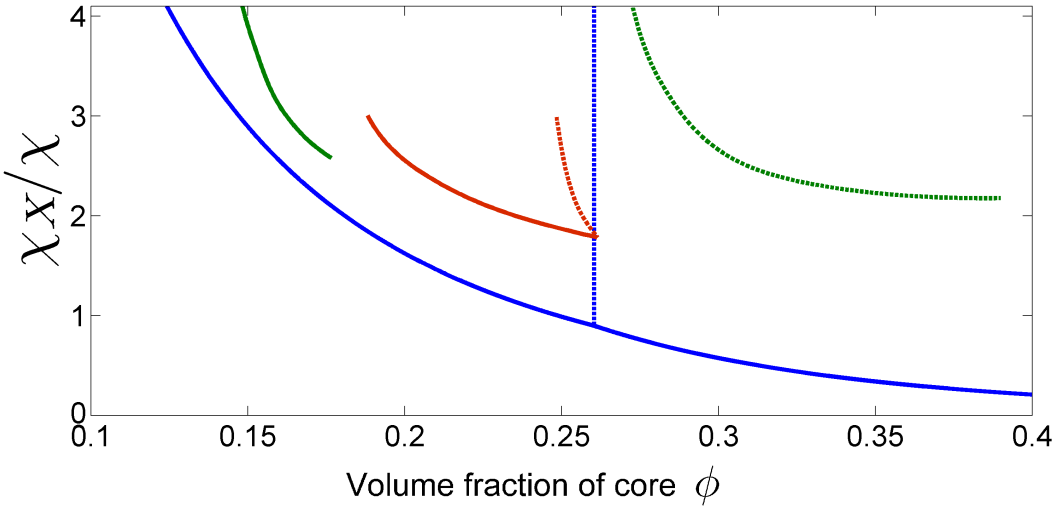

Figure 6.3: Comparison of the phase boundaries between the three columnar structures for melts of dual-chain star-copolymers with extended cores, obtained by different methods. Phase boundaries are given with respect to the volume fraction of the molecular core, ϕ, and the ratio between the segregation strength of the core species X, denoted χ_X, and the segregation strength among the other species A, B and C, labeled χ. Solid lines correspond to the transition between the usual honeycomb and either the alternative honeycomb or the sixfold tiling, whereas dashed lines show the transitions between the alternative honeycomb and the sixfold tiling pattern. Blue lines correspond to the analytical calculations of appendix E, performed in the strong segregation limit ($\chi N \to \infty$). The transition between the alternative honeycomb and the sixfold tiling is independent of the segregation ratio since both structures exhibit the same branch line arrangement and we assumed that the core domain forms cylinders around these lines. The blue dashed line separates the stability regions of these phases, with the alternative honeycomb being stable for lower volume fractions of the molecular core. The solid line shows the transition between the usual honeycomb morphology and the respective other columnar phase. Green lines indicate the phase transitions obtained from the full numerical SCFT for the weakly segregated system at $\chi N = 25$. The solid line separates the usual and the alternative honeycomb whereas the dashed line is the phase boundary between the alternative honeycomb and the sixfold tiling. Not shown are the boundaries that these phases share with the disordered homogeneous state, cf. figure 6.2. Red lines show the numerical results for the moderately segregated system, $\chi N = 40$. The illustration of phase boundaries is equivalent to the previous case. At this segregation strength, however, we do not observe a disordered phase.

Chapter 7

Conclusion

We have demonstrated that it is possible to achieve new complex mesophases in systems of three-arm star-copolymers by introducing a core to these molecules. More precisely, we presented a specific tricontinuous structure which seems to be the most suitable candidate to supersede the honeycomb structure. The way to identify this novel mesophase began by an understanding of the self-assembly process based on polymer field theories which led to geometric criteria that afford a differentiation of different structures with respect to certain attributes. These concepts could be validated by more general numerical calculations which ultimately provide the equilibrium morphology for a particular molecular architecture and a given set of system parameters. However, we concede that there might be other structures yielding even lower free energies which have been overlooked so far. Nevertheless, these would still present novel mesophases which are very likely to be tricontinuous network structures with remarkable complexity. Moreover, the region of stability in the phase diagrams can only be broadened by new candidates, making an observation of novel mesophases even more likely.
Hence we are still left with a lot of experimental and theoretical challenges to identify stable complex morphologies. We summarize some ideas which might help to achieve this task.

On the theoretical side, we derived analytical expressions in the SST limit and used them to motivate certain structures and their triple line arrangements. These methods could be further utilized to achieve a robust analysis in the strong segregation limit. By exactly calculating the free energies of different structures according to the SST, a phase diagram could be constructed with this method. However, there are some constraints which have to be accounted for in this sort of analysis [42]. As was discussed, the volumes in each domain associated with a certain branch line segment, or an element of the core, have to be equal. This and the presence of curved interfaces between these domains will result in curved polymer paths making the calculation of the $z(\vec{r})$ values in e.g. (4.7) non-trivial.
Here, we used the full numerical SCFT method instead. The spectral approach allowed us to calculate the free energies of different candidate structures which in turn enabled us to construct phase diagrams, as demonstrated in chapter 6. Since some of the more interesting structures have in fact very low symmetries, it may be worthwhile to apply the real space approach to the SCFT. Furthermore, this alternative might help to explore new morphologies since a priori knowledge of the actual structure is not necessarily needed for this approach. Nevertheless, there are some challenges associated with this method, especially if one wants to apply it to complex three-dimensional morphologies. Algorithms have to be optimized in order to efficiently and accurately use this method due to its high computational costs

[12, 83, 78, 41, 76]. Additionally, one still has to be careful about boundary conditions since these can influence the outcome of the calculations.
In this context, other theoretical methods based on simulating molecular systems may be extremely helpful as well. These could extend the scope of application of our work from high molecular weight polymers to other (smaller) molecular constituents which might, in analogy to diblock copolymer and surfactant systems, show the formation of the same or at least similar morphologies. Moreover, simulations might be able test the question if the examined structures can form from a *dynamical* point of view. So far, we have only discussed equilibrium mesophases and mentioned the possibility of observing metastable configurations in experiments. A step towards assessing metastable morphologies and the kinetics of three-arm star-shaped molecules with functional or extended cores is therefore given by these methods. While they permit us to examine a broader range of systems they also suffer from choices of e.g. boundary conditions. The geometric concepts we developed and the structures we identified also provide an important starting point for these and other methods.

This being said, it becomes obvious that experiments with the suggested core-star-copolymers and related molecules are essential at this point. First and foremost, such experiments will test the presented ideas. Also, they may show new complex mesophases which can in turn be examined with the discussed methods. A strong collaboration between experimentalists and theoreticians is hence vital for the exploration and understanding of new complex materials. In terms of pure high molecular weight copolymer systems the core of these molecules could be realized by a fourth polymer species, which has in fact been the assumption for the numerical SCFT calculations in this thesis, see figure 4.4. By using dendronized polymers, depicted in figure 4.3(d), an additional bond between these cores could be achieved. Here, the fourth polymer species would not just occupy the center of the copolymers, but would rather form a polymer backbone onto which the other species can be attached.

On the low molecular weight front, star-polyphiles consisting of three immiscible arms have been examined [9]. These molecules exhibit aromatic cores or similarly rigid centers onto which the arms are attached. Due to their low molecular weight, the size of these centers is now comparable to the rest of the molecule. Additionally, different features can be assigned to the cores. Aromatic centers, for example, enable π-stacking and other architectures could result in H-bonding between adjacent cores. These approaches can thus result in bonds between adjacent molecules and could furthermore implement other concepts like a preferred torsion along the branch lines which would also favor self-assembly of more complex, tricontinuous morphologies [37]. The latter could, for example, be realized by chiral constituents and might very well induce a self-assembly of chiral mesophases, some of which have been presented in this thesis.
Although the SCFT is strictly only valid for high molecular weight polymers, we expect that the underlying ideas are qualitatively applicable to those star-polyphiles, too. We note that there are also various other approaches to realize polyphilic molecules with rigid centers, see for example [81]. Furthermore, molecular systems like discotic liquid crystals, which assembly into hexagonal columnar arrays, or other nanoparticles could form the basis for a molecular core onto which the three immiscible arms would be attached.

We note that no specific (balanced) tricontinuous structures have been unambiguously identified in star-copolymer systems so far, but an initial experimental study which suggested self-assembly of these complex soft matter mesophases, and thus motivated further research,

was performed on precisely these systems [63]. However, a particular tricontinuous structure has been reported in a different system, namely for a mesoporous material with a silica pore wall synthesized by a surfactant template [25], as discussed in section 3.4. The observation of another tricontinuous structure in a thermotropic liquid crystal has also been mentioned [86].

Lastly, we note that the tricontinuous structures we examined were balanced meaning that all domains, occupied by different polymer species, are congruent. While this seems like a reasonable assumption for symmetric copolymer architectures it must not necessarily hold true. Additionally, with different segregation strengths between distinct pairs of species or different volume fractions of the domains, it can be expected that other unbalanced morphologies will in fact represent the equilibrium solution. Since it is experimentally challenging to realize the criteria for symmetric star-copolymers, such unbalanced structures are presumably more likely to form in real systems. Although we examined the balanced case, the developed concepts can be just as well transfered to more general architectures.
While prismatic structures dominate a large portion of the phase diagram of simple three-arm star-copolymers [55], cf. figure 1.4, this thesis suggests that the introduction of the core can induce structural changes leading to different, possibly tricontinuous, morphologies. However, the vast amount of possible unbalanced structures makes it hard to identify equilibrium morphologies for every cases. This thesis therefore focused on balanced structures which already exhibit numerous possible candidate mesophases.
Furthermore, the addition of other types of constituents to these systems will stress different aspects of the self-assembled geometries possibly leading to yet other morphologies. The addition of homopolymers, for example, has been shown to relieve the effects of packing frustration since these molecules will occupy the regions which would otherwise only be reached by highly stretched chains [46]. This opposes the influence of the core which exacerbates the stretching effects.

It is a general pursue of science to understand even the most complex, and therefore most fascinating, phenomena that nature has to offer. Soft matter self-assembly, as it takes place in copolymer melts, doubtlessly belongs to the most interesting examples because it not only exhibits the formation of evermore complex geometries, but it also allows us to develop mathematical models and physical theories to comprehend the mechanisms involved. The curiosity to apply these concepts to more and more challenging problems incited people to consider self-assembled tricontinuous structures and search for prospects to synthesize them. On the other hand, scientists have not completely understood everything there is to know even in the simplest systems, yet. In this regard, there is also ongoing interest in the formation of tri- and polycontinuous structures in common surfactant systems [72].

In conclusion, we have presented a way to achieve novel, intricate morphologies in systems of triblock star-copolymers and related molecules. We hope that future experimental and theoretical studies will benefit from the concepts which have been developed in this thesis.

Bibliography

[1] Donald G. Anderson.
Iterative procedures for nonlinear integral equations.
J. ACM, 12(4):547–560, October 1965.

[2] Sten Andersson.
On the Description of Complex Inorganic Crystal Structures.
Angewandte Chemie International Edition in English, 22(2):69–81, 1983.

[3] R. C. Ball, J. F. Marko, S. T. Milner, and T. A. Witten.
Polymers grafted to a convex surface.
Macromolecules, 24(3):693–703, 1991.

[4] Frank S. Bates and Glenn H. Fredrickson.
Block copolymers—designer soft materials.
Physics Today, 52(2):32–38, 1999.

[5] V. A. Belyi.
Exclusion zone of convex brushes in the strong-stretching limit.
The Journal of Chemical Physics, 121(13):6547–6554, 2004.

[6] M. R. Bockstaller, R. A. Mickiewicz, and E. L. Thomas.
Block Copolymer Nanocomposites: Perspectives for Tailored Functional Materials.
Advanced Materials, 17(11):1331–1349, 2005.

[7] K. Brakke.
The surface evolver.
Experimental Mathematics, 1(2):141–165, 1992.

[8] Edward J. W. Crossland, Marleen Kamperman, Mihaela Nedelcu, Caterina Ducati, Ulrich Wiesner, Detlef M. Smilgies, Gilman E. S. Toombes, Marc A. Hillmyer, Sabine Ludwigs, Ullrich Steiner, and Henry J. Snaith.
A Bicontinuous Double Gyroid Hybrid Solar Cell.
Nano Letters, 9(8):2807–2812, 2009.
PMID: 19007289.

[9] Liliana de Campo, Trond Varslot, Minoo J. Moghaddam, Jacob J. K. Kirkensgaard, Kell Mortensen, and Stephen T. Hyde.
A novel lyotropic liquid crystal formed by triphilic star-polyphiles: hydrophilic/oleophilic/fluorophilic rods arranged in a 12.6.4. tiling.
Phys. Chem. Chem. Phys., 13:3139–3152, 2011.

[10] P.G. de Gennes.
Scaling Concepts in Polymer Physics.
Cornell University Press, 1979.

[11] M.P. do Carmo.
Differential Geometry of Curves and Surfaces.
Pearson Education Canada, 1976.

[12] F. Drolet and G. H. Fredrickson.
Combinatorial screening of complex block copolymer assembly with self-consistent field theory.
Phys. Rev. Lett., 83:4317–4320, Nov 1999.

[13] Ian W. Hamley Eds.
Developments in Block Copolymer Science and Technology.
John Wiley and Sons, Jan 2004.

[14] Veit Elser.
A cubic archimedean screw.
Philos. T. Math. Phys. Engin. Sci., 354(1715):pp. 2071–2075, 1996.

[15] Thomas H. Epps, Eric W. Cochran, Travis S. Bailey, Ryan S. Waletzko, Cordell M. Hardy, and Frank S. Bates.
Ordered network phases in linear poly(isoprene-b-styrene-b-ethylene oxide) triblock copolymers.
Macromolecules, 37(22):8325–8341, 2004.

[16] V. Eyert.
A comparative study on methods for convergence acceleration of iterative vector sequences.
Journal of Computational Physics, 124(2):271 – 285, 1996.

[17] Alexander S. Finnemore, Maik R. J. Scherer, Richard Langford, Sumeet Mahajan, Sabine Ludwigs, Fiona C. Meldrum, and Ullrich Steiner.
Nanostructured calcite single crystals with gyroid morphologies.
Advanced Materials, 21(38-39):3928–3932, 2009.

[18] Paul J. Flory.
Principles of Polymer Chemistry.
Baker lectures 1948. Cornell University Press, 1953.

[19] G. H. Fredrickson, V. Ganesan, and F. Drolet.
Field-theoretic computer simulation methods for polymers and complex fluids.
Macromolecules, 35(1):16–39, 2002.

[20] Glenn H. Fredrickson and Eugene Helfand.
Fluctuation effects in the theory of microphase separation in block copolymers.
The Journal of Chemical Physics, 87(1), 1987.

[21] J. L. Goveas, S. T. Milner, and W. B. Russel.
Corrections to strong-stretching theories.
Macromolecules, 30(18):5541–5552, 1997.

[22] Gregory M. Grason.
The packing of soft materials: Molecular asymmetry, geometric frustration and optimal lattices in block copolymer melts.
Physics Reports, 433(1):1 – 64, 2006.

[23] Theo Hahn, editor.
International Tables For Crystallography.
Kluwer Academic Publishers, Dordrecht, 1992.

[24] D.A. Hajduk, P.E. Harper, S.M. Gruner, C.C. Honeker, G. Kim, E.L. Thomas, and L.J. Fetters.
The gyroid: A new equilibrium morphology in weakly segregated diblock copolymers.
Macromolecules, 27(15):4063–4075, 1994.

[25] Y. Han, D. Zhang, L. L. Chng, J. Sun, L. Zhao, X. Zou, and J. Y. Ying.
A tri-continuous mesoporous material with a silica pore wall following a hexagonal minimal surface.
Nat Chem, 1(2):123–7, 2009.

[26] Eugene Helfand.
Theory of inhomogeneous polymers: Fundamentals of the gaussian random-walk model.
The Journal of Chemical Physics, 62(3):999–1005, 1975.

[27] Eugene Helfand and Anne Marie Sapse.
Theory of unsymmetric polymer–polymer interfaces.
The Journal of Chemical Physics, 62(4):1327–1331, 1975.

[28] Eugene Helfand and Yukiko Tagami.
Theory of the interface between immiscible polymers. ii.
The Journal of Chemical Physics, 56(7), 1972.

[29] Norman F.M. Henry and Kathleen Lonsdale Eds.
International Tables for X-Ray Crystallography.
Kynoch Press, 1969.

[30] K. M. Hong and J. Noolandi.
Theory of inhomogeneous multicomponent polymer systems.
Macromolecules, 14(3):727–736, 1981.

[31] S. T. Hyde, S. Andersson, K. Larsson, Z. Blum, T. Landh, S. Lidin, and B.W. Ninham.
The Language of Shape.
Elsevier Science, Amsterdam, 1997.

[32] S. T. Hyde and C. Oguey.
From 2D hyperbolic forests to 3D Euclidean entangled thickets.
Eur. Phys. J. B, 16:613–630, 2000.

[33] S. T. Hyde and S. Ramsden.
Polycontinuous morphologies and interwoven helical networks.
EPL, 50(2):135–141, 2000.

[34] S. T. Hyde, S. J. Ramsden, T. Di Matteo, and J. Longdell.
Ab-initio construction of some crystalline 3D Euclidean networks.
Solid State Sciences, 5:35–45, 2003.

[35] S. T. Hyde, M. O'Keeffe, and D. M. Proserpio.
Netze und gyroide: wenig bekannt und doch in chemie, materialwissenschaften und mathematik allgegenwärtig.
Angewandte Chemie, 120(42):8116–8121, 2008.

[36] S.T. Hyde and G.E. Schröder.
Novel surfactant mesostructural topologies: between lamellae and columnar (hexagonal) forms.
Current Opinion in Colloid & Interface Science, 8(1):5 – 14, 2003.

[37] Stephen T. Hyde, Liliana de Campo, and Christophe Oguey.
Tricontinuous mesophases of balanced three-arm 'star polyphiles'.
Soft Matter, 5:2782–2794, 2009.

[38] Ashish K. Khandpur, Stephan Foerster, Frank S. Bates, Ian W. Hamley, Anthony J. Ryan, Wim Bras, Kristoffer Almdal, and Kell Mortensen.
Polyisoprene-polystyrene diblock copolymer phase diagram near the order-disorder transition.
Macromolecules, 28(26):8796–8806, 1995.

[39] J. J. K. Kirkensgaard.
Kaleidoscopic tilings, networks and hierarchical structures in blends of 3-miktoarm star terpolymers.
Interface Focus, 2012.

[40] Ludwik Leibler.
Theory of microphase separation in block copolymers.
Macromolecules, 13(6):1602–1617, 1980.

[41] W. Li, Y. Xu, G. Zhang, F. Qiu, Y. Yang, and A. Shi.
Real-space self-consistent mean-field theory study of abc star triblock copolymers.
The Journal of Chemical Physics, 133(6):064904, 2010.

[42] A. E. Likhtman and A. N. Semenov.
Theory of microphase separation in block copolymer/homopolymer mixtures.
Macromolecules, 30(23):7273–7278, 1997.

[43] A. E. Likhtman and A. N. Semenov.
An advance in the theory of strongly segregated polymers.
EPL (Europhysics Letters), 51(3):307, 2000.

[44] Alexey E. Likhtman and Alexander N. Semenov.
Stability of the obdd structure for diblock copolymer melts in the strong segregation limit.
Macromolecules, 27(11):3103–3106, 1994.

[45] M. Maldovan, A. M. Urbas, N. Yufa, W. C. Carter, and E. L. Thomas.
Photonic properties of bicontinuous cubic microphases.
Phys. Rev. B, 65:165123, Apr 2002.

[46] M. W. Matsen.
Stabilizing new morphologies by blending homopolymer with block copolymer.
Phys. Rev. Lett., 74:4225–4228, May 1995.

[47] M. W. Matsen.
The standard gaussian model for block copolymer melts.
Journal of Physics: Condensed Matter, 14(2):R21, 2002.

[48] M. W. Matsen.
Self-Consistent Field Theory and Its Applications, pages 87–178.
Wiley-VCH Verlag GmbH & Co. KGaA, 2007.

[49] M. W. Matsen.
Fast and accurate scft calculations for periodic block-copolymer morphologies using the spectral method with anderson mixing.
Eur. Phys. J. E, 30(4):361–369, 2009.

[50] M. W. Matsen and F. S. Bates.
Origins of complex self-assembly in block copolymers.
Macromolecules, 29(23):7641–7644, 1996.

[51] M. W. Matsen and F. S. Bates.
Unifying weak- and strong-segregation block copolymer theories.
Macromolecules, 29(4):1091–1098, 1996.

[52] M. W. Matsen and F. S. Bates.
Conformationally asymmetric block copolymers.
Journal of Polymer Science Part B: Polymer Physics, 35(6):945–952, 1997.

[53] M. W. Matsen and M. Schick.
Stable and unstable phases of a diblock copolymer melt.
Phys. Rev. Lett., 72:2660–2663, Apr 1994.

[54] M.W. Matsen.
Investigating the dominant corrections to the strong-stretching theory for dry polymeric brushes.
Journal of Chemical Physics, 121(4):1938–1948, 2004.
cited By (since 1996)20.

[55] Y. Matsushita, K. Hayashida, T. Dotera, and A. Takano.
Kaleidoscopic morphologies from abc star-shaped terpolymers.
Journal of Physics: Condensed Matter, 23(28):284111, 2011.

[56] Wayne W. Maurer, Frank S. Bates, Timothy P. Lodge, Kristoffer Almdal, Kell Mortensen, and Glenn H. Fredrickson.
Can a single function for Ï‡ account for block copolymer and homopolymer blend phase behavior?
The Journal of Chemical Physics, 108(7), 1998.

[57] A. J. Meuler, M. A. Hillmyer, and F. S. Bates.
Ordered network mesostructures in block polymer materials.
Macromolecules, 42(19):7221–7250, 2009.

[58] S. T. Milner.
Polymer brushes.
Science, 251(4996):905–914, 1991.

[59] S. T. Milner, T. A. Witten, and M. E. Cates.
Theory of the grafted polymer brush.
Macromolecules, 21(8):2610–2619, 1988.

[60] Scott T. Milner.
Chain architecture and asymmetry in copolymer microphases.
Macromolecules, 27(8):2333–2335, 1994.

[61] Roland R. Netz and M. Schick.
Polymer brushes: from self-consistent field theory to classical theory.
Macromolecules, 31(15):5105–5122, 1998.

[62] Sang Soon Oh, Angela Demetriadou, Sebastian Wuestner, and Ortwin Hess.
On the Origin of Chirality in Nanoplasmonic Gyroid Metamaterials.
Advanced Materials, 25(4):612–617, 2013.

[63] Shigeru Okamoto, Hirokazu Hasegawa, Takeji Hashimoto, Teruo Fujimoto, Hongmin Zhang, Takeo Kazama, Atsushi Takano, and Yoshinobu Isono.
Morphology of model three-component three-arm star-shaped copolymers.
Polymer, 38(21):5275 – 5281, 1997.

[64] M. O'Keeffe, J. Plévert, Y. Teshima, Y. Watanabe, and T. Ogama.
The invariant cubic rod (cylinder) packings: symmetries and coordinates.
Acta Crystallographica Section A, 57(1):110–111, Jan 2001.

[65] Michael O'Keeffe, Maxim A. Peskov, Stuart J. Ramsden, and Omar M. Yaghi.
The reticular chemistry structure resource (rcsr) database of, and symbols for, crystal nets.
Accounts of Chemical Research, 41(12):1782–1789, 2008.

[66] William H. Press, Saul A. Teukolsky, William T. Vetterling, and Brian P. Flannery.
Numerical Recipes 3rd Edition: The Art of Scientific Computing.
Cambridge University Press, New York, NY, USA, 3 edition, 2007.

[67] M. Saba, M. Thiel, M. D. Turner, S. T. Hyde, M. Gu, K. Grosse-Brauckmann, D. N. Neshev, K. Mecke, and G. E. Schröder-Turk.
Circular dichroism in biological photonic crystals and cubic chiral nets.
Phys. Rev. Lett., 106:103902, 2011.

[68] Stefano Salvatore, Angela Demetriadou, Silvia Vignolini, Sang Soon Oh, Sebastian Wuestner, Nataliya A. Yufa, Morgan Stefik, Ulrich Wiesner, Jeremy J. Baumberg, Ortwin Hess, and Ullrich Steiner.
Tunable 3D Extended Self-Assembled Gold Metamaterials with Enhanced Light Transmission.
Advanced Materials, 25(19):2713–2716, 2013.

[69] Maik R. J. Scherer and Ullrich Steiner.
Efficient Electrochromic Devices Made from 3D Nanotubular Gyroid Networks.
Nano Letters, 13(7):3005–3010, 2013.

[70] Alan H. Schoen.
Infinite periodic minimal surfaces without self-intersections.
Technical Note TN D-5541, NASA, 1970.

[71] G.E. Schröder, S.J. Ramsden, A.G. Christy, and S.T. Hyde.
Medial surfaces of hyperbolic structures.
The European Physical Journal B - Condensed Matter and Complex Systems, 35(4):551–564, 2003.

[72] Gerd E. Schroder-Turk, Liliana de Campo, Myfanwy E. Evans, Matthias Saba, Sebastian C. Kapfer, Trond Varslot, Karsten Grosse-Brauckmann, Stuart Ramsden, and Stephen T. Hyde.
Polycontinuous geometries for inverse lipid phases with more than two aqueous network domains.
Faraday Discuss., 161:215–247, 2013.

[73] John M. Seddon.
Structure of the inverted hexagonal (hii) phase, and non-lamellar phase transitions of lipids.
Biochimica et Biophysica Acta (BBA) - Reviews on Biomembranes, 1031(1):1 – 69, 1990.

[74] A. N. Semenov.
Contribution to the theory of microphase layering in block-copolymer melts.
Zhurnal Eksperimentalnoi I Teoreticheskoi Fiziki, 88(4):1242–1256, 1985.

[75] A. N. Semenov.
Theory of block copolymer interfaces in the strong segregation limit.
Macromolecules, 26(24):6617–6621, 1993.

[76] Mingzhu Sun, Peng Wang, Feng Qiu, Ping Tang, Hongdong Zhang, and Yuliang Yang.
Morphology and phase diagram of *abc* linear triblock copolymers: Parallel real-space self-consistent-field-theory simulation.
Phys. Rev. E, 77:016701, Jan 2008.

[77] Mikihito Takenaka, Tsutomu Wakada, Satoshi Akasaka, Shotaro Nishitsuji, Kenji Saijo, Hirofumi Shimizu, Myung Im Kim, and Hirokazu Hasegawa.
Orthorhombic f*ddd* network in diblock copolymer melts.
Macromolecules, 40(13):4399–4402, 2007.

[78] Ping Tang, Feng Qiu, Hongdong Zhang, and Yuliang Yang.
Morphology and phase diagram of complex block copolymers: Abc star triblock copolymers.
The Journal of Physical Chemistry B, 108(24):8434–8438, 2004.

[79] R. B. Thompson, K. O/. Rasmussen, and T. Lookman.
Improved convergence in block copolymer self-consistent field theory by anderson mixing.
The Journal of Chemical Physics, 120(1), 2004.

[80] S. Torquato, S. Hyun, and A. Donev.
Multifunctional composites: Optimizing microstructures for simultaneous transport of heat and electricity.
Phys. Rev. Lett., 89:266601, Dec 2002.

[81] C. Tschierske, C. Nürnberger, H. Ebert, B. Glettner, M. Prehm, F. Liu, X.-B. Zeng, and G. Ungar.

Complex tiling patterns in liquid crystals.
Interface Focus, 2011.

[82] Christopher A. Tyler and David C. Morse.
Orthorhombic f*ddd* network in triblock and diblock copolymer melts.
Phys. Rev. Lett., 94:208302, May 2005.

[83] G. Tzeremes, K. Ø. Rasmussen, T. Lookman, and A. Saxena.
Efficient computation of the structural phase behavior of block copolymers.
Phys. Rev. E, 65:041806, Apr 2002.

[84] Silvia Vignolini, Nataliya A. Yufa, Pedro S. Cunha, Stefan Guldin, Ilia Rushkin, Morgan Stefik, Kahyun Hur, Ulrich Wiesner, Jeremy J. Baumberg, and Ullrich Steiner.
A 3D Optical Metamaterial Made by Self-Assembly.
Advanced Materials, 24(10):OP23–OP27, 2012.

[85] Zhen-Gang Wang.
Chain dimensions in amorphous polymer melts.
Macromolecules, 28(2):570–576, 1995.

[86] Xiangbing Zeng, Goran Ungar, and Marianne Imperor-Clerc.
A triple-network tricontinuous cubic liquid crystal.
Nat Mater, 4:562–567, 2005.

Appendix A

The calculus of functionals

We briefly summarize some of the techniques from the calculus of functionals which have been used for the derivation of the SCFT. A functional, $\mathcal{F}$, is simply a function which takes a function, say f, as its argument and returns a scalar number, $\mathcal{F}[f]$. The functional derivative of $\mathcal{F}$ at $f(y)$ is defined as

$$\frac{D\mathcal{F}}{Df(y)} \equiv \lim_{\epsilon \to 0} \frac{\mathcal{F}[f + \epsilon\delta] - \mathcal{F}[f]}{\epsilon} \tag{A.1}$$

where $\mathcal{F}[f + \epsilon\delta]$ represents the functional evaluated for the input function $f(x) + \epsilon\delta(x - y)$ and $\delta(x)$ is the usual Dirac delta function. The functional integral of $\mathcal{F}$ is formally defined by employing ordinary multi-dimensional integrals for all values f(x) of the functionals input function,

$$\int Df \ \mathcal{F}[f] \equiv \int ... \int \prod_x df(x) \mathcal{F}[f]. \tag{A.2}$$

We can also introduce a Dirac delta functional which takes functions as arguments, $\delta[f]$. This functional is defined such that it fulfills the functional analog of the shifting property of the usual Dirac delta function,

$$\int Df \ \delta[f - g] \mathcal{F}[f] = \mathcal{F}[g], \tag{A.3}$$

where $\mathcal{F}$ is a functional and f and g are ordinary functions. If we set $\mathcal{F}[f] \equiv 1$ we obtain

$$\int Df \ \delta[f - g] = 1. \tag{A.4}$$

Using the integral representation of the ordinary Dirac delta function,

$$\delta(x) = \frac{1}{2\pi} \int_{-\infty}^{\infty} dk \ \exp(ikx), \tag{A.5}$$

we can derive an analogous integral representation for the Dirac delta functional $\delta[f]$ by approximating it by a product of ordinary delta functions for all values $f(x)$ of its input function. This leads to

$$\delta[f] \propto \int Dk \ \exp\left(i \int dx \ k(x) f(x)\right), \tag{A.6}$$

where $\int Dk$ is a functional integral over the function $k(x)$. We can avoid problems associated with fixing the proportionality constant in (A.6) because our application of this formula in the context of SCFT renders this constant unimportant. If we redefine $k(x) \to \frac{\rho_0}{iN} k(x)$ in (A.6), we end up with

$$\delta[f] \propto \int Dk \ \exp\left(\frac{\rho_0}{N} \int dx \ k(x) f(x)\right), \tag{A.7}$$

where the integration with respect to x is performed in the complex plane along the imaginary axis. This expression for the delta functional was used in the context of SCFT.

Appendix B

Fourier representation of periodic functions

Any periodic function $f(\vec{r})$ in three-dimensional space $\mathbb{R}^3$ can be represented via its Fourier series,

$$f(\vec{r}) = \sum_{\vec{G}} f_{\vec{G},C} \cos(\vec{G} \cdot \vec{r}) + f_{\vec{G},S} \sin(\vec{G} \cdot \vec{r}). \tag{B.1}$$

$\vec{G}$ are the vectors of the reciprocal lattice, which can be deduced from the primitive vectors of the direct lattice, and $f_{\vec{G},C}$ and $f_{\vec{G},S}$ are the respective Fourier coefficients. In our notation, the vectors $-\vec{G}$ and $\vec{G}$ describe the same mode and only one of them needs to be considered. For example, we might choose only those which satisfy $(G_z > 0)$, $(G_y > 0 \wedge G_z = 0)$ or $(G_x \geq 0 \wedge G_y = 0 \wedge G_z = 0)$.
Let us now consider a symmetry transformation which leaves the function $f(\vec{r})$ unchanged,

$$\vec{r} \to \mathbf{A}\vec{r} + \vec{a}. \tag{B.2}$$

A is an invertible matrix and $\vec{a}$ is a vector. Due to the invariance of $f(\vec{r})$ under this transformation we have

$$\begin{aligned}
f(A\vec{r} + \vec{a}) &= \sum_{\vec{G}} f_{\vec{G},C} \cos(\vec{G} \cdot (\mathbf{A}\vec{r} + \vec{a})) + f_{\vec{G},S} \sin(\vec{G} \cdot (\mathbf{A}\vec{r} + \vec{a})) \\
&= \sum_{\vec{G}} f_{\vec{G},C} \cos(\mathbf{A^T}\vec{G} \cdot \vec{r} + \vec{G} \cdot \vec{a}) + f_{\vec{G},S} \sin(\mathbf{A^T}\vec{G} \cdot \vec{r} + \vec{G} \cdot \vec{a}) \\
&= \sum_{\vec{G}} f_{\vec{G},C} \left[\cos(\mathbf{A^T}\vec{G} \cdot \vec{r}) \cos(\vec{G} \cdot \vec{a}) - \sin(\mathbf{A^T}\vec{G} \cdot \vec{r}) \sin(\vec{G} \cdot \vec{a})\right] \\
&\quad + f_{\vec{G},S} \left[\cos(\mathbf{A^T}\vec{G} \cdot \vec{r}) \sin(\vec{G} \cdot \vec{a}) + \sin(\mathbf{A^T}\vec{G} \cdot \vec{r}) \cos(\vec{G} \cdot \vec{a})\right] \\
&= \sum_{\vec{G}} \cos(\mathbf{A^T}\vec{G} \cdot \vec{r}) \left[f_{\vec{G},C} \cos(\vec{G} \cdot \vec{a}) + f_{\vec{G},S} \sin(\vec{G} \cdot \vec{a})\right] \\
&\quad + \sin(\mathbf{A^T}\vec{G} \cdot \vec{r}) \left[-f_{\vec{G},C} \sin(\vec{G} \cdot \vec{a}) + f_{\vec{G},S} \cos(\vec{G} \cdot \vec{a})\right] \\
&\stackrel{!}{=} f(\vec{r}) = \sum_{\mathbf{A^T}\vec{G}} f_{\mathbf{A^T}\vec{G},C} \cos(\mathbf{A^T}\vec{G} \cdot \vec{r}) + f_{\mathbf{A^T}\vec{G},S} \sin(\mathbf{A^T}\vec{G} \cdot \vec{r}),
\end{aligned} \tag{B.3}$$

which establishes a correspondence between certain Fourier coefficients,

$$\begin{pmatrix} f_{\mathbf{A}^T\vec{G},S} \\ f_{\mathbf{A}^T\vec{G},C} \end{pmatrix} = \begin{bmatrix} \cos(\vec{G}\cdot\vec{a}) & -\sin(\vec{G}\cdot\vec{a}) \\ \sin(\vec{G}\cdot\vec{a}) & \cos(\vec{G}\cdot\vec{a}) \end{bmatrix} \begin{pmatrix} f_{\vec{G},S} \\ f_{\vec{G},C} \end{pmatrix} \tag{B.4}$$

This corresponds to a rotation through the angle $\vec{G}\cdot\vec{a}$ in the two-dimensional space defined by the coefficients $f_{\vec{G},S}$ and $f_{\vec{G},C}$. It should again be noted that the Fourier coefficients of the vectors $-\vec{G}$ and $\vec{G}$ are in a fixed relationship to each other, namely

$$\begin{aligned} f_{\vec{G},S} &= -f_{-\vec{G},S} \\ f_{\vec{G},C} &= f_{-\vec{G},C} \end{aligned} \tag{B.5}$$

Equation (B.3) shows that any existing symmetry transformations allow us to identify certain Fourier coefficients. Thereby, we end up with a reduced number of basis functions required to describe a certain geometry with this symmetry because we only need to specify the coefficients of independent Fourier components.

Appendix C

Expressions for the components of the Lagrange multiplier

We demonstrate the expressions for the components of the Lagrange multiplier, κ_i, which need to be evaluated in each iteration of the spectral method in order to solve the self-consistent field equations, cf. section 2.3. The derivation of these formulas is based on combining the incompressibility constraint (2.96) with the self-consistent condition (2.97) which results in a system of linear equations where the $\chi_{JK}N$ enter the coefficients, the $\omega_{I,i}$ provide the constant terms, and the variables are given by the $\phi_{I,i}$ and the κ_i, which we want to obtain.
The resulting forms of the κ_i components differ for the individual copolymer architectures. For diblock copolymers (with polymer species A and B) we have

$$\kappa_i = \frac{1}{2}\left(\omega_{A,i} + \omega_{B,i}\right), \tag{C.1}$$

where $i \geq 1$.
For simple triblock copolymers (species A, B and C) we have (for $i \geq 1$)

$$\kappa_i = \frac{1}{\sum_{I\in\{A,B,C\}} X_I} \sum_{I\in\{A,B,C\}} X_I \omega_{I,i}, \tag{C.2}$$

where

$$X_I = \sum_{J\neq K\neq I} \chi_{JK}N\left(\chi_{IJ}N + \chi_{IK}N - \chi_{JK}N\right). \tag{C.3}$$

Finally, we consider triblock star-copolymers with an extended core. The outer arms of the copolymer consist of species A, B and C, as before, and the species forming the core is denoted X. Upon assuming equal interactions between the outer species, $\chi \equiv \chi_{AB}N = \chi_{AC}N = \chi_{BC}N$ and equal interactions between the core and all other species, $\chi_X \equiv \chi_{AX}N = \chi N_{BX} = \chi N_{CX}$, we have (for $i \geq 1$)

$$\kappa_i = \frac{\chi_X N}{6\chi_X N - 2\chi N}\left(\sum_{I\in\{A,B,C\}} \omega_{I,i} + \frac{3\chi_X N - 2\chi N}{\chi_X N}\omega_{X,i}\right). \tag{C.4}$$

These three examples cover all relevant copolymer architectures for this thesis.

Appendix D

Scaling behavior of free energies in the strong segregation theory

We wish to minimize the SST free energy with respect to the size of the unit cell, ξ. This can be done by factoring out the scaling behavior of the interfacial and the stretching term,

$$\begin{aligned}
\frac{F}{nk_BT} =& \frac{1}{\xi}\frac{F_{Int;\xi=1}}{nk_BT} + \xi^2\frac{F_{Conf;\xi=1}}{nk_BT},\\
\frac{\partial}{\partial\xi}\frac{F}{nk_BT} =& -\frac{1}{\xi^2}\frac{F_{Int;\xi=1}}{nk_BT} + 2\xi\frac{F_{Conf;\xi=1}}{nk_BT} \stackrel{!}{=} 0,\\
\xi =& \sqrt[3]{\frac{F_{Int;\xi=1}}{2F_{Conf;\xi=1}}},\\
\frac{F}{nk_BT} =& 2^{\frac{1}{3}}\left(\frac{F_{Int;\xi=1}}{nk_BT}\right)^{\frac{2}{3}}\left(\frac{F_{Conf;\xi=1}}{nk_BT}\right)^{\frac{1}{3}} + 2^{-\frac{2}{3}}\left(\frac{F_{Int;\xi=1}}{nk_BT}\right)^{\frac{2}{3}}\left(\frac{F_{Conf;\xi=1}}{nk_BT}\right)^{\frac{1}{3}}\\
=& \frac{3}{2^{\frac{2}{3}}}\left(\frac{F_{Int;\xi=1}}{nk_BT}\right)^{\frac{2}{3}}\left(\frac{F_{Conf;\xi=1}}{nk_BT}\right)^{\frac{1}{3}} = \frac{3}{2^{\frac{2}{3}}}\left(\frac{F_{Int}}{nk_BT}\right)^{\frac{2}{3}}\left(\frac{F_{Conf}}{nk_BT}\right)^{\frac{1}{3}},
\end{aligned} \tag{D.1}$$

where $\frac{F_{Int}}{nk_BT}$ is the interfacial contribution to the free energy, cf. (2.66), and $\frac{F_{Conf}}{nk_BT}$ is the contribution due to the stretching of polymer chains (2.78). Both contributions depend on the choice of the size of the unit cell, ξ. $\frac{F_{Int;\xi=1}}{nk_BT}$ and $\frac{F_{Conf;\xi=1}}{nk_BT}$ describe the respective contributions when evaluated for $\xi = 1$. In the last step, we were able to evaluate the minimized free energy for arbitrary ξ. Therefore, the final expression does not depend on the choice of ξ, as must be the case, and we can choose a unit cell of arbitrary size to evaluate it. From the steps in (D.1) it can also be seen that the ratio between the total interfacial contribution and the total stretching contribution at the preferred length scale is always equal to $2^{\frac{1}{3}}/2^{-\frac{2}{3}} = 2$.
For simple diblock copolymers, the free energy contributions read (cf. section 3.2)

$$\begin{aligned}
\frac{F_{Int}}{nk_BT} \equiv& Na\sqrt{\frac{\chi}{6}}\frac{A_{AB}}{V},\\
\frac{F_{Conf}}{nk_BT} \equiv& \frac{3\pi^2}{8Na^2V}\left[\frac{1}{f^2}\int_{V_A} d^3r\ z^2 + \frac{1}{(1-f)^2}\int_{V_B} d^3r\ z^2\right].
\end{aligned} \tag{D.2}$$

For (simple) balanced triblock copolymers we can write (cf. section 4.1)

$$\begin{aligned}\frac{F_{Int}}{nk_BT} \equiv & Na\sqrt{\frac{\chi}{6}}\frac{A_{ABC}}{V}, \\ \frac{F_{Conf}}{nk_BT} \equiv & \frac{3\pi^2}{8f^2Na^2V}\int_{V_{ABC}} d^3r\ z^2(\vec{r}).\end{aligned} \tag{D.3}$$

The more sophisticated triblock copolymers architectures with an extended polymeric core yield (cf. section 4.2)

$$\begin{aligned}\frac{F_{Int}}{nk_BT} \equiv & \frac{Na}{\sqrt{6}}\left[\frac{\sqrt{\chi}A_{ABC}+\sqrt{\chi_X}A_X}{V}\right], \\ \frac{F_{Conf}}{nk_BT} \equiv & \frac{3\pi^2}{8Na^2V}\left[\frac{1}{f^2}\int_{V_{ABC}} d^3r\ z^2(\vec{r}) + \frac{1}{f_X^2}\int_{V_X} d^3r\ z^2(\vec{r})\right].\end{aligned} \tag{D.4}$$

Appendix E

Explicit free energy calculations for the columnar phases

An accurate treatment in the context of the SST is possible for all of the columnar phases that have been presented because the coarse-grained polymer paths have to follow straight lines that are attached to the next branch line, or equivalently to the next interface of the core, by virtue of the structure's geometry. This facilitates the evaluation of the polymeric path distances z, providing a concrete calculation of the free energy for melts of triblock star-copolymers with an extended core when we make the assumptions that the core species forms cylindrical compartments that are centered around the branch lines. This might generally not be the case, but should become increasingly accurate for a strong segregation strength of the core species X, when compared to the segregation strengths among the other components, i.e. in the limit $\frac{\chi_{XX}}{\chi} \to \infty$. In order to calculate the free energy, given by (4.7), we have to evaluate the geometric properties that are involved in this equation. These are the surface areas of the interfaces between the species A, B and C, denoted A_{ABC}, and the surface areas of the interfaces between the core species X and any other species, A_X. Furthermore, we need the volume V of the system and we must perform the integrals $\int_{V_{ABC}} d^3r\, z^2(\vec{r})$ and $\int_{V_X} d^3r\, z^2(\vec{r})$ which quantify the entropic costs of stretching polymer chains within the melt state. It is sufficient to calculate the expression for a representative part of the structure, e.g. for a single unit cell. We go even further and just consider a particular branch line segment of the structure and its associated Voronoi cell. The whole structure is then simply constructed by adding several of these representative Voronoi cells.

Let us begin by considering the usual honeycomb structure. Figure 4.2(a) shows its geometry and a representative Voronoi cell is framed by purple lines. This Voronoi cell is given by a prism with triangular cross-section. The branch line is centered within this Voronoi region and its length is given by the height of the prism. Therefore, we identify the height of the Voronoi cell to be L. The triangular cross-section can be described by the length of the triangle's sides, labeled a. Thus, the volume of the Voronoi cell, V, is given by

$$V = \frac{\sqrt{3}}{4} a^2 L. \tag{E.1}$$

Let us describe the region occupied by the core species as a cylinder that is centered around the branch line. The height of the cylinder must be L and its radius will be denoted R. Hence the volume occupied by the core species, V_X, is given by $V_X = \pi R^2 L$. With that, we

can calculate the volume fraction of the core,

$$\phi \equiv \frac{V_X}{V} = \frac{4\pi}{\sqrt{3}} \left(\frac{R}{a}\right)^2. \tag{E.2}$$

This in return allows us to express R/a by the volume fraction ϕ,

$$\frac{R}{a} = \sqrt{\frac{\sqrt{3}\phi}{4\pi}}. \tag{E.3}$$

The interfacial areas are given by

$$A_{ABC} = 3L \left[\frac{a}{2\sqrt{3}} - R\right] \tag{E.4}$$

and

$$A_X = 2\pi RL, \tag{E.5}$$

respectively. In order to perform the integrals, we evaluate the surface area of the cylindrical segments that are defined as the part of a cylinder of radius y centered around the branch line that is fully contained within the Voronoi cell. We denote these areas by $A(y)$. The (uniform) distance between these cylindrical segments and the interface of the core, i.e. the polymeric path distance, is then given by $z = |y - R|$. We find

$$A(y) = \begin{cases} L2\pi y, & \text{if } y \leq \frac{a}{2\sqrt{3}} \\ Ly\left[2\pi - 6\arccos\left(\frac{a}{2\sqrt{3}y}\right)\right], & \text{if } \frac{a}{2\sqrt{3}} \leq y \leq \frac{a}{\sqrt{3}} \end{cases}. \tag{E.6}$$

The integral for the outer brushes of species A, B and C can then be solved,

$$\begin{aligned} \int_{V_{ABC}} d^3r\ z^2(\vec{r}) =& \int_R^{\frac{a}{\sqrt{3}}} dy\ A(y)(y-R)^2 \\ =& La^4 \left\{ \frac{1}{16\sqrt{3}} - \left[\frac{1}{6} + \frac{\ln(2+\sqrt{3})}{12\sqrt{3}}\right] \frac{R}{a} + \frac{\sqrt{3}}{4}\left(\frac{R}{a}\right)^2 - \frac{\pi}{6}\left(\frac{R}{a}\right)^4 \right\}. \end{aligned} \tag{E.7}$$

Similarly, the integral for the stretching contribution of the core domains can be resolved,

$$\int_{V_X} d^3r\ z^2(\vec{r}) = \int_0^R dy\ A(y)(R-y)^2 = \frac{\pi}{6} R^4 L. \tag{E.8}$$

Putting the previous equations together allows us to express the free energy (4.7) via the volume fraction of the core ϕ, the ratio of segregation strengths $\frac{\chi_X}{\chi}$, and the ratio $\frac{f}{f_X}$ which encodes the precise molecular architecture.
For a star-copolymer with an extended core and equal statistical segment lengths for all species but possible multiple chains of each outer species (A, B ,C) attached to the core, we have

$$\frac{f}{f_X} = \frac{1-\phi}{m\phi}, \tag{E.9}$$

where m is the number of chains of each species A, B, C that are attached to the molecular core, e.g. $m = 2$ for the dual-chain triblock star-copolymers in figure 4.4(b).

Let us now consider the alternative honeycomb morphology. Its representative Voronoi cell is shown in figure 4.2(b). The height of this cell is again given by the length of branch lines in it, denoted L as before. The cross-section of the Voronoi regions is a hexagon. From now on we use a to label the length of each side of this hexagon. Thus the volume V of the Voronoi cell can be written as

$$V = \frac{3\sqrt{3}}{2} a^2 L. \tag{E.10}$$

Since the volume of the core region can again be described by $V_X = \pi R^2 L$, where R is the radius of the cylindrical core domain, we express its volume fraction ϕ by

$$\phi \equiv \frac{V_X}{V} = \frac{2\pi}{3\sqrt{3}} \left(\frac{R}{a}\right)^2. \tag{E.11}$$

R/a is thus given by the volume fraction ϕ,

$$\frac{R}{a} = \sqrt{\frac{3\sqrt{3}\phi}{2\pi}}. \tag{E.12}$$

The area of the interfaces between species A, B and C (within the Voronoi cell) is

$$A_{ABC} = 3L\left[a - R\right], \tag{E.13}$$

whereas the area of the interface of the core is given by

$$A_X = 2\pi RL, \tag{E.14}$$

as before. We have to calculate the area of cylindrical segments at distance y that are centered around the branch line and fully contained within the Voronoi cell. We find

$$A(y) = \begin{cases} L2\pi y, & \text{if } y \leq \frac{\sqrt{3}a}{2} \\ Ly\left[2\pi - 12\arccos\left(\frac{\sqrt{3}a}{2y}\right)\right], & \text{if } \frac{\sqrt{3}a}{2} \leq y \leq a \end{cases}. \tag{E.15}$$

We use this expression to evaluate the integral for the outer brushes of species A, B and C,

$$\begin{aligned} \int_{V_{ABC}} d^3r\ z^2(\vec{r}) =& \int_R^a dy\ A(y)(y-R)^2 \\ =& La^4 \left\{ \frac{5\sqrt{3}}{8} - \frac{\sqrt{3}}{4}\left[4 + 3\ln(3)\right]\frac{R}{a} + \frac{3\sqrt{3}}{2}\left(\frac{R}{a}\right)^2 - \frac{\pi}{6}\left(\frac{R}{a}\right)^4 \right\}. \end{aligned} \tag{E.16}$$

The integral for the stretching contribution of the core domains takes the same form as before,

$$\int_{V_X} d^3r\ z^2(\vec{r}) = \int_0^R dy\ A(y)(R-y)^2 = \frac{\pi}{6} R^4 L. \tag{E.17}$$

Inserting the previous expression in (4.7) allows us to obtain the free energy for the alternative honeycomb structure. By comparing it with the free energy of the honeycomb we can identify the location of the phase transition between the two mesophases.

Lastly, let us consider the sixfold tiling. Since its branch line arrangement is identical to that of the alternative honeycomb structure, we can choose the same Voronoi cell as before.

This renders most calculations identical to those presented for the alternative honeycomb. The only difference is the area of interfaces between species A, B and C. Instead of (E.13) we now have

$$A_{ABC} = 4L \left[\frac{\sqrt{3}a}{2} - R \right], \tag{E.18}$$

where we have taken into account that the Voronoi cells of every third branch line contains twice the amount of interfaces compared to the other Voronoi cells. The only difference in the free energies of the alternative honeycomb and the sixfold tiling is thus given by their different expression for these surface areas. By comparing (E.13) with (E.18) and using (E.12) to express $\frac{R}{a}$ via the volume fraction ϕ, we can calculate the volume fraction for the transition between the two phases, which turns out to be $\phi_{Trans} = \frac{2\pi}{3\sqrt{3}}(2\sqrt{3}-3)^2 \approx 0.26$. Therefore, in the context of the SST, this transition only depends on the volume fraction of the core, with the alternative honeycomb being stable for smaller volume fractions.
Likewise, we can use the analytical expressions that have been derived in this section to calculate the phase transitions between all columnar phases. Figure 6.3 compares these phase boundaries with those obtained from the full numerical SCFT calculations.

Furthermore, we employ this analytical treatment to obtain values for the two geometric measures comprised in equation (4.4). These geometric properties measure the interface configuration, $\frac{A_{ABC}}{\sqrt{LV}}$, and the packing frustration, $\frac{L}{V}\left\langle z^2 \right\rangle_{ABC}$, respectively. They have been used in chapter 5 to estimate the relevance of different candidate morphologies for the self-assembly of triblock star copolymers. For their evaluation, we assumed that the polymer brushes are grafted to the one-dimensional branch lines, i.e. $R = 0$, and that the polymer paths are straight and perpendicular to them, as has been the assumption in this section. Therefore it is sufficient to use the previous expressions while setting $R = 0$.
For the usual honeycomb we obtain

$$\frac{A_{ABC}}{\sqrt{LV}} \overset{R=0}{=} 3^{1/4} \approx 1.32 \tag{E.19}$$

and

$$\frac{L}{V}\left\langle z^2 \right\rangle_{ABC} \equiv \frac{L}{V^2}\int_{V_{ABC}} d^3r\, z^2(\vec{r}) \overset{R=0}{=} \frac{1}{3\sqrt{3}} \approx 0.192. \tag{E.20}$$

For the alternative honeycomb we have

$$\frac{A_{ABC}}{\sqrt{LV}} \overset{R=0}{=} \sqrt{2}\,3^{1/4} \approx 1.86 \tag{E.21}$$

and

$$\frac{L}{V}\left\langle z^2 \right\rangle_{ABC} \equiv \frac{L}{V^2}\int_{V_{ABC}} d^3r\, z^2(\vec{r}) \overset{R=0}{=} \frac{5}{18\sqrt{3}} \approx 0.160. \tag{E.22}$$

The sixfold tiling has the same packing frustration as the alternative honeycomb (E.22) due to the same arrangement of branch lines in these structures. However, in the limit $R = 0$ the interfacial energy of the sixfold tiling is higher,

$$\frac{A_{ABC}}{\sqrt{LV}} \overset{R=0}{=} \frac{2\sqrt{2}}{3^{1/4}} \approx 2.15. \tag{E.23}$$

Acknowledgment

I am very grateful for the help and support from my supervisor PD Dr. Gerd Schröder-Turk. Not only did he provide me with advice at all times during my research, but he consistently pushed me to improve. Furthermore, he managed to get me excited for many projects and ideas, and he in turn was always open to new ideas from my side. This led to a very productive and exciting working environment with countless hours of discussions. Additionally, he made it possible for me to stay with our collaborating group at the Australian National University (ANU) in Canberra, Australia for a couple of month during my research. He also offered me to present my results at multiple (international) conferences, which allowed me to get valuable insights into the work (and life) of a scientist. Finally, he did always care for my situation and helped me to make the decisions which were best for me. I couldn't have hoped for a better supervisor.

I want to thank Prof. Klaus Mecke for the possibility to write this thesis at the Chair of Theoretical Physics I. More importantly, I want to thank him for his advice and support throughout my studies at the university of Erlangen-Nürnberg. This ranges from the lectures he was giving, which I particularly enjoyed, to his role in the "Forschungsstudiengang Physik". This program of studies offered a unique experience with lots of special offers for the students and individual opportunities. Therefore, I am very glad that I had the opportunity to study in this program.

I would like to thank Dr. Liliana de Campo for all her help, especially during my stay at the ANU. There have been countless occasions where she provided me with explanations, relevant data or discussions. Her help went far beyond the purely professional side of my stay and I had an amazing time in Australia due to her aid.

I thank Prof. Stephen Hyde at the ANU for his help with my research. He was always inspiring and I am glad that I had the chance to work with him. I took great benefit from his lectures and discussions with him.

I thank Dr. Myfanwy Ewans for her help on various occasions and for her informative discussions.

Furthermore, I would like to thank all people at the Chair of Theoretical Physics I for their help. They provided an enjoyable atmosphere and I had a lot of fun in this group.

I'd like to thank Dr. Jacob Kirkensgaard at the Niels Bohr Institute in Copenhagen for the discussions we had and his input regarding the extension of this project by other simulation methods.

I am grateful for financial support by the DAAD PROMOS program, the "Elitenetzwerk Bayern" and the "Leonardo-Kolleg" of the University of Erlangen that facilitated my stay at the ANU and at other conferences and meetings.

Thank goes to the "Rechenzentrum Erlangen" (RRZE) for providing me with an account to perform my calculations on their computing clusters. Furthermore, I thank Dr. Hager who

supported me with useful information to adopt my code such that it was working efficiently on these clusters.

I thank Prof. Matsen at the University of Reading for his suggestions regarding my research and for introducing me to recent improvements to the spectral method for solving the self-consistent field equations.

I'd like to thank Prof. Kell Mortensen at the Niels Bohr Institute in Copenhagen for our discussions.

Without knowing him personally, I thank Prof. Kenneth Brakke for his free software *Surface Evolver* which was used to construct several models of minimal surfaces that served as a valuable starting point for my calculations and illustrations.

Last but not least, I thank my parents and my girlfriend for all their support and encouragement. It would be impossible to list their help in detail and thus I just want to state that its due to them that I was able to pursue my studies and my passions.

Statement of originality

I hereby confirm that I have written the presented thesis by myself, without contributions from any sources other than those cited in the text and acknowledgements. This also applies to all figures included in the thesis.

Erlangen, February 27, 2014

Michael Fischer

Erklärung

Hiermit erkläre ich, dass ich die vorgelegte Masterarbeit selbstständig und lediglich unter Benutzung der angegebenen Quellen und Hilfsmittel, sowie durch die entsprechende Unterstützung der in der Danksagung genannten Personen, verfasst habe. Zitate sind an den entsprechenden Stellen kenntlich gemacht. Dies bezieht sich auch auf alle in dieser Arbeit dargestellten Abbildungen.

Erlangen, 27. Februar 2014

Michael Fischer